

UNIVERSITY OF OKLAHOMA

GRADUATE COLLEGE

DEVELOPMENT OF PHAGE DISPLAY-DERIVED TARGETED CANCER THERAPY AND
NET-WORK SCAFFOLD FOR 3D CANCER CELL CULTURE

A DISSERTATION

SUBMITTED TO THE GRADUATE FACULTY

in partial fulfillment of the requirements for the

Degree of

DOCTOR OF PHILOSOPHY

By

XUEWEI QU
Norman, Oklahoma
2018

DEVELOPMENT OF PHAGE DISPLAY-DERIVED TARGETED CANCER THERAPY AND
NET-WORK SCAFFOLD FOR 3D CANCER CELL CULTURE

A DISSERTATION APPROVED FOR THE
DEPARTMENT OF CHEMISTRY AND BIOCHEMISTRY

BY

Dr. Chuanbin Mao, Chair

Dr. Elena I. Zgurskaya

Dr. Wai Tak Yip

Dr. Yihan Shao

Dr. Scott D. Russell

Acknowledgements

Pursuing PhD degree in a foreign country is the biggest challenge of my life. It is fulfilled with difficulties and accomplishment, tears and joys, confusion and encouragement, failure and lesson. I am lucky enough to have people being around me, supporting me and helping me for all these years.

First, I thank my major professor, respected Dr. Chuanbin Mao for all the supports and directions he gave to me to overcome the difficulties of my study. So that I can possibly do the interesting research and complete this dissertation. His enthusiasm in work I have seen will definitely influence me in the future.

I also would give my most sincere thanks to all my dissertation and advisory committee members, Dr. Scott D. Russell, Dr. Wai Tak Yip, Dr. Zhibo Yang, Dr. Yihan Shao, Dr. Elena I. Zgurskaya and Dr. Jun Li. Thanks for your time and advices for helping my study in the past several years.

I appreciate the friendship and happiness I gained from every valuable member of Dr. Mao's group, both current and former member. My special thank is given to Dr. Binrui Cao, Dr. Penghe Qiu and Dr. Lin wang. We have been working and laughing all those years since I came to OU at the first day.

At last, I would like to thank my parents for standing by me for whatever happened and my love Yueyi for being supportive for the most difficult three years. And for every person I have mentioned above, I appreciate your participation to share the great moment of my life as much as the precious study experience of my PhD years.

Table of Contents

Acknowledgements	iv
List of Tables	ix
List of Figures.....	x
Abstract.....	xii
Chapter 1: Introduction	- 1 -
1.1 General background	- 1 -
1.2 Types of breast cancer and treatments	- 1 -
1.3 Breast cancer targeting therapy	- 2 -
1.4 Peptide displayed phage library selection	- 4 -
1.4.1 Filamentary bacteria phage biology	- 4 -
1.4.2 Phage library and Biopanning	- 4 -
1.5 Properties of inorganic particles.....	- 5 -
1.5.1 Up-converting nano-particles (UCNPs)	- 5 -
.....	- 6 -
1.5.2 Properties of gold nanorods.....	- 7 -
1.6 <i>In vitro</i> 3D cultured cancer cell spheroids	- 9 -
Chapter 2 Multi-functionalized nanoparticles for cancer-targeting cell imaging and tubulin-	
interactive anti-cancer therapy	- 11 -
2.1 Introduction	- 11 -
2.2 Materials and Method.....	- 13 -
2.2.1 Cell line and chemical reagents	- 13 -
2.2.2 Synthesis of NaYF₄: Yb, Er upconverting nanoparticles (UCNPs)	- 13 -

2.2.3 Preparation of UCNPs/SiO ₂ core/shell nanoparticles	13 -
2.2.4 Surface modification of Silica-coated UCNPs	14 -
2.2.5 Enzyme-linked immunosorbent assay (ELISA) for evaluating the tubulin binding affinity of the selected phages.	15 -
2.2.6 Cell viability inhibition assay of TIP/CTP-UCNPs against SKBR-3 cells.	15 -
2.2.7 Microscopic imaging of UCNPs uptake by breast cancer cells.....	16 -
2.2.8 Live and Dead assay of SKBR-3 cells.....	16 -
2.3 Results	17 -
2.3.1 Characteristics of SiO ₂ -coated UCNPs.....	17 -
2.3.2 Evaluation of the identified tubulin binding peptide.	19 -
2.3.3 <i>In vitro</i> cell imaging with UCNPs.	21 -
2.3.4 Cytotoxicity of CTP/TIP-UCNPs against SKBR-3 cells	22 -
2.4 Conclusion and Discussion	29 -
Chapter 3 Guiding nanomaterials to tumors for breast cancer precision medicine: From tumor- targeting small molecule discovery to targeted nano-drug delivery to breast tumors	30 -
3.1 Introduction	30 -
3.2 Materials and Experiments.....	32 -
3.2.1 Cell line and MCF-7 tumor xenograft	32 -
3.2.2 <i>In vivo</i> phage display	33 -
3.2.3 <i>In vivo</i> fluorescence imaging.....	33 -
3.2.4 Synthesis of gold nanorods.....	34 -
3.2.5 Preparation of peptide conjugated tumor-homing AuNRs	34 -

3.2.6 Quantification of AuNRs tissue distribution through ICP-AES.....	35 -
3.2.7 Photothermal treatment of MCF-7 tumor.....	36 -
3.2.8 haematoxylin and eosin (HE) staining.....	36 -
3.3 Results.....	36 -
3.3.1 Biopanning against <i>in vivo</i> MCF-7 tumors.....	36 -
3.3.2 Live <i>in vivo</i> imaging of tumor-bearing mice.....	41 -
3.4.3 Characteristics of peptide modified AuNRs.....	43 -
3.4.4 <i>In vivo</i> biodistribution of tumor-homing AuNRs.....	44 -
3.4.5 Tumor targeting photothermal treatment.....	47 -
3.4 Conclusion and Discussion.....	50 -
Chapter 4 3D multiple cell spheroids in silica coated fungi network scaffolds.....	52 -
4.2 Material and method.....	53 -
4.2.1 Cell line and 3D cell spheroids generation.....	53 -
4.2.2 Preparation of silica coated <i>Penicillium</i> fungi network scaffolds.....	54 -
4.2.3 Light microscopy and phase contract microscopy.....	54 -
4.2.4 Cell viability assay of cell spheroid growing with or without scaffolds.....	54 -
4.2.5 Scanning electron microscopy (SEM) and Energy-dispersive X-ray spectroscopy (EDS).....	55 -
4.2.6 <i>In vitro</i> 3D multi-cell spheroids targeting peptide selection by phage library biopanning.....	56 -
4.3 Results.....	56 -
4.3.1 Structure of silica-coated Fungi scaffold.....	56 -

4.3.2 Size shrinkage in pre-SEM process	58 -
4.3.3 Statistics of 3D cultured MCF-7 cell spheroids.....	60 -
4.3.4 Cell viability assay of 3D cultured MCF-7 cell spheroids	64 -
4.3.5 Phage-antibody selection.....	66 -
4.4 Conclusion and Discussion	67 -
References	69 -
Appendix A: List of Abbreviations	85 -
Appendix B: List of Copyrights and Permissions	88 -

List of Tables

Table 3.1. 30 sequences were randomly picked and identified from the 3 rd round of <i>in vivo</i> biopanning.....	- 38 -
Table 3.2. 54 sequences were randomly picked and identified from the 4 th round of <i>in vivo</i> biopanning.....	41
Table 3.3. 162 sequences were randomly picked and identified from the 5 th round of <i>in vivo</i> biopanning.....	43
Table 3.4. Summary of peptide sequences and frequencies in the 3 rd to 5 th round of <i>in vivo</i> phage display against MCF-7 tumors.....	44
Table 4.1. Summary of peptide sequences and frequencies in both 3 rd and 4 th rounds of Ph.D.-12 phage display against <i>in vitro</i> MCF-7 tumors.	70

List of Figures

Figure 1.1. Diagram of targeted cancer therapy agents.....	3
Figure 1.2. The structure of M13 and fd phage.....	4
Figure 1.3. Photo of UCNPs solution excited by laser at 980nm and Illustration of the penetration depths for UV and NIR light.....	6
Figure 1.4. Typical architecture of the therapeutic UCNPs-based composite.	7
Figure 1.5. Illustration of photothermal therapy. and the most commonly employed AuNPs for photothermal therapy.	8
Figure 1.6. The effect of shape of the nanoparticles on cellular uptake.....	9
Figure 1.7. Summary of <i>in vitro</i> tumor culture techniques and applications.	10
Figure 2.1. Fluorescent spectrum and TEM images of UCNPs solution	18
Figure 2.2. Eveluation of tubulin-binding phages	20
Figure 2.3. The fluorescence imaging of SKBR-3 cells on the basis of 0.2 mg/ml of UCNPs.	24
Figure 2.4. Cell viability of SKBR-3 cells incubated in the presence of control or functionalized UCNPs at different concentration for 24 hours.	26
Figure 2.5. Microscopic images of Live/Dead cell imaging assay.....	29
Figure 2.6. Confocal-microscopic images of SKBR-3 cells incubated with different functional peptide modified UCNPs	30
Figure 3.1. Schematic description of the phage display-based breast cancer precision medicine.....	35
Figure 3.2. <i>In vivo</i> imaging for the detection of selective accumulation of tumor-homing peptides at the MCF-7 tumors.....	45

Figure 3.3. TEM image and UV-Vis spectrum of the as-synthesized AuNRs used for the photothermal treatment.	- 43 -6
Figure 3.4. DLS measurement of AuNRs with different surface ligands..	47
Figure 3.5. Blood circulation of AuNRs.	48
Figure 3.6. Organ distribution of AuNRs. Mice were sacrificed 1 day, 2 days, 3 days, 4 days and 5 days after the intravenous injection of 1 mg of AuNRs.	49
Figure 3.7. Photothermal treatment of MCF-7 tumors.....	52
Figure 4.1. Fungus template branched silica scaffolds..	60
Figure 4.2. EDS spectrum of empty silica-coated scaffold at day 0 and at day 7	61
Figure 4.3. SEM and LM images of the same sample of cell spheroids growing on the scaffold.....	63
Figure 4.4. SEM images of MCF-7 cell spheroids growing on silica-coated fungi network scaffolds at day 3 and day 7	64
Figure 4.5. Phase contrast images of cell spheroids growing in Corning ultra-low attachment surface 96 well plate for 7 days.....	65
Figure 4.6. SEM images of cell spheroids growing on silica-coated scaffold for 7 days after cell-seeding.....	66
Figure 4.7. Statistic of size distribution for the cell spheroids with or without scaffold being cultured for 7 days.....	67
Figure 4.8. Comparison of AlarmaBlue assay between <i>in vitro</i> cell spheroids with or without the presence of scaffolds.....	68
Figure 4.9. Microscopic images of 5×10^4 cells growing on scaffold for 7 days.....	68

Abstract

Precision medicine emphasizes the patient-specific formulation for treating diseases, especially cancer. For targeted cancer treatment, however, since the expression level of tumor receptors on each patient varies even for the same type of cancer, the ligand-receptor mediated approach does not seem promising for precision medicine. In this study, we first identified a tubulin-interactive peptide (TIP) from Tau protein that is a well-known microtubule binding protein. The TIP was attached on an up-converting nano-particle (UCNP) core with other functional peptides, including the SKBR-3 cell-targeting peptide that was selected via *in vitro* biopanning by our lab and cell penetrating peptide R8, to synthesize multi-functional nanoparticle complex CTP/TIP-UCNPs. We have demonstrated CTP/TIP-UCNPs for a potential tubulin interfering anti-cancer reagent, which could be specifically delivered to the breast cancer cells, interrupt the cellular microtubule function and finally killed the cells. To better apply the precision medicine on anti-breast cancer therapy, through *in vivo* biopanning, we first selected an MCF-7 breast tumor-targeting peptide, then tested the effectiveness of the as-selected peptide in tumor homing, and finally conjugated the peptide to a model photothermal drug, the gold nanorods, to achieve enhanced cancer killing efficacy. The peptides identified by phage display technique can guide the drug to tumors without the need of first knowing the exact receptors on the tumor, which will take significantly less effort to explore the patient-specific targeting molecules for precision medicine. However, we also developed the substitute of tumor-bearing model with low cost for tumor-targeting reagents discovery, the 3D cultured breast cancer cell spheroids, which can mimic the *in vivo* tumor microenvironment and have similar drug resistance to real tumor tissues rather than two dimensionally cultured cancer cells. The natural network structure of penicillium fungi was first used to develop biocompatible scaffold and

culture *in vitro* MCF-7 breast cancer cell spheroids. 3 advantages of our method were confirmed comparing to the other published 3D cell culture methods: 1. The template of the scaffold and the surface modification of it can be generated effortlessly; 2. Neither special devices, cell matrix and laboratory skill nor another type of helper cell is required for the spheroid growth; 3. The scaffolds have loose enough space for 3D cell spheroids to better proliferate than the same amount of cells growing without the scaffold in non-adherent culture dish, and also have enough strength to be easily transferred with a pair of tweezers. So that, the cell spheroids could be applied for the purpose those require multiple steps of solution changes such as gradient dehydration for SEM and paraffin embedding based histology analyses and phage display biopanning.

Chapter 1: Introduction

1.1 General background

Breast cancer has the second highest death rate among all the kinds of cancers for women in the U.S. About 12.4% of women will develop invasive breast cancer in their whole life, and another 3% women are projected to develop non-invasive breast cancer.¹ Fortunately, since 2002, breast cancer incidence rate started decreasing in both the U.S and Canada. The main reason is believed to be a reduced use of hormone replacement therapy (HRT), especially for women between the age of 50 to 69.² Unlike most other type of cancers, surgical removal of breast tumor will permanently damage the patient's female physique. Instead of such ineffective and potentially harmful surgery, my goal is to develop biocompatible nanomaterials to image, target and precisely kill breast cancer tumors.

1.2 Types of breast cancer and treatments

Breast cancer differs by the exact location of the tumor, and by the invasive types or the molecular subtypes. Different breast cancer types have different incidence rates and mortality rates among all human races of all ages. According to the breast cancer statistics on 2013³, the overall incidence rate is similar between non-Hispanic white and African American women aged younger than 60 by 2010 and significantly higher in non-Hispanic white women than African American women aged elder than 60. But for the estrogen (ER)- type of breast cancer, the incidence rate is significant higher in African American women than non-Hispanic white of all age. However, for Hispanic women the incidence rate of either ER+ or ER- breast cancer is the lowest among all women of all age. The mortality rate of overall breast cancer from 2006 to 2010 for African American Women was about 30.8%, which is the 7.9% higher than non-

Hispanic white women and more than twice higher than Hispanic women. Although many factors might cause a woman to develop breast cancer or help her survive it, age is the most important factor influencing both the incidence rate and mortality rate. Including in situ and invasive breast cancer, the incidence rate among women aged beyond 50-year-old is three times higher (75.0% of 309,860 cases) than those aged younger than 50 (25% of 309,860 cases); the patients older than 50 have a double risk of death (30%) than younger patients (15%); among women aged older than 50 in comparable number of breast cancer cases, the mortality rate of the ones aged over 65 is almost twice higher (18.8% of 121440 cases) than those age between 50- and 64- year-old (10.8% of 110980 cases).⁴ Without any doubt, an optimal therapy specific for the diagnosed breast cancer subtype will ensure the best chance of survival for the patient.

1.3 Breast cancer targeting therapy

In cancer targeting therapy, a medicine interferes the tumor growth, progression or spread through any of the following ways: i) a cytotoxin or chemo drug is specifically delivered into the tumor sites⁵⁻⁶; ii) the drug attacks a specific cancer associated molecule;⁷⁻⁹ or iii) the drug is only active or being activated in the tumor sites.¹⁰⁻¹² Comparing to the common chemo therapy, the targeted cancer therapy might show an enhanced anti-cancer ability as well as possibly less side effect due to the precise treatment against the tumor sites. For the cancer-specific drug delivery approaches, the delivery system usually contains three components: the anti-cancer drugs, the organic vehicles or inorganic nano-carriers and tumor-targeting molecules (Figure 1.1). In some conditions, the nanocarriers also play the role of anti-cancer drugs such as gold-nanorods and quantum dots. The nano-carriers, including inorganic, organic and highly branched polymers, all showed one or more of these advantages: decrease of cytotoxic to normal cells, increase in the circulating time or half-life of the drug, controllable release, tunable size and surface properties,

etc.¹³⁻¹⁶ The most important portion of the targeted cancer therapy is the tumor-targeting agent. Monoclonal antibody (mAb) is the most well-known cancer delivery agent with high specificity to tumors and many clinical approval members.¹⁷⁻¹⁹ Phage display-derived (antibody phage display, APD) mAb became another promising tumor-targeting agent with comparable tumor-specificity as regular mAb since the first APD mAb was approved for therapeutic use in 2007.²⁰

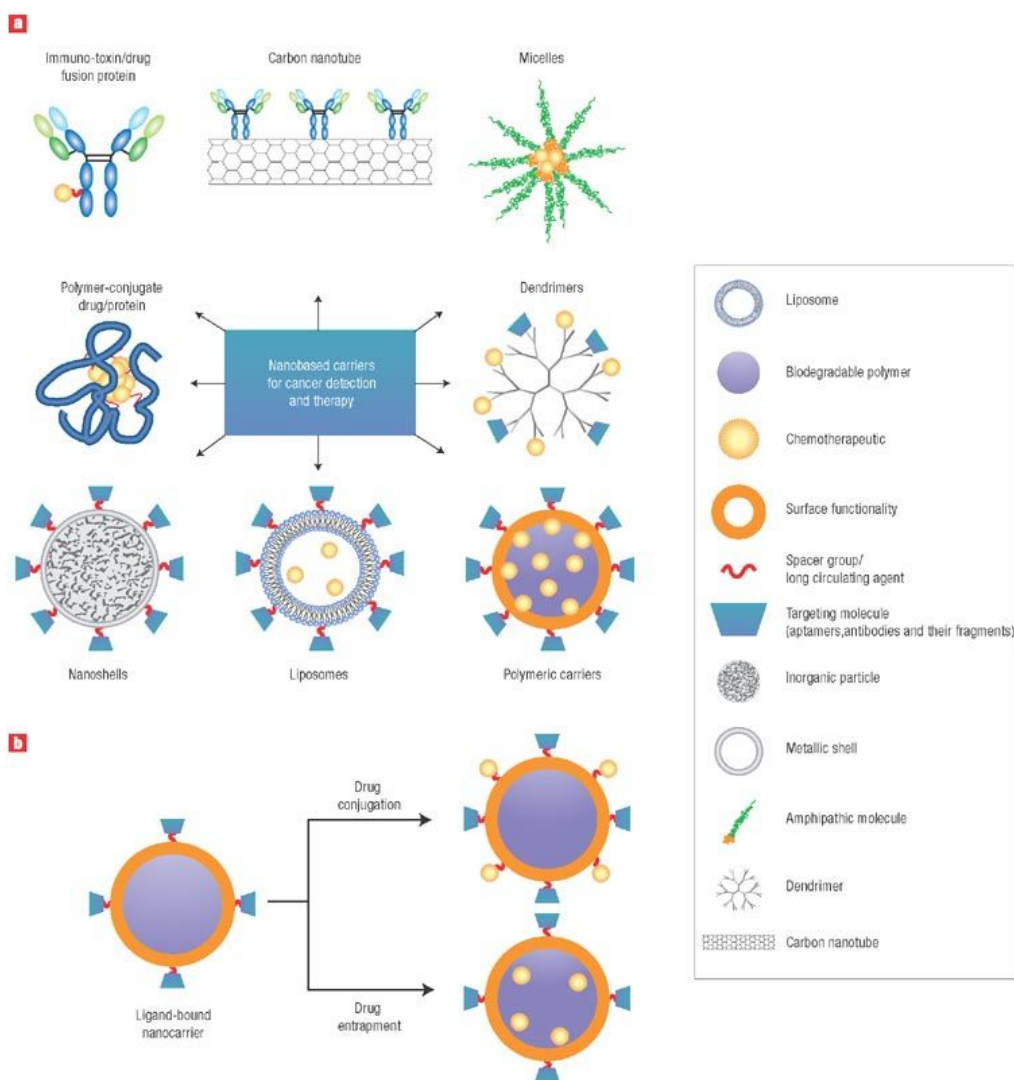


Figure 1.1. Diagram of targeted cancer therapy agents (a) and schematic diagram of drug-loading methods (b).²¹ Most types of agent contain three components: targeting agent, drug carrier and anti-cancer agent.

1.4 Peptide displayed phage library selection

1.4.1 Filamentary bacteria phage biology

Filamentary bacteria phage (Ff) including M13, fd and f1, is a type of *Escherichia coli* (*E. coli*) K12-infecting phage, with the long filamentary shape (6-7 nm × 500-1000 nm) and a single strand DNA (ssDNA, 6407-6408 bases) genome. They share about 98% identical DNA sequence and very similar coat proteins, thus they can be studied and applied interchangeably. There are 5 types of coat proteins for Ff phages: the major coat proteins pVIII (~2700 copies) and four minor coat proteins pIII, pVI, pVII and pIX (5 copies for each protein, Figure 1.2).^{1, 22-23}

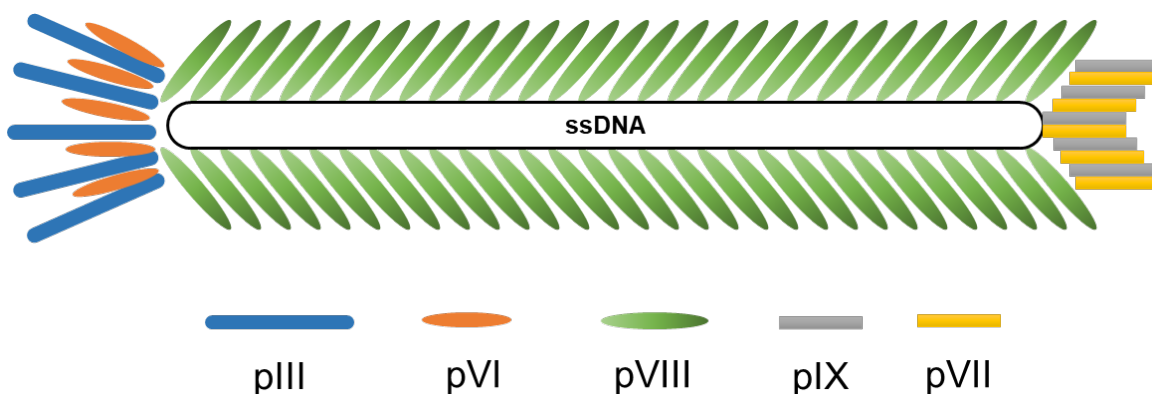


Figure 1.2. The structure of M13 and fd phage.

1.4.2 Phage library and Biopanning

All five coat proteins can be genetically engineered to display exogenous peptides, however pVIII and pIII are the most common position for peptide display without effecting their life cycle. By modifying the surface proteins of Ff phages, they could be used for many applications, including nanotechnology template, bio-functional nanofibers and the most significant contribution phage display.²⁴⁻²⁷ Phage display technique enables the application of

phage display library, which contains billions of phages clones randomly displaying various of exogenous peptides.²⁸ For pIII displayed library, a relatively long peptide (12 to 15 residues) is displayed at all 5 copies of pIII proteins of phage. For pVIII display library, also called landscape library, the foreign peptide is displayed on every copy of pVIII protein.²⁸ The pVIII displayed peptide is relatively short (8 residues at most), however the amount of them is abundant.

During the biopanning process, billions of random peptide-displayed phages will competitively interact with the targets. Only those phages with high target affinity peptide will be selected and amplified. The biopanning process shares a similar principle as positive selection for T cell development and the product peptide of biopanning could be used to produce APD mAb. Thus, phage display biopanning is also called antibody phage display.²⁹⁻³⁰ The target of antibody phage display is wildly diverse, including inorganic and organic compounds, metal, polymers, cells, tissues and others.³¹⁻³⁴ The most common targets of phage biopanning are clinical associated biomarkers or tumor tissues. The identified peptides can be used as the target agent for the nanocarrier targeted cancer therapy system.

1.5 Properties of inorganic particles

1.5.1 Up-converting nano-particles (UCNPs)

The up-converting nano-particles (UCNPs) is a unique type of material that convert light at long wave length to short wavelength. For instance, the lanthanide doped UCNPs could convert near-infrared (NIR) light at 980nm to visible light (Figure 1.3A).³⁵ Since NIR can deep penetrate the biological tissue with low photodamage, the UCNPs are promising nanocarriers for photosensor drug³⁶ or *in vivo* imaging³⁷ (Figure 1.3B).

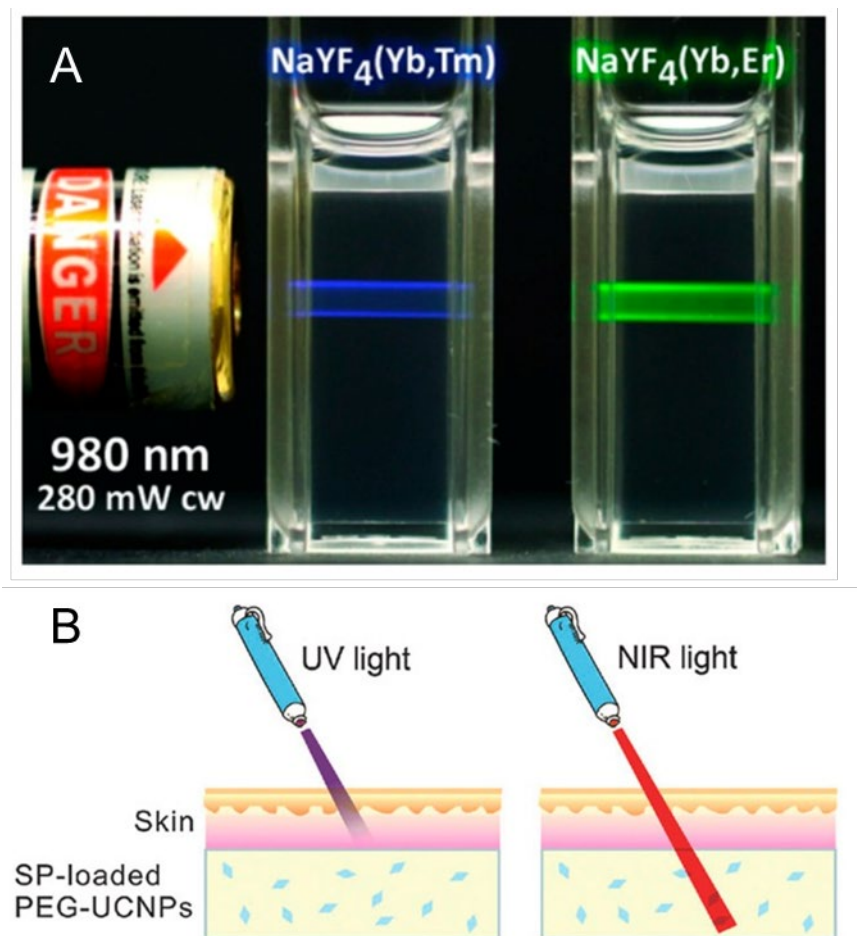


Figure 1.3. (A) Photo of UCNPs solution excited by laser at 980nm.³⁵ The doped lanthanide element ratio for blue UCNPs is ytterbium (Yb^{3+}): thulium (Tm^{3+}) = 25%: 0.3%; for green UCNPs is Yb^{3+} : erbium (Er^{3+}) = 20%: 2%. (B) Illustration of the penetration depths for UV and NIR light.³⁸

For targeted cancer therapy application, the UCNPs have several advantages: i). The UCNPs are safe with intravenous injection dose of 15mg/kg body weight both short-term and long-term trails.³⁹⁻⁴¹ Thus, the UCNP is an remarkable nanocarrier candidate for the exploring and studying unknown anti-cancer agents, or promising *in vivo* imaging agent for pre-clinical application. ii). The optical characteristic of UCNPs allows them to act as bifunctional

nanomaterial for *in vivo* study. The anti-cancer treatment and *in vivo* tumor imaging are possibly accomplished at the same time.⁴² iii). Surface of UCNPs can be modified by various of ligands at the same time, such as *in vivo* imaging enhancer, targeting agent, photothermal agent and others. It suggests that the UCNPs could be an ideal carrier candidate for multiple treatment purpose (Figure 1.4).⁴³

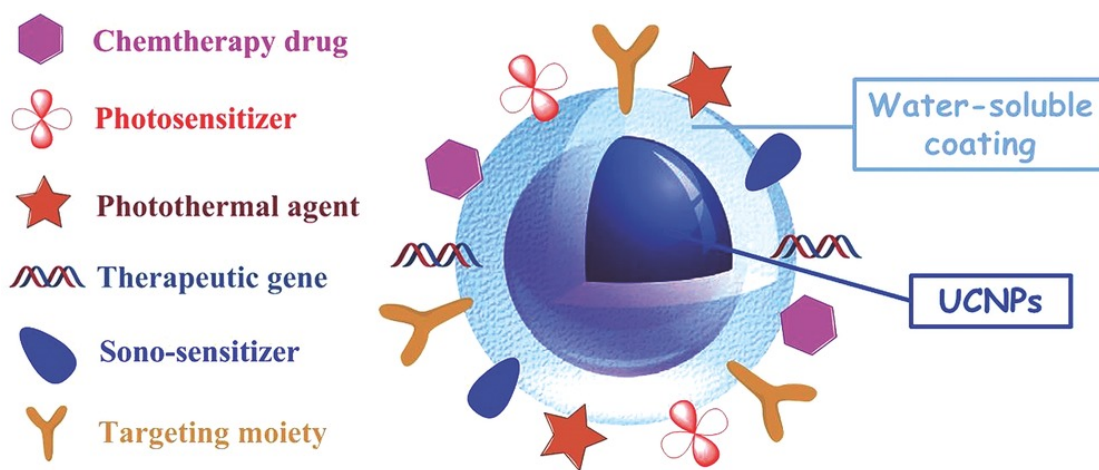


Figure 1.4. Typical architecture of the therapeutic UCNPs-based composite.⁴³

1.5.2 Properties of gold nanorods

Many types of gold nano-materials can be constructed to generate heat, including gold nanocages, nanorods, nanoshells and nanostars. Therefore, they are mostly employed for photothermal therapy (Figure 1.5).⁴⁴ Except the photothermal properties of gold nano-materials, each type of nano-particle has its own advantage. For example, the core-shell structure of nanoshells enhances the image contrast;⁴⁵ the nanostars have large surface area for ligand conjugation or absorption;⁴⁶ the cavity of nanocages allow the nano-carriers to load a large number of drug, slow release and increase the circulating half-life of the drug.⁴⁷ Overall, the photothermal property and other special characteristic of gold nanoparticles makes them at least dual targeting/ killing ability against cancer cells without needing of extra anticancer agents.

Comparing to those gold nano-materials, nanorods have the highest length/width ratio, which makes nanorods different in two following ways: i). The excitation and emission spectrum of nanorods is narrow;⁴⁸ ii). The cellular uptake of gold nanorods is significantly low (Figure 1.6).⁴⁹ For better applying targeted cancer therapy, the relatively low cellular uptake of non-specific nanorods decreases the distribution of drugs in healthy tissue and protect those organs and tissues from side effects.

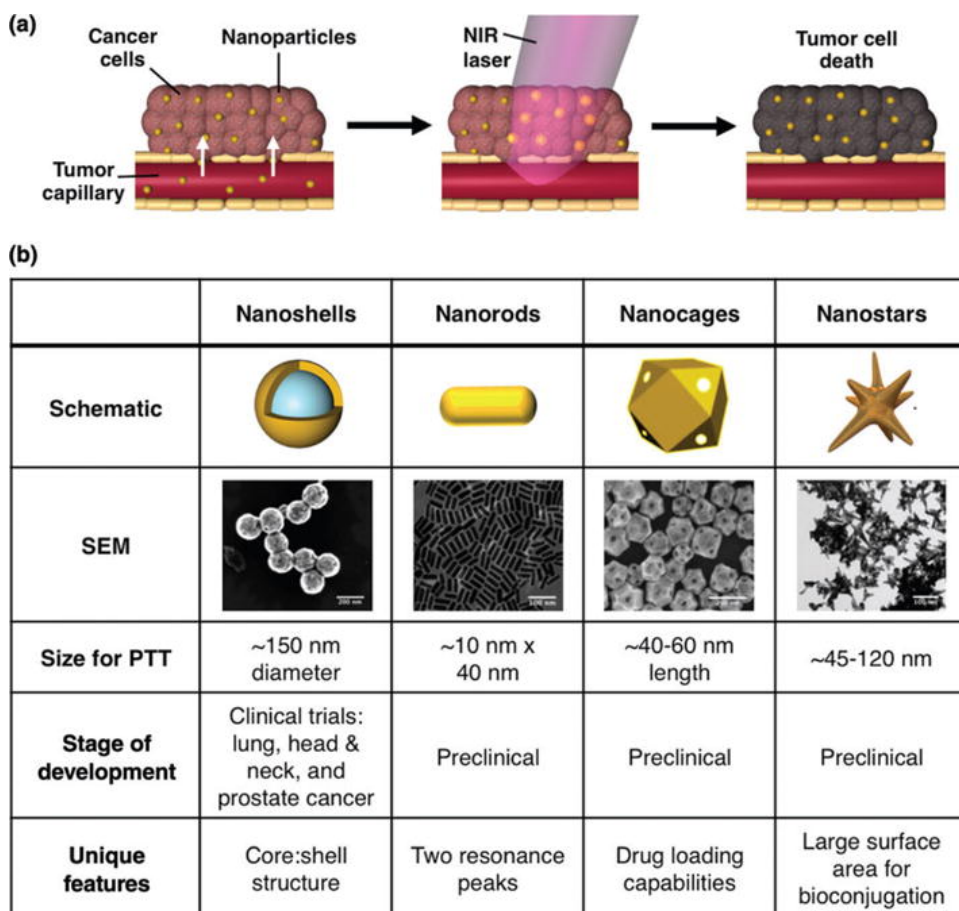


Figure 1.5. (a) Photothermal therapy. (b) Four of the most commonly employed AuNPs for photothermal therapy.⁴⁴

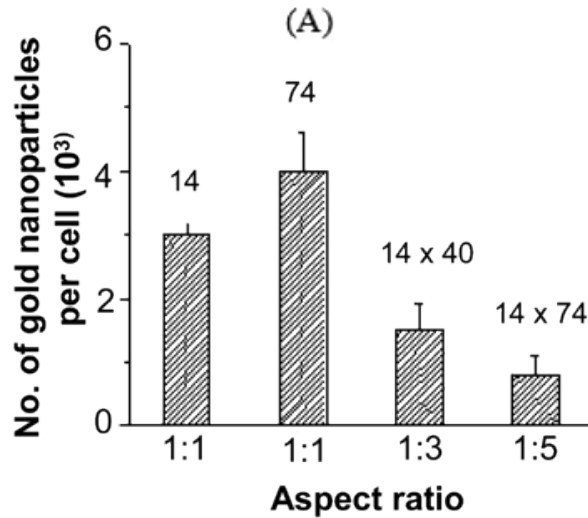


Figure 1.6. The effect of shape of the nanoparticles on cellular uptake.⁴⁹ When the aspect ratio equals to 1, the cellular uptake of nanoparticles with 74 nm in diameter is higher than with 14 nm in diameter. When one dimension of nanoparticles is fixed to 14 nm, the longer for the other dimension, the lower the cellular uptake is.

1.6 *In vitro* 3D cultured cancer cell spheroids

2D cultured cells, which is also called monolayer cell culture, were attached on the surface of the culture dish. Either the cellular morphology or the cell-cell interaction is different from the real *in vivo* tumors. Comparing to 2D cell culture, *in vitro* 3-dimensionally growing cancer cell spheroids, also called *in vitro* tumors show higher drug resistance and unhomogeneous biology profile, which are much closer to the real solid tumor tissues.⁵⁰⁻⁵⁷ Thus, for *in vitro* anti-cancer drug research, 3D cultured cell spheroids are the ideal models. There are several methods for generating 3D cultured cell spheroids, growing cells in non-adherent surface cell culture dish⁵⁸⁻⁶⁰ or microfluidic platform⁶¹⁻⁶³, hydrogel matrix made of collagen fibers or others^{57, 64-66}, hanging drop of medium⁶⁷⁻⁶⁸ or coculture the cancer cells with endothelial cells or stem cells (Figure 1.7).⁶⁹

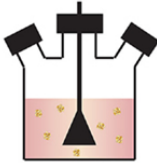
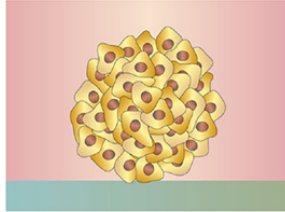
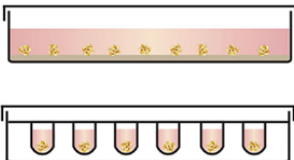
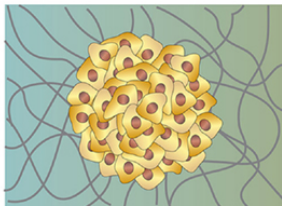
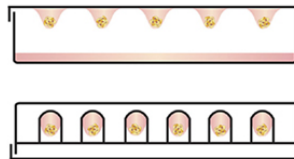
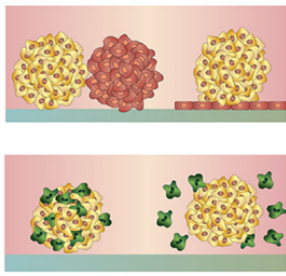

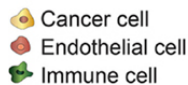
Spheroid Formation	Experimental Setup	Variables	Outputs
Suspension/Spinner Flasks 	Spheroids in Media 	Proliferation/ Migration/Invasion	Characterization of spheroid composition, growth and proliferation Protein and gene expression changes Migration and invasion assays
Liquid Overlay Technique Non-adherent Surfaces 	Spheroids in Matrix 	Drug Screening	Characterization of spheroid composition, growth and proliferation Protein and gene expression changes Survival assays Efficacy, distribution and accumulation of therapeutics
Hanging Drop Technique 	Coculture Spheroids 	Angiogenesis	Characterization of spheroid composition, growth and proliferation Protein and gene expression changes (i.e. angiogenic factors) Migration and invasion assays Angiogenesis assays
Microfluidic 		Immune Cell Response	Characterization of spheroid composition Protein and gene expression changes Adhesion assays Infiltration of immune cells into spheroids Migration and extravasation assays

Figure 1.7. Summary of *in vitro* tumor culture techniques and applications.⁷⁰

Chapter 2 Multi-functionalized nanoparticles for cancer-targeting cell imaging and tubulin-interactive anti-cancer therapy

2.1 Introduction

Tubulin proteins are monomeric proteins of microtubule (MT), which is one crucial type of structure of cellular skeleton. By polymerizing to MTs and dispolymering to tubulins, tubulin proteins play an important role in most cellular activities, including plasma transportation, cell immigration and karyokinesis cycles. Aggressive cancer cells are high proliferated cells with extremely active pathological cell mitosis. Thus, many tubulin interactive reagents were clinically applied as anticancer drugs. Generally, the tubulin interactive reagents interfere with the microtubule behavior in two typical ways, inhibiting the tubulin polymerization or promoting it. Either way would disable the cellular MT dynamics, interrupt the cell mitosis and finally cause cell apoptosis.⁷¹⁻⁷² As the polymerization inhibitor, bisindole alkaloids vinblastine and vincristine were the first clinical used nature-produced tubulin interactive anticancer medicine since 1960s, which bind to β -tubulin and prevent MT assembly.⁷³⁻⁷⁵ On the opposite, paclitaxel, or taxol as it was also called, was found to promote the tubulin polymerization and show significant clinical activity for refractory ovarian cancer and refractory breast cancer around 1990.⁷⁶⁻⁷⁹ Therefore, study of developing tubulin interactive agents will improve the anticancer therapy in the future.

However, the anti-tubulin type of agent influent not only the cancer cells but also the normal cells due to the non-specific uptake of cells, including toxicity of proliferating cells and neural system.⁸⁰⁻⁸¹ Developing cancer targeting tubulin interactive anticancer agents is a

promising way to minimize the side effect.⁸² In this study, we conjugated the lanthanide-doped up-converting nanoparticles (UCNPs) with three functional peptides, tubulin-interactive peptide (TIP), cancer cell-targeting peptide (CTP), and cell penetrating peptide R8⁸³⁻⁸⁵ to build a multi-biofunctional nanoparticles (CTP/TIP-UCNPs). The peptide DGSIPWST were selected as SKBR-3 binding agents from landscape phage library biopanning in our lab⁸⁶, showing significant cancer cell binding affinity and was used as the cancer-targeting portion of multifunctional nanoparticles. Five potential tubulin-binding peptides were selected from phage library biopanning too.⁸⁷ However, none of those tubulin-interactive candidates showed promising microtubule-function and cell viability interference. Thus, we picked a 15 residues peptide VQIINKKLDLSNVVQS from the microtubule binding domains of tau protein and used as an cytotoxic tubulin-interactive peptide (TIP) reagent.⁸⁸ Although tau is a well-known microtubule-associated protein, the peptide itself has never been approved or used as tubulin-interactive anti-cancer drug in any current report. The *in vitro* microtubule assembly assay confirmed remarkable tubulin-binding ability of both TIP and TIP modified UCNPs. The further assays including cell viability assay, confocal-imaging and *in vivo* anti-tumor test determined that the multi-biofunctional nanoparticles CTP/TIP-UCNPs could effectively kill the breast cancer cells, interfering microtubule functions and inhibit the *in vivo* tumor growing on an animal model. In sum, the CTP/TIP-UCNPs showed promising specific anti-microtubule activity and potential to be applied as anti-cancer reagent in further preclinical research.

2.2 Materials and Method

2.2.1 Cell line and chemical reagents

Human breast cancer cells SKBR-3 (ATCC Org.) were cultured in Dulbecco's Modified Eagle Medium (DMEM, ATCC Org.) with 10% fetal bovine serum (Gibco Inc.) at 37°C with 5% CO₂.

2.2.2 Synthesis of NaYF₄: Yb, Er upconverting nanoparticles (UCNPs)

To synthesize NaYF₄:18%Yb, 2%Er UCNPs, we modified the method described in several reports based on our own experience.⁸⁹⁻⁹⁰ All the chemical reagents used in this section were purchased from Sigma-Aldrich Inc. First, NH₄F (0.37 g, 10 mmole) and NaOH (0.40 g, 10 mmole) were mixed with 27.5 ml of oleic acid and 22.5 ml of 1-octadecene (ODE) in a 100 ml three-neck, heated to 110 °C under vacuum for at least 30 min, stirring until the solid completely dissolved. Then, the mixture of chloride compounds of the rare earth elements including YCl₃·6H₂O (606.72 mg, 2 mmole), YbCl₃·6H₂O (174.37 mg, 0.45mmole) and ErCl₃·6H₂O (19.08 mg, 0.05mmole) were added in the above solution, kept string at 110 °C under vacuum until a clear solution was formed. And afterwards, the solution was heated to 300 °C under vacuum for 30 min. The prepared UCNPs were collected washed for 3 times by acetone. Finally, they were dispersed in cyclohexane for storage.

2.2.3 Preparation of UCNPs/SiO₂ core/shell nanoparticles

The concentration of as-prepared UCNPs in cyclohexane were adjusted to 0.5 mg/ml. The water-in-oil microemulsion was then prepared by mixing together 50 µl of IGEPAL CO-520 (Polyoxyethylene (5) nonylphenylether, Sigma-Aldrich Inc.), 10 µl of 38% ammonia hydrate for 1 ml of cyclohexane dispersion of UCNPs. The mixture was sonicated for 10 min and then vigorously stirred for about 30 min to form a stable inverted microemulsion. Afterwards, 5 µl of

tetraethoxysilane (TEOS, Sigma-Aldrich Inc.) were added to the mixture to initiate the hydrolysis reaction. After 12 h to 16 h of reaction, the silica coated UCNPs were destabilized and precipitated by adding acetone to the microemulsion. The nanoparticles were then washed repeatedly by ethanol and water, and finally dispersed into ethanol for storage.

2.2.4 Surface modification of Silica-coated UCNPs

The silica-coated UCNPs in ethanol were first precipitated and resuspended into ethanol/water mixed solvent (4:1 v/v). at the concentration of 1 mg/ml. Then, 20 μ l of 38% ammonia hydrate, 2mg mPEG-Silane (Methosy PolyEthyleneGlycol-Silane, Biochempeg Scientific Inc.) and 0.5 mg Silane-PEG-COOH (Silane-PolyEthyleneGlycol-Acetic Acid) were added subsequently into 1 ml of the solution. The mixture was vigorously stirred for 12 h to 16 h. And afterwards, a wash step of ethanol was applied to remove the unbound PEG. To active the carbohydrate group on the surface of PEG deposited silica-coated UCNPs, the particles were suspended in MES buffer (0.1M of 2-(N-Morpholino) ethanesulfonic acid, PH=4) and added by 0.03 mg NHS (*N*-Hydroxysuccinimide, Sigma-Aldrich Inc.) and 0.10 mg EDC (*N*-(3-Dimethylaminopropyl)-*N'*-ethylcarbodiimide hydrochloride, Sigma-Aldrich Inc.) per 1 mg of particles and reacted for 15 min at room temperature. And then the active particles were immediately precipitated and resuspended into 1 ml of Phosphate buffered saline (PBS) and added by 50 μ l of 5 mM desired peptide (Peptide 2.0 Inc.). The peptide conjugation was allowed to continue for 5 hours at 4°C. Finally, the peptide modified particles were centrifuged and dispersed to desired concentration in serum free cell medium.

2.2.5 Enzyme-linked immunosorbent assay (ELISA) for evaluating the tubulin binding affinity of the selected phages.

The five tubulin-binding phages were incubated with E.coli K91 BlueKan cells and tetracycline overnight at 37 °C with shaking. Then centrifugation was applied to remove bacteria cells in the culture medium and the phage particles in the supernatant were purified by double precipitation with PEG/NaCl (3% PEG, 3.75M sodium chloride). Five liters of each type of phage were amplified and purified. The concentrations of phage were measured by measuring optical density (OD) at 269 nm. To conduct ELISA, identical number of potential tubulin binding phages or wild type phages were first coated on a 96-well plate. After surface blocking of the phages by 0.5% bovine serum albumin (BSA) solution, the biotinylated tubulin was added to each well and incubated with the phages for an hour followed by washing away the unbound tubulin with PBS for three times. Then the bound tubulin proteins were linked with streptavidin labeled by Alkaline Phosphatase (ALP, ThermoFisher Scientific Inc.), an enzyme that can quantitatively convert p-Nitrophenyl Phosphate (pNPP, ThermoFisher Scientific Inc.) to a soluble yellow product which can be quantified at 205 nm. Five repeats were employed for each type of phages to exclude the random error.

2.2.6 Cell viability inhibition assay of TIP/CTP-UCNPs against SKBR-3 cells.

The AlamarBlue assay was applied for semi-quantifying the cell viability inhibition of TIP/CTP-UCNPs against cancer cells. SKBR-3 cells were incubated with TIP/CTP-UCNPs and control groups those include R8-UCNPs, TIP-UCNPs and negative control, at a series of concentration of 0.25, 0.5, 1.0 and 2.0 mg/ml respectively for 24 hours. And afterwards, the unbound particles and old medium was removed and 200 µl of pre-mixed assay medium (20 µl of AlamarBlue reagent was added in 180 µl of serum-free EMEM medium) were added in each

well and cultured at 37 °C for 3.5 to 4 hours in the cell incubator. Finally, the absorption at 570 nm and 600 nm of each well was measured by plate reader. The cell viability was normalized by the negative control group.

2.2.7 Microscopic imaging of UCNPs uptake by breast cancer cells

For normal microscopic images of UCNPs uptake cells, the cells were first cultured in 24 well plate for 24 hours to perform good cell behavior. For confocal microscopy measurements, the cells were cultured in 8 well chamber slides. Then the test peptide modified UCNPs with different concentrations were added to replace the old medium and incubated with the cells at 37 °C for 16 to 24 hours. After removal of the unbound UCNPs and the old medium, the cells were washed for 5 times with warm PBS buffer and fixed with 4 % of paraformaldehyde (PFA, w/v, in PBS) for 15 min at room temperature. For immunofluorescence staining of microtubule, the fixed cells will be treated with 0.1 % of Triton X-100 (v/v, in PBS) for 10 to 15 min on ice to penetrate the cell membrane. And afterwards, 1 % of BSA (w/v, in PBS) was added into the well, blocking the cells for 2 hours at 4 °C following by adding mouse anti- α tubulin antibody (Abcam. Inc) and incubating at 4 °C for 12 h. After a wash step of PBS buffer for 5 times, Alexa Fluor 555 labeled donkey anti-mouse IgG secondary antibody (Abcam. Inc) was added and incubated with cells for 1 h in the dark. Finally, the cells were washed with PBS for 6 times and mounted by cover slip with a drop of Glycerol mounting medium with 4',6-diamidino-2-phenylindole (DAPI, EMS. Inc).

2.2.8 Live and Dead assay of SKBR-3 cells

The cells were cultured in 24 well plate for 24 hours to maintain good cellular behavior and then incubated with different concentration of TIP/CTP-UCNPs, TIP-UCNPs or Ctrl-UCNPs individually for 24 h. Then the Live/Dead cell imaging kit (ThermoFisher Scientific Inc.) was

employed for fluorescent stain live cells and dead cells separately. Briefly, the two components, Live Green and Dead Red were thawed, mixed and added to the same volume of cell medium. The cells were ready to image after 15 min of incubation at room temperature.

2.3 Results

2.3.1 Characteristics of SiO₂-coated UCNPs

The fluorescent intensity spectrum of our UCNPs showed the major peak at 540nm and the minor peak at 525 nm, when the UCNPs were excited by laser at 980 nm (Figure 2.1A). Meanwhile, strong green fluorescence can be seen (Fig. 1A inset). The TEM images of UCNPs and SiO₂-coated UCNPs are shown in Figure 2.1B and C respectively. We demonstrated that the average size of uncoated spherical UCNPs or the core UCNPs was 40 ± 4 nm and the thickness of SiO₂ shell is about 7-8 nm.

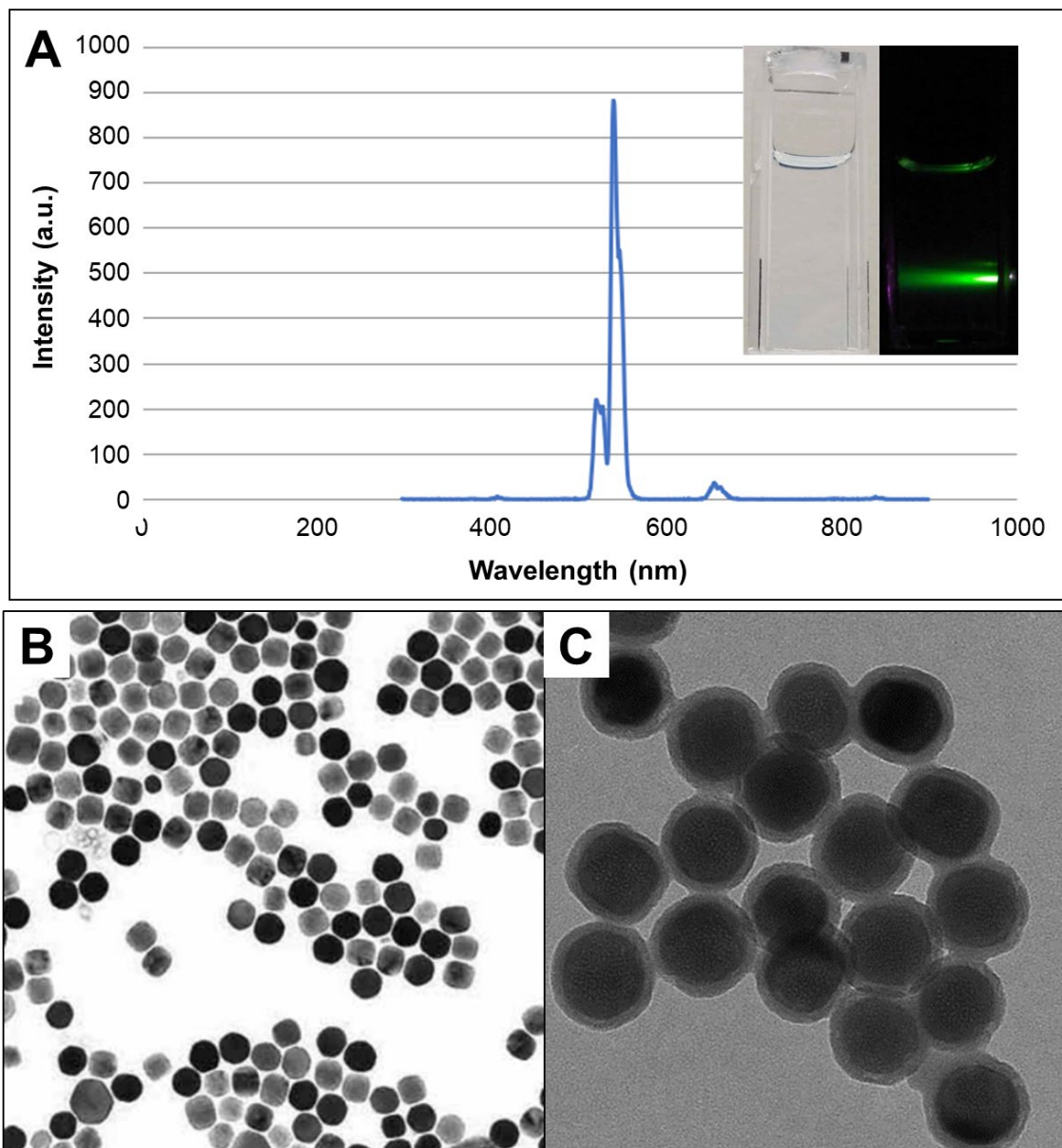


Figure 2.1. A: Fluorescent spectrum of UCNPs solution excited at 980 nm. Inset images: photographs of UCNPs under white light (left) and 980 nm laser irradiation (right). B: transmission electron microscope (TEM) image of uncoated sphere UCNPs. C: TEM image of SiO₂ coated UCNPs, core/shell structure. The scale bars indicate 100 nm for both TEM images.

2.3.2 Evaluation of the identified tubulin binding peptide.

The enzyme-linked immunosorbent assay (ELISA) was employed to evaluate the tubulin binding affinity of the selected phages (Figure 2.2A). The optical density of the final solution at 405 nm indicated the relative tubulin binding capability of the phages. Comparing to the wild type phage, all the selected phages showed remarkably higher affinity to tubulin (Figure 2.2B), and the sequences T1, T3 and T5 were considered as the most promising tubulin binding phage due to the highest OD value. Then, the tubulin polymerization assay was employed to monitor how the selected tubulin-binding phages, T1, T3 and T5 will influence the normal process of the assembly of into microtubules. The polymerization process⁹¹ was tracked by measuring the optical density (OD) of the solutions at 340 nm. Under the experimental condition, OD₃₄₀ of 0.1 is approximately equal to a microtubule concentration of 1.0 mg/ml. Paclitaxel, which is a strong inducer for tubulin polymerization⁹²⁻⁹⁴, was also used for control experiments. It can be seen from the polymerization assay that the phages with T3 sequence (green line) can promote tubulin polymerization as well as the paclitaxel, while the promotional effect was not as significant by phages displaying T1 and T5 sequences. Thus, the T3 phages were considered as the best tubulin-interactive reagents. However, since the tubulin-binding peptides must be delivered into the cytoplasm to play a role in interrupting the microtubule assembly behavior, and the cell penetrating ability of tubulin-binding phages is unknown, the cell viability assay was applied to find out if the tubulin-binding phages can pass through the cell membrane to enter the cells and affect cell viability. SKBR-3 cells were incubated with the tubulin-binding phages or the wild type phages in a 96 well plate for 48 hours, followed by the assay. Two different final concentrations of phage were added (2×10^{12} and 6×10^{12} virions/ml). Although the T3 peptide displayed phages showed the strongest microtubule assembly interference. Comparing to the

control group in which the cells were cultured in media without any phage, neither the wild type nor tubulin-binding phages can affect the cell viability (Figure 2.2C and D).

These above facts indicated: (1) Phage particles are harmless to cells even at a very high concentration (6×10^{12} virions/ml) and can be further used for *in vitro* or *in vivo* tests; and (2) Although the tubulin-interactive phages could significantly bind to the tubulin proteins, they could not interfere the cancer cell viability for following two possible reasons: i). Phages displaying only tubulin-interactive peptides on the side wall are not able to penetrate cell membrane to bind microtubules or free tubulins; ii). The interaction between the tubulin and the displayed peptide was not strong enough to interrupt the regular microtubule behavior due to the complex intracellular environment.

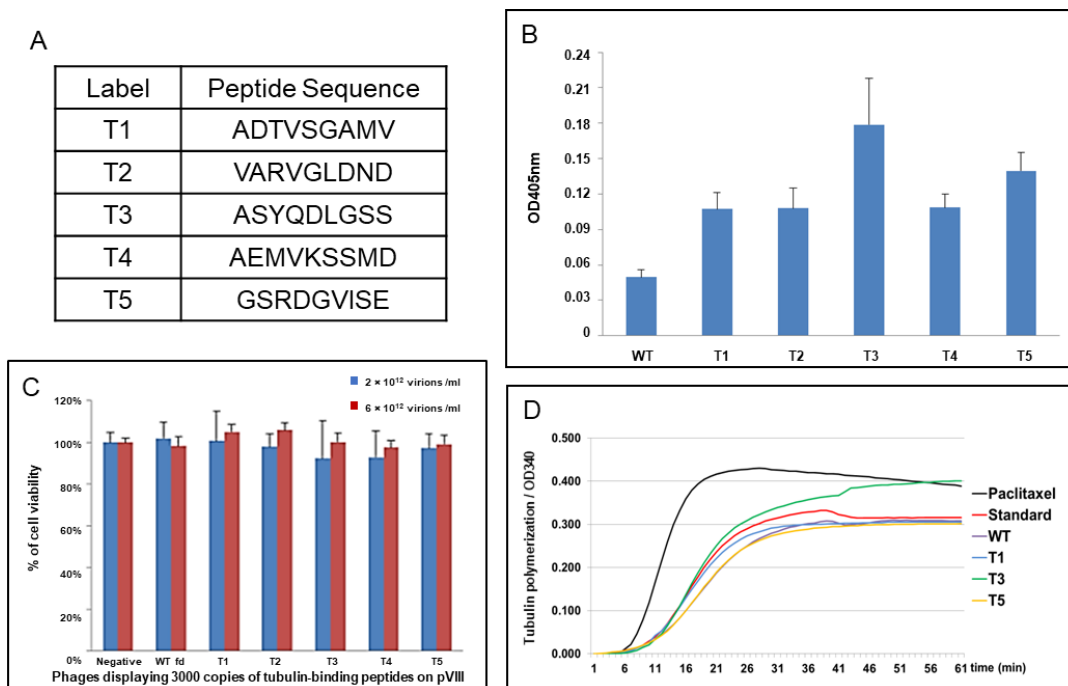


Figure 2.2. (A) Table showing the sequences of five tubulin-interactive peptide candidates. (B) Direct ELISA to detect the affinity between tubulin-binding phages and tubulin. Compared to wild type fd phage (WT), all the tubulin-binding phages showed higher affinity to tubulin

($p < 0.01$). This data shows that the phage displaying T3 peptide has the highest affinity. (C) Tubulin-binding phage showed no cytotoxicity to SKBR-3 cells. The cell viability was normalized by negative group. The final concentration of phage was 2×10^{12} (blue) or 6×10^{12} virions/ml (red). (D) The polymerization reactions in the absence of any drug (Standard) and in the presence of 10 μ M paclitaxel and with tubulin-binding phages (displaying T1, T3 or T5 peptides) or wild-type (WT) phages.

2.3.3 *In vitro* cell imaging with UCNPs.

The Peg-UCNPs were modified by only TIP or CTP, or by both peptides with the molar ratio of 1:1. SKBR-3 cells were incubated with each kind of UCNPs, including the Peg-UCNPs, with the concentration of 0.2 mg/ml in the 24 wells plate for 16 hours and then the images were captured by using the 980 nm laser as the excitation light source (Figure 2.3). The light intensity, optical length and the exposure time was consistent for all the photos. As we expected, the uptake of PEG-UCNPs is the lowest and hardly offers the visible fluorescence image. Although each kind of peptide conjugated UCNPs penetrated into the cells due to the cell internalizing function of the R8 sequences, the CTP linked nanoparticles apparently displayed the stronger fluorescence than the TIP-UCNPs. It is likely that the CTP plays a role to anchor the particles onto the cell membrane and increase the chance of endocytosis. Additionally, the TIP/CTP double functionalized nanoparticles showed the brightest green light. This exciting result suggested that the interaction between the cellular microtubules and the TIP might help the UCNPs retain in the cells after the uptake.

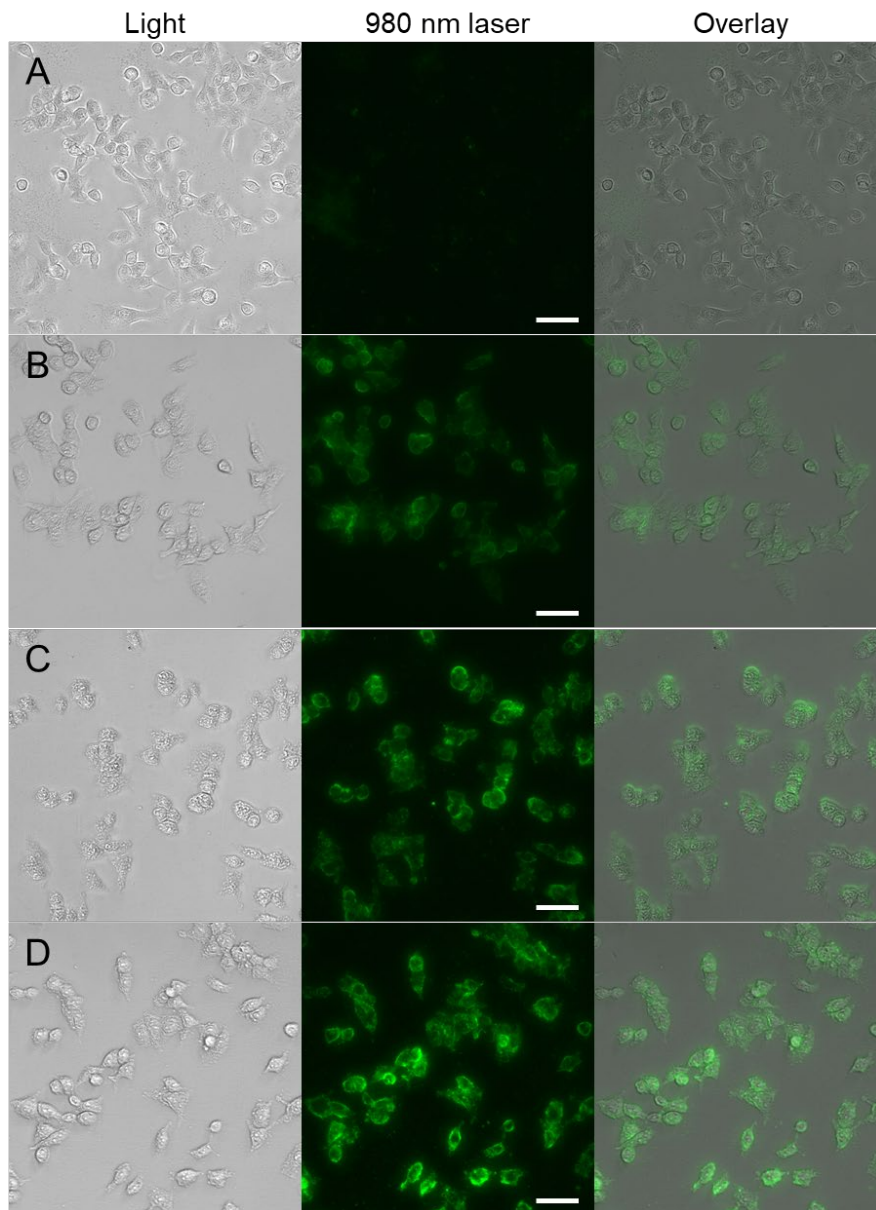


Figure 2.3. The fluorescence imaging of SKBR-3 cells on the basis of 0.2 mg/ml of UCNPs. (A) Peg-UCNPs, (B) TIP-UCNPs, (C) CTP-UCNPs and (D) TIP/CTP-UCNPs. The scale bar indicates 20 μ m.

2.3.4 Cytotoxicity of CTP/TIP-UCNPs against SKBR-3 cells

To Examine the cytotoxicity of CTP/TIP-UCNPs against the breast cancer cells, AlarmaBlue assay was applied to determine the half maximal inhibitory concentration (IC₅₀) of it against SKBR-3 cells. The Peg-UCNPs were conjugated with different combination of four

peptides: tubulin-interactive peptide (TIP), cancer cell-targeting peptide (CTP), cell penetrating peptide R8 and a random control peptide (Ctrl, WTDSIPGSGGGRRR). To enhance the microtubule assembly interference of CTP/TIP-UCNPs, the ratio of TIP: CTP: R8 was adjusted to 2: 1: 2. According to the relation between the molar mass and the mean diameter of UCNPs,⁹⁵ the estimated molar concentration of 1 mg/ml of UCNPs was 10 nM. Therefore, the theoretical ratio of peptides to particles was 500 to 1. Although the real amount of peptides attaching on the surface of a single particle was absolutely lower than 500, each portion of the modified peptide was able to functionalize the particles. For CTP-UCNPs and TIP-UCNPs, the corresponding portion of function peptides was replaced by control peptide. Both portions of CTP and TIP were replaced by control peptide for Ctrl-UCNPs. The same amount of R8 peptide were attached at each type of particles. For AlarmaBlue assay, the cells were incubated with Ctrl-UCNPs, TIP-UCNPs or CTP/TIP-UCNPs at concentration of 0.25 mg/ml, 0.5 mg/ml, 1.0 mg/ml or 2.0 mg/ml respectively, for 24 h. The cell viability without any interference was set as 100% (Figure 2.4). Overall, the control particles showed no inhibition to the cell growth at all concentrations and the cell viability was significantly inhibited by both type of tubulin-interacting nanoparticles, TIP-UCNPs and CTP/TIP-UCNPs groups. The inhibition of cell growth for either tubulin-interactive nano-particles showed linear increasing pattern from 10-13% to 22-34% as the concentration increased from 0.25 mg/ml to 2.0 mg/ml. However, the difference of cell viability between TIP-UCNPs and CTP/TIP-UCNPs groups was not significant when the concentration is as low as 0.25 mg/ml, but became greater since the concentration was equal or higher than 0.5 mg/ml. When the concentration of nano-particles was as high as 2.0 mg/ml, the cell viability inhibition of CTP/TIP-UCNPs was significantly lower than TIP-UCNPs with the difference of 12 %. According to the trendline of each group, the IC₅₀ of CTP/TIP-UCNPs against SKBR-3 cells

was 5.9 mg/ml that was significantly lower than 12.6 mg/ml of TIP-UCNPs and the IC₅₀ of Ctrl-UCNPs is incomputable. The cell viability assay exhibited the following three facts: the UCNPs appeared to be noncytotoxic to SKBR-3 cells; the TIP was able to inhibit the cell viability and the CTP could improve the cell viability inhibition of TIP.

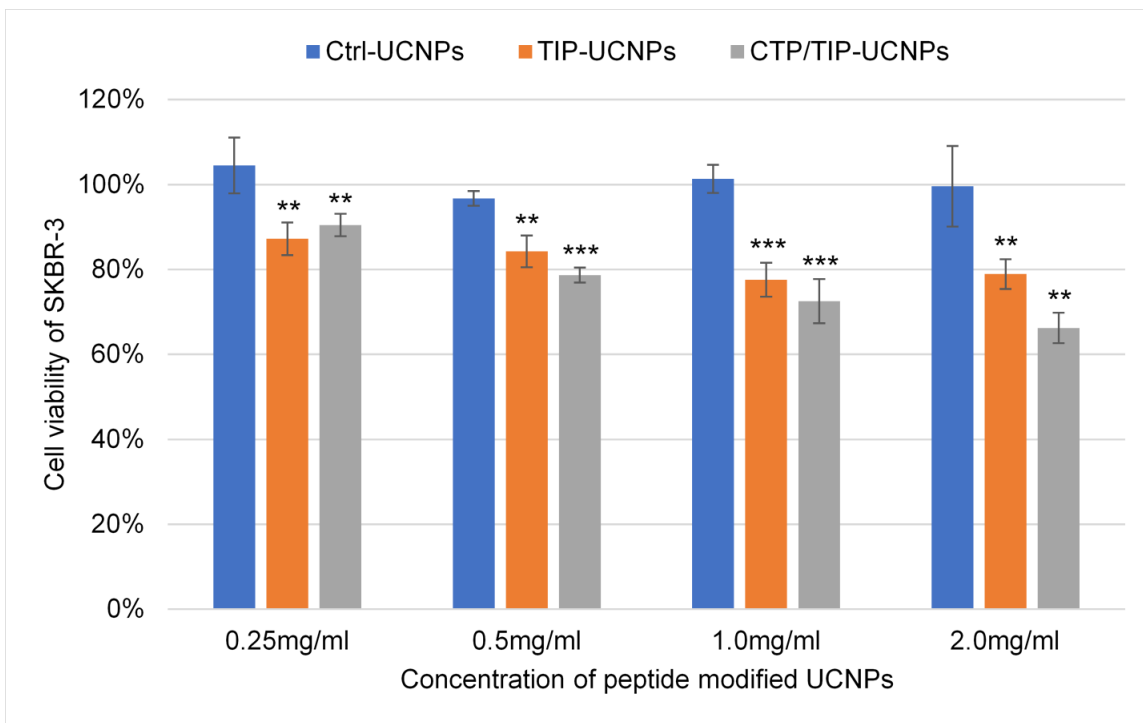


Figure 2.4. AlarmaBlue assay of SKBR-3 cells incubated in the presence of control or functionalized UCNPs at different concentration for 24 hours. The cell viability was normalized by the cell viability without any interference. * indicates P value between the test group to the corresponding control group: ** indicates $P < 0.01$; *** indicates $P < 0.001$.

To verify that if the cell viability inhibition of CTP/TIP-UCNPs was caused by cell death, SKBR-3 cells were incubated with or without 1 mg/ml of peptide modified UCNPs for 24 hours following by Live/Dead cell imaging stain to determine cell death (Figure 2.5). Without the presence of any nano-particles, dead cells were seldom found in the microscopic view. More

dead cells appeared in the presence of either Ctrl-UCNPs or CTP-UCNPs with no significant difference between each other group. However, the significant cell death was only observed for the cells incubating in the presence of tubulin-interactive peptide modified UCNPs, CTP/TIP-UCNPs and TIP-UCNPs. As I expected, the Live/Dead imaging assay verified that the TIP modified nanoparticles could significantly kill the breast cancer cells *in vitro*, and meanwhile, the deposit of CTP could greatly enhance the cytotoxicity of TIP modified nanoparticles.

Based on the previous results, we have determined that the tubulin-interactive peptide VQIINKKLDLSNVVQS specifically image and kill the breast cancer cells with the help of an imaging component UCNPs, a cell-penetrating peptide R8 and a cell-targeting peptide DGSIPWST. However, it is still unclear whether the TIP interfere the intracellular microtubule assembly to induce cell death. Therefore, the cells were imaged by confocal microscope to determine the tubulin polymerization and the morphological changes of cells. To prevent the cell detaching from the slides and to decrease the non-specific cell uptake of peptide modified UCNPs, the incubation time of cells and nanoparticles was reduced to 4 hours. At this time, most the cells were not yet in mitosis and still attached on the slide.⁹⁶ The confocal microscopic images showed that without the presence of TIP, all SKBR-3 cells, in negative, Peg-UCNPs, Ctrl-UCNPs and CTP-UCNPs groups, exhibited common cell morphology and regular microtubule polymerization (Figure 2.6A-D). For the cells incubated with TIP-UCNPs for 4 h (Figure 2.6E), the microtubule filaments disappearance⁹⁷⁻⁹⁸ was observed like the effect of nocodazole, which binds to the tubulin dimer and inhibits tubulin assembly.⁹⁷ With higher uptake of CTP/TIP-UCNPs due to the cell binding ability, the treating cells (Figure 2.6F) showed significant morphological change and microtubule depolymerization. The change of microtubule

structure was similar as the breast cancer cells treated by high dose of nocodazole.^{96, 99-100} The confocal microscopic images suggested that the TIP modified UCNPs could be uptake by the breast cancer cells and interfere the regular microtubule function by either inhibiting the microtubule assembly or promoting the microtubule depolymerization. The tubulin-interference ability of the peptide modified UCNPs will be greatly enhanced with the help of CTP modification.

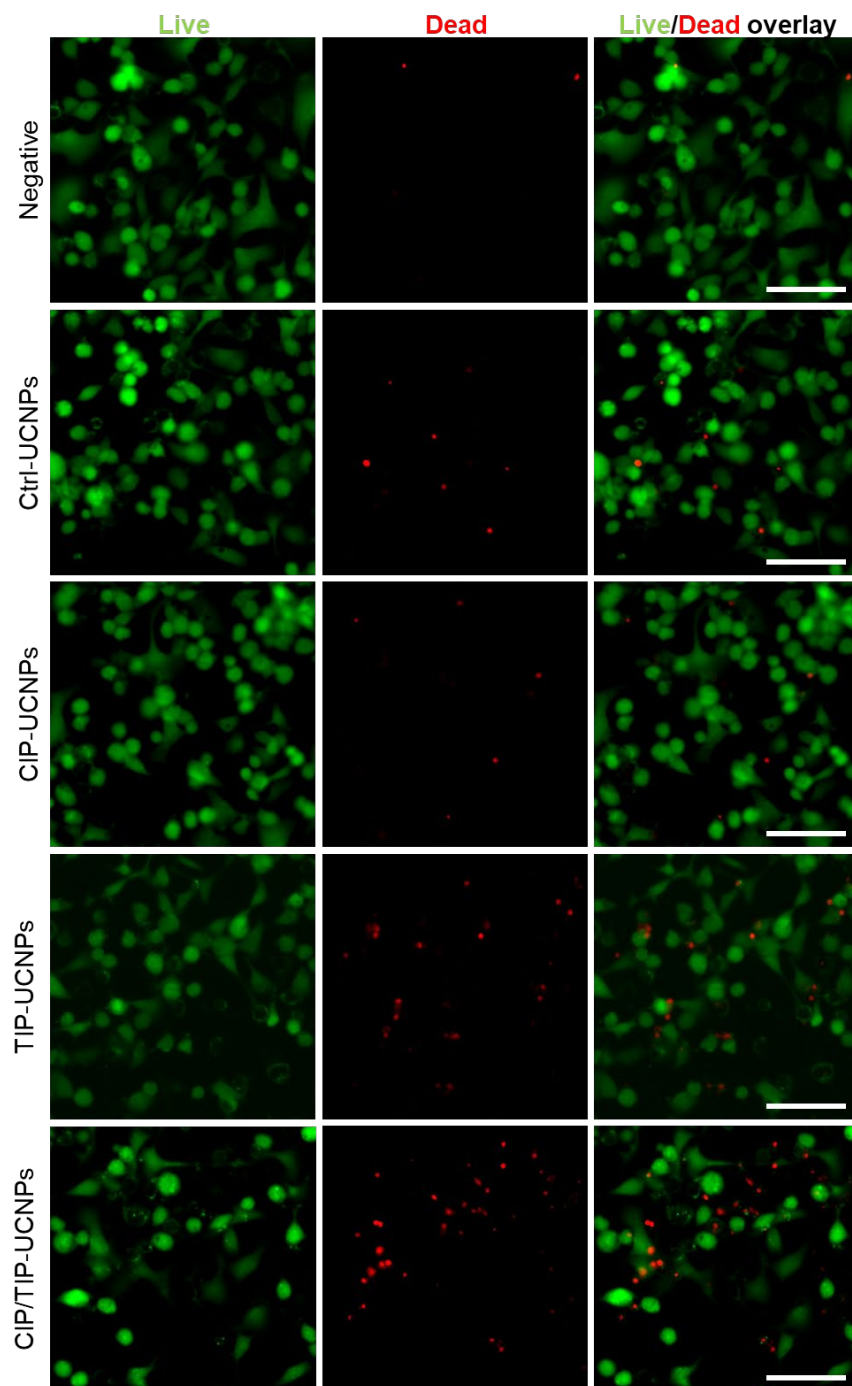


Figure 2.5. Microscopic images of Live/Dead cell imaging assay. The live cells were labeled by FITC fluorescent calcein (Green) due to the presence of ubiquitous intracellular esterase activity. DNA of the dead cells (Red) was indicated by Texas Red attached cell-impermeant component that only entered dead cells. The Scale bars indicate 100 μ m.

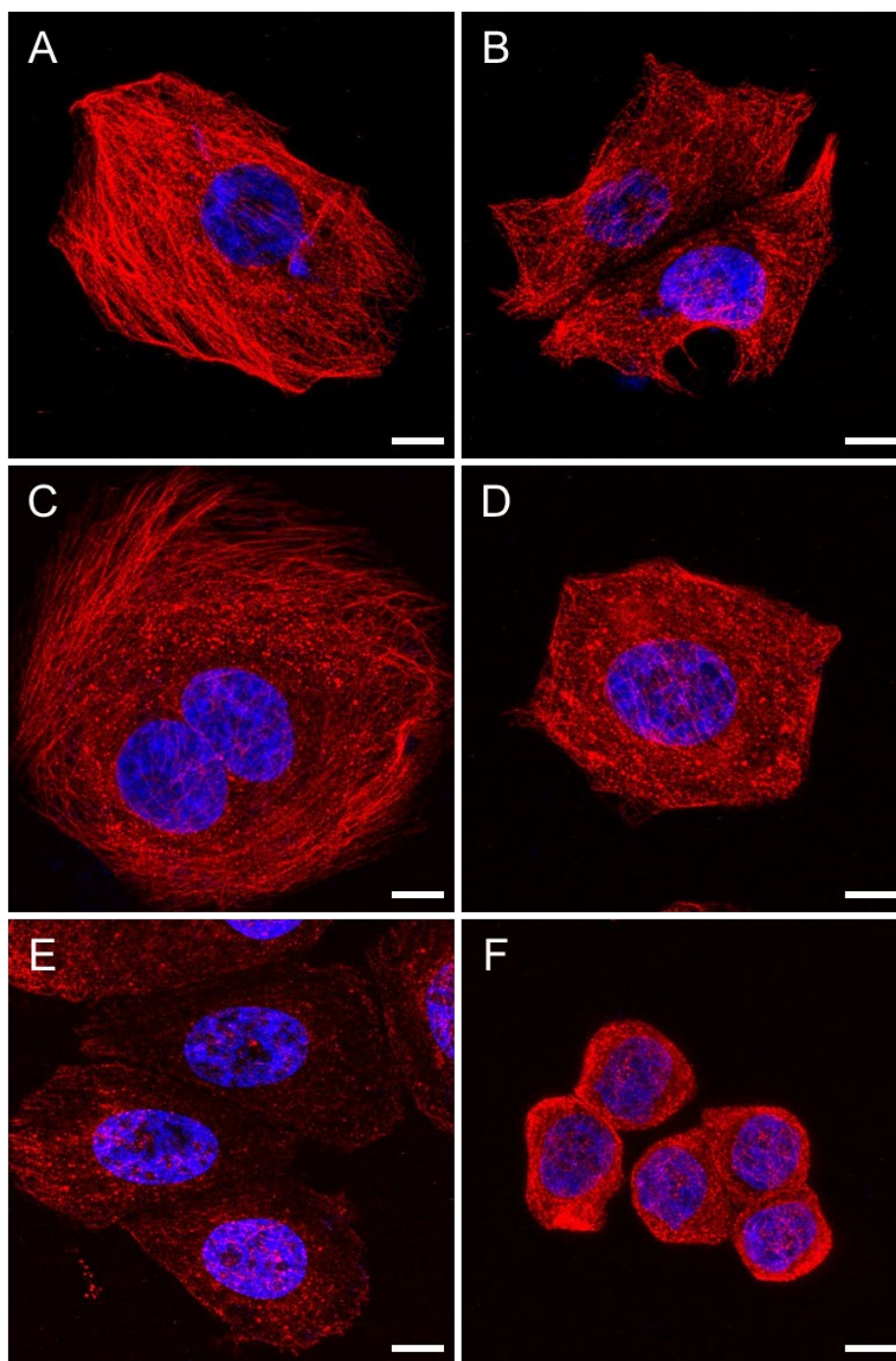


Figure 2.6. Confocal-microscopic images of SKBR-3 cells those were incubated with 1 mg/ml of different functional peptide modified UCNPs for 4 hours. (A) no interference; (B) Peg-UCNPs; (C) Ctrl-UCNPs; (D) CTP-UCNPs; (E) TIP-UCNPs; (F) CTP/TIP-UCNPs. The α -tubulins were indicated by Alexa-Fluor 555 (Red). The nucleus was indicated by DAPI (Blue). The scale bars indicate 10 μ m.

2.4 Conclusion and Discussion

In this study, we selected a 15-residues peptide sequence VQIINKKLDLSNVVQS (TIP) from Tau protein, which has never been approved or applied to interrupt microtubule assembly individually. We have synthesized the multi-functional nanoparticles CTP/TIP-UCNPs with the cell-targeting peptide (CTP), TIP and cell penetrating peptide R8, which trend to be uptake by breast cancer cells, interfere the regular microtubule function and then kill the cancer cells. Since the core of the complex, UCNPs are not only a stage of the peptides but also a fluorophore, CTP/TIP-UCNPs can be used to image the cancer cells too. However, some questions remain to be studied in the future. For instance, the TIP appeared to promote the tubulin polymerization in microtubule assembly assay in a way similar to paclitaxel. Instead, the TIP delivered into the cells inhibited the tubulin polymerization similar as nocodazole according to the confocal-microscopic images. It is possible that the TIP interacts the extracellular and intracellular tubulin protein in different ways. The complicated cell plasma environment might limit the aggregation between the nanoparticles and proteins or accelerate the microtubule degradation when it binds to the particles. A systematic *in vivo* study needs to be designed and accomplished to verify the anti-tumor potential of our complex particles for preclinical application in the future.

Chapter 3: Guiding nanomaterials to tumors for breast cancer precision medicine: From tumor-targeting small molecule discovery to targeted nano-drug delivery to breast tumors

3.1 Introduction

In the recent decade, targeted drug delivery has been studied intensively in cancer treatment.¹⁰¹⁻¹⁰⁴ It involves the use of tumor-recognizing molecules in the drug formulation to enhance drug accumulation in the cancerous tissue. This strategy can result in significantly enhanced cancer treatment efficacy, decreased side effects as well as reduced drug use. Up to date, different types of molecules with tumor affinity, such as antibodies,¹⁰⁵⁻¹⁰⁹ folic acid/folate,¹¹⁰⁻¹¹⁵ and hyaluronic acid,¹¹⁶⁻¹¹⁹ have been reported and employed for targeted drug delivery. These molecules interact preferentially with certain types of proteins that are overexpressed or specifically expressed at the tumor sites. Namely, in this type of tumor-targeting approach, it requires unambiguous pre-knowledge of the corresponding tumor receptors that are paired with these targeting molecules.¹²⁰⁻¹²³ However, such strategy neglects the patient-specific tumor difference for the same type of cancer. Ideally, a molecule targeting patient-specific tumors should be identified and then integrated with the cancer therapeutics to achieve customized cancer therapy. This is the goal of precision medicine in the context of cancer therapy. Precision medicine is a new emerging research area that aims to provide personalized drug formulations or treatment plans for individual patients.¹²⁴⁻¹²⁵ It is expected that by using the patient-specific solution, cancer treatment can be significantly more effective. Since each type of cancer differs in many ways on different patients, especially on the molecular level, the tumor receptor-based targeted delivery strategy may not work quite well for precision medicine, as the

expression level of receptors may vary dramatically among different patients. This is also one of the reasons why the current cancer therapeutics result in low survival rate. In addition, for unknown types of tumor or new tumor variants on individual patients, it is practically difficult to explore the specific ligand-receptor pairs for them when the patient-specific receptors have not been identified. Here I show that without considering the unique receptors of breast tumors, I discovered novel peptides capable of preferentially recognizing the tumors by phage display technique. This is possible because in principle identification of targeting peptides by phage display does not require us to have prior knowledge of the target, and thus peptides affinitive to unknown types of tumor can be selected in a fast and cost-effective manner, allowing us to seek patient-specific tumor-homing peptides. I intend to demonstrate a new strategy of breast cancer precision medicine using MCF-7 breast cancer bearing mice as the model, where a tumor-homing peptide customized to a specific patient is first identified without the need of knowing what receptors this peptide is recognizing and then linked with a cancer nanomedicine (using photothermal gold nanorods, AuNRs, as a model drug) to selectively inhibit tumor (Figure 3.1). For the first time, I demonstrate such strategy by carrying out the whole procedure from the discovery of tumor-homing peptides to the eventual validation of the peptide in targeted breast cancer therapy using the same animal model in the same lab.

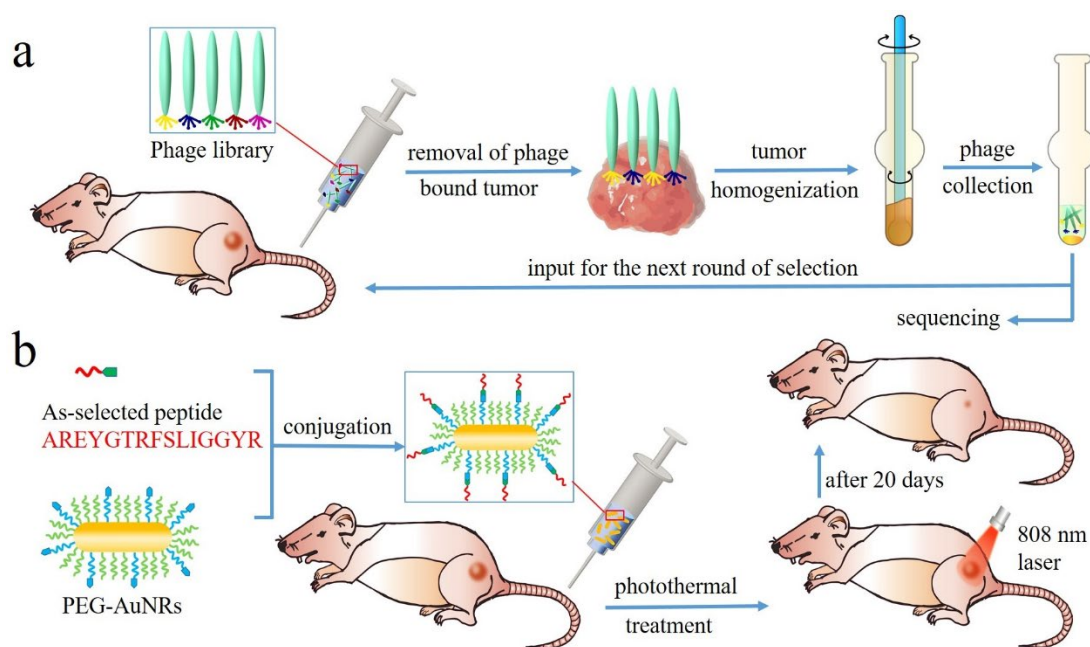


Figure 3.1. Schematic description of the phage display-based breast cancer precision medicine.

a) Selection of the patient-specific breast cancer-targeting peptides through *in vivo* phage display. A phage library was first injected through tail vein into the tumor-bearing mice and allowed to circulate for 24 h. Afterwards, tumors with preferentially bound phages were removed from mice and homogenized. Phages were then collected by centrifugation, amplified and used as input for the next round of *in vivo* selection. b) Coupling of the as-selected peptide with anticancer nanomedicines (AuNRs) to enhance their accumulation inside tumors so as to achieve highly efficient cancer treatment by photothermal therapy.

3.2 Materials and Experiments

3.2.1 Cell line and MCF-7 tumor xenograft

Human breast cancer cells MCF-7 (ATCC Org.) were cultured in Eagle's Minimal Essential Medium (EMEM, ATCC Org.) with 10% fetal bovine serum (Gibco Inc). To generate tumors on the mice, $2.5\text{--}3 \times 10^6$ cells in 0.1 ml of saline were hypodermically injected on the

right flank for each mouse (Athymic Nude-Foxn1^{nu}, 3-5 weeks, female, Harlan Lab). All the tests in the *in vivo* phage display and photothermal therapy were started when the tumor reached 0.5-0.8 cm in diameter.

3.2.2 *In vivo* phage display

The f3-15mer phage library (aka fUSE/15mer; GenBank Accession AF246445) displaying 15-mer peptide on all five copies of pIII coat proteins at N-terminal on fd phages were provided as a gift from Dr. George Smith at the University of Missouri. At least 1×10^{12} transducing units (TU) of f3-15mer phage library were intravenously injected into each tumor-bearing mouse through the tail vein and allowed to circulate for 1 hour before the euthanasia by CO₂ asphyxiation. Then 20 ml of PBS was used to wash the unassociated phages by heart perfusion. The tumor-recognized phages were purified from the tumor homogenate and then amplified to be used as new input phages for the next round of selection. The tumor-homing peptide sequences in every round of selection were identified by phage genome sequencing from the third to fifth round.

3.2.3 *In vivo* fluorescence imaging

All the peptides with biotin labeled at C-terminal for conjugation with streptavidin were commercially purchased from United BioSystems. A linker of GGG was added to the C-terminal during the peptide synthesis for each peptide. The streptavidin proteins tagged with a fluorescence dye (Cy5) at a dye/protein ratio of 6.5 were purchased from USBiological. To conduct conjugation, 16 μ l of 1 mg/ml streptavidin was added to 800 μ l of 6.0 μ M peptide saline solution, and the mixture was then incubated at room temperature for 3 h. Free unconjugated peptide was then removed by using Slide-A-Lyzer Dialysis Cassettes (10,000 MWCO, Thermo Inc.) according to the protocols provided with the kit. The Cy5-peptide conjugates were stored at

4 °C and used within 24 h after preparation. For *in vivo* imaging, 5 nmol of the as-prepared Cy5-peptides conjugates dissolved in 100 µl saline was injected through tail vein of each tumor model. All of the mice were given anesthesia of 4% isoflurane /oxygen mixture and scanned under the *In vivo* Xtreme Imaging System (CarestreamInc.) 24 h after the injection.

3.2.4 Synthesis of gold nanorods

Gold nanorods were synthesized through a seed mediated process. Seed solution was prepared by adding 600 µl of NaBH₄ (100 mM) into 10 ml mixture solution of 0.25 mM HAuCl₄ and 0.1 M CTAB under vigorous stirring. A total of 30 ml AuNRs solution was prepared each time. Briefly, to a 30 ml growth solution, which contained 0.5 mM HAuCl₄ and 0.1 M CTAB, varying amounts of 4 mM AgNO₃ solution and 210 µl of 78.8 mM ascorbic acid solution were added in sequence. After gentle shaking, 36 µl of the as-prepared gold seed solution was added, and the growth of AuNRs took place under room temperature for overnight. The resultant nanoparticles solution was considered as the as-synthesized AuNRs.

3.2.5 Preparation of peptide conjugated tumor-homing AuNRs

The peptides used for AuNRs conjugation were synthesized with four additional lysine amino acids (KKKK) at the C-terminal. It is expected that the majority of the conjugation reaction takes place through the amine groups at the C-terminal, leaving the –NH₂ at the N-end free. The AuNRs with extinction band maximized at around 808 nm were synthesized according to the well-developed seed-mediated method in cetyltrimethylammonium bromide (CTAB). Conjugation of peptides onto AuNRs can be finished through a three-step surface modification. To begin with, 100 ml of the as-prepared AuNRs were centrifuged twice at 10,000 rpm for 10 min, and then redispersed into 50 ml of 0.1 mM HS-PEG aqueous solution and placed overnight to allow the CTAB molecules on the AuNRs surface to be replaced by HS-PEG molecules. The

AuNRs were then centrifuged once and mixed with 50 ml of 0.1 mM HS-PEG-COOH for a few hours to achieve partial ligand exchange of HS-PEG by HS-PEG-COOH. Afterwards, the nanoparticles were subjected to another round of centrifugation and redispersed into 10 ml of pH 6.0 MES buffer. The peptide conjugation was then initiated by activation of –COOH with EDC (4 mg) and NHS (6 mg) at room temperature for 15 min, followed by centrifugation at 4 °C for 10 min. Thereafter, the nanoparticle pellet was immediately resuspended into 2 ml of 1 mM peptide/ saline solution and left on a rocker shaker for 2 h under room temperature. The resultant peptide-conjugated tumor-homing AuNRs were about 5 mg/ml in concentration and 200 µl of the solution containing about 1 mg of AuNRs were used for each mouse for intravenous injection.

3.2.6 Quantification of AuNRs tissue distribution through ICP-AES

Peptide 1 or control peptide conjugated AuNRs (200 µl, 5 mg/ml) were intravenously injected into each tumor-bearing mouse (5 mice/group) through the tail vein and circulated for 1 day to 5 days before euthanasia. The tumors and other organs including liver, kidney, heart and lung, were excised after heart perfusion and completely dried in a freeze-drying system. Some peripheral blood was collected before heart perfusion as well. Afterwards, all these tissues were weighed and then digested completely by freshly prepared aqua regia. Finally, the solution was diluted with large amount of water, filtered and used for Inductively coupled plasma atomic emission spectroscopy (ICP-AES) quantification.

To track the gold concentration in peripheral blood, 20 µl of blood was collected from suborbital space of 5 anesthesia mice each time at 3 min, 20 min, 1 h, 4 h, 7 h, 12 h, 24 h and 48 h after injecting either peptide conjugated AuNRs or PEG modified AuNRs. The gold was then digested and quantified following the same procedures as above.

3.2.7 Photothermal treatment of MCF-7 tumor

20 tumor-bearing mice were randomly separated into four groups. Mice in each group were injected intravenously with target peptide-AuNRs, control peptide-AuNRs, PEG-AuNRs and saline respectively. The amount of AuNRs was 1 mg per mouse. Twenty-four hours after injection and under general anesthesia, all the mice were irradiated at the tumor site by 808 nm laser for 5 min at a power density of 2.25 W/cm². The laser spot size is about 1 cm in diameter. After laser irradiation, the mice were housed for another 20 days, after which the tumors were measured in dimensions and were then taken out of the mice and weighed. The tumor volume was calculated by the following equation: Volume= length \times width²/2.

3.2.8 haematoxylin and eosin (HE) staining

For HE staining, tumors were excised from mice 3 h after laser treatment and then placed immediately into 10% fresh formalin solution and soaked for 24 h. The fixed tumors were embedded in paraffin block following standard procedures. Thereafter, they were cut into 5 μ m thick sections and mounted onto glass slides. Before imaging, the slices were deparaffinated and stained subsequently with hematoxylin and eosin staining solutions. The imaging was carried out on Eclipse Ti microscope system (Nikon Instruments Inc.).

3.3 Results

3.3.1 Biopanning against *in vivo* MCF-7 tumors

Briefly, *in vivo* phage display was carried out by several rounds of affinity test against MCF-7 tumors *in vivo*. In the first round, a phage library, which contains billions of phage clones with each displaying a unique 15-mer peptide at the five copies of minor coat protein (pIII) of the phage, was injected intravenously into tumor-bearing mice. After an hour, the mice were sacrificed and the tumors were excised and homogenized. Tumor-associated phages (output

phages) were extracted from tumor homogenate and used as an input for the next round of selection. Similarly, in the rest rounds of selections, output from the previous round was employed as an input for the next round and injected intravenously into a new tumor-bearing mouse. In this work, a total of 5 rounds of selection were conducted. It is expected that phages appear in the output of subsequent rounds should have higher tumor affinity. Hence, I randomly isolated some output phage clones in round 3, 4 and 5. Since the DNA inside the phage genetically encodes the peptides displayed on the surface of the phage, the DNA of the tumor-associated phage clones was sequenced to identify the sequences of 15-mer peptides (Tables 3.1, 3.2, 3.3 and 3.4). A total of 246 colonies were identified from 3-5 rounds of *in vivo* selection and the top 12 identified peptides with the number of repeats no less than 2 after the 5th round are listed in Table 1. Our following studies were mainly focused on the top 5 peptides with the highest occurrence frequency, namely AREYGTRFSLIGGYR (peptide 1), PKAFQYGGRAVGGLW (peptide 2), PVRYGFSGPRLAELW (peptide 3), RNVPPIFKEVYWIAQ (peptide 4) and RTLIRMGTGAHAFAV (peptide 5), as they are more likely to have higher affinity to MCF-7 tumors than the rest of the peptides. Among these peptides, peptide 1 has the highest occurrence frequency, indicating that peptide 1 has the highest tumor affinity.

Sequence	Count (30 seq. total)	Sequence	Count (30 seq. total)
AREYGTRFSLIGGYR	1	PSVPVFRGRFFQVDY	1
AVVSSGGALYXRIVR	1	PVIAIPPSFANMFLF	1
FAFSPCPLESNVIGC	1	PWSSRPWYLQFLGAA	1
FSLGVSSVIFSPVSA	1	RLVCWRLGCVSPMGS	1
FVFPRPNAY*	1	RPPVVDAAHFGASRW	1
GHSPRCSSSFVRCEA	1	RQQDGRLIYTTASVR	1
GQDVIRIRNEVNQYGL	1	SEELLVESSAIRSRE	1

GVQVPFSGGSSLLGM	1	SNPGLFVSGYWRLFP	1
GVSEDASVQHYYRSP	1	TRLECFSAGWRLSAC	1
LRMGLCSDQIRLSA	1	TRVYWAPVSEGDVSP	1
MFRTFVGRSSNAVVG	1	VSSQHGXGREVNSAV	1
MQSVSGWFPWESVAY	1	VYASPASIPWSFAGL	1
NAVRVAFWSVPLYPF	1	YFTTPATLLPFGVGT	1
NAVRVAFWSVPLYXF	1	YRVREPQLFCCEGPD	1
PGGGANFLLSPFSGG	1	PSVPVFRGRFFQVDY	1

Table 3.1. 30 sequences were randomly picked and identified from the 3rd round of *in vivo* biopanning.

Sequence	Count (54 seq. total)	Sequence	Count (54 seq. total)
ACAIGCXQANGLALV	1	PFPVSSRVVPRFTAV	1
AGGGGPTVGDDRVR	1	PIGVFWDDLLIRH	1
ALGRGRVVGVRVLSL	1	PKAFQYGGRAVGGLW	3
AREYGTRFSLIGGYR	3	PKAXQYGGRAVGGLW	1
AVYPLLVICLLGRFW	1	PVQSLYAIGGVSLDT	1
DGLRVGXWDAVSX	1	PWSSILVGRSSSLLS	1
DKCVRXRILFMLVLM	1	QDFFAFCGGLAAVCG	1
DVLYRFGHSSVVFPG	1	RCSSFAMCGSIVPGS	1
FPYTRVPHFGNVHSS	1	RFPSASWSFSGHAAT	1
GASILGGXXGXXP*	1	RGAPFFISVSERAFR	1
GLAPVGSHSATPRPW	1	RSSGAVXNGVGVSA LG	1
GLDLLHTTWRCAPP	1	SGTGLXYPSTAGSS	1
GPVVLWPPLFDGHL	1	SGVHSYLAXRPVRL	1
GRXRLGVVSVLSXDG	1	SIGEMPSGLVTLST	1
GTLKVGMMCSLGACLG	1	SNPGLFVSGYWRLFP	1
HRWMPHVFAVRQGAS	1	SRHVRSLGNLGDVSVG	1
KTWXPXLVPGSASGRA	1	TSASTSVFIXRASST	1
LDPRRASFHIGRAAP	1	TTCLDFFNRPEVFWG	1
LFTPFFSCHEFCWD	1	TYHSVVWSEPVVWS	1
LGRAGQSYPSFARGL	1	VRCEGVLINGDRCGL	1
LGRARDRLSIQFPHF	1	VSSQHGXGREVNSAV	1
LRFISVAVAGNLSWA	1	WSNRMPPLFTXWYX	1
LRPPVAGMSVARVYG	1	YFTTPATLLPFGV*	1
LVRALPLWPLVGPV	1	PFPVSSRVVPRFTAV	1
MCAVRDPAFSRS*	1	PIGVFWDDLLIRH	1
MPLRFFXPSXGPLAP	1	PKAFQYGGRAVGGLW	3
PFARAPVEHHDVVGL	1	PKAXQYGGRAVGGLW	1

Table 3.2. 54 sequences were randomly picked and identified from the 4th round of *in vivo* biopanning.

Sequence	Count (162 seq. total)	Sequence	Count (162 seq. total)
AHPPLASVWHVSVPL	1	PKAFQYGGRAVGGLW	7
ALESSGSVPSRDLPP	1	PLRYGPSRSRLDEVW	1
AREYGTRFSLIGGYR	7	PMLGPHLCVSEFCGR	1
ARIGFASGSRPYVSS	1	PNRNYLPNTSMDGSR	1
ASSFSVSEVSVRRV	1	PPDSFSRGYRVRDTF	1
ASSVPYVDANWSYNR	1	PPQTISGKARYLPSV	1
AVFDGSLCVPGFYSC	1	PRAASIFRAGHVSML	1
AVTPQNPYGIQRDRR	1	PSALRVKGFTVVSR	1
AYGLVVPDLPAMPSL	1	PVRYGFGSPRLAELW	3
CAGFQSRQVAL*	1	QADGPNSVVRPFTLT	2
CSGCAPGFRSERAIR	1	QPVSAPVPLCRLHCRS	1
DRYLPINGVSMFGVP	2	QPWHPGVYGVASSVA	1
DSALRVSRWRLSHSV	1	RAPRSAPGIFVFRSF	1
DSSSLGNSSGSRGWR	1	RERIHSPGSTQILFL	1
EGLFSFPRGASE*	1	RFGFSATWDQSNLLL	1
FAFSPCPLESNVIGC	1	RGFLSDLHALASRDR	1
FGHIIPSRFDRLSLG	1	RNVPPIFKEVYWIAQ	3
FGRIPSPLAYTYSFR	1	RRVP*	1
FLLTGLQHATSSGFR	1	RSDHLGVGPASASRYG	1
FSDSFVTGVWAPSRP	1	RSFAYAAPTSFPWV	2
FSSGGTSYRLRHIPF	1	RSLSHGGRWGPGYAI	1
FSVSFPSLPAPPDRS	1	RSPWSDFYASASRGP	1
FVFPRPNAY*	1	RTLIRMGTGAHAFAV	3
FVRHYLLGGQGSLPR	1	RVLFLVAALAIGSLA	1
GAKPGLGPRAHLGGV	1	RVLGRDGSVIFYELAA	1
GALHQTRVPVGAFAW	1	RVNFLFKPSVIFNAP	1
GAPGAFFGSVRDVVPRR	1	RVPPRYHAKISPMVK	1
GAPLSANFNNAFWR	1	RVQSTILSGLRGFSS	1
GAVDFVSLYAAATVA	1	RVTHHAFLGAHRTVG	1
GAYPSLDFPRAPSFG	1	RYPVPFPGFEETLPR	1
GDAFGFFPPFRTMG	1	SDHSPTQSQRASHDA	1
GFTDVHLHLPGNSHR	1	SDWFPTACFDCRSVR	1
GGAVFPEYPLARAFL	1	SGASRNSAFWAVSVA	1
GGPLVSPLSEDARPW	1	SGAYSSFRPSHHTTR	1
GKGEVSLYSLGSPGM	1	SGLCRYESPSGRPSC	1
GLHGATPAHRLFHTG	1	SGNSAIWPRVRL LHG	1
GSGAVSPPLWAARGR	1	SGYMTSALIRPSRFP	1

GSGTAYMMRPSLGPD	1	SKKPQSSNEGYRIAD	1
GTRAVLVVGLDALSA	1	SKTFQYGGRAIEGPW	1
GVGHVRAGHLRSVGI	1	SLPHLAPFGTTFFGP	1
GWSHFYRSPNFLRIQ	1	SPPLAPYGGTRVGLT	1
HAALSLPWYRINSVY	1	SPPLAPYGGTRVGLTG	1
HGSLGLGWPGHTSVR	1	SSGFRDAFRGWDGSA	1
HKAIQHGGRAVGGAW	1	SSVA*	1
HPTTSYSTSVFSWGW	1	STFFGFVGNSIVRPW	1
HVSGYVSRFDRSVGA	1	STSGVLSSILHVVS	1
HVTCVHSVSSLRSIV	1	SVGCPVVGTVGYLRG	2
IPLLVLNPLHLPRAL	1	SVLHPALDFTSLA	1
IPVQFSTIDFVAASY	2	SVVXLRTTRHFSTDSA	1
KVGVALVGP*	1	TGSVLSRFASGRLAP	1
LAGVQMSLRSLDTRR	1	TGTVVQVADPFAGGH	1
LFLNSHDDDRSFLSS	1	TNVPPISENDA*	1
LGAAHVVLGSSDFFP	1	TPFVFRAGRFFLHAG	1
LGGAGPFFGLGLVES	1	TRLECFSAGWRLSAC	1
LLGELPPTPRSPRLW	1	VCSPVFSPFCKMSVA	1
LPSIGPWEPXPDAL	1	VFGATSVVRDLYSR	1
LRPPVAGMSVARVYG	1	VRVRVDTAVYKPSYP	1
LRSLVSYSGGHNYSG	1	VGAASFYLERGSRXS	1
LTLSPHPWVLNHFVS	1	VLSRRLVVGGAAGV	1
LVGTLLGAHGFVAIP	1	VRINNCIGFDSNCTS	1
LVSRLTPCDLSFYAC	1	VRMFDYGVPRRAVYG	2
MAAWLPHSYSITRLL	1	VRVTPSFREPSGFV	1
MHFGPGFGH*	5	VTATAAQPGDAFIGV	1
NAAGYNSRVVTLPLF	1	WFPTHFWTYSSWTG	1
PAQSNFVTWGYNVAV	1	WRYRLVYALLAMLT	1
PFARAPVEHHDVVGL	1	YSRVLSSSYRFFDR	1
PGHSLGKLSVLHSFF	2		

Table 3.3. 162 sequences were randomly picked and identified from the 5th round of *in vivo* biopanning. The * marker indicates the incomplete peptides displayed on particular phages, which might be the result of either the failure of sequencing or the insertion of a stop codon into the fusion DNA sequence.

Peptide sequences	Count / Frequency (%)			
	3rd Rnd (30 cln)	4th Rnd (54 cln)	5th Rnd (162 cln)	Sum (246 cln)
AREYGTRFSLIGGYR	1 / 3.33	3 / 5.56	7 / 4.32	11 / 4.30
PKAFQYGGRAVGGLW	0	3 / 5.56	7 / 4.32	10 / 4.07
PVRYGFSGPRLAELW	0	0	3 / 1.85	3 / 1.22
RNVPPIFKEVYWIAQ	0	0	3 / 1.85	3 / 1.22
RTLIRMGTGAHAFAV	0	0	3 / 1.85	3 / 1.22
DRYLPINGVSMFGVP	0	0	2 / 1.23	2 / 0.81
IPVQFSTIDFVAASY	0	0	2 / 1.23	2 / 0.81
PGHSLGKLSVLHSFF	0	0	2 / 1.23	2 / 0.81
QADGPNSVVRPFTLT	0	0	2 / 1.23	2 / 0.81
RSFAYAAAPTSFPWV	0	0	2 / 1.23	2 / 0.81
SVGCPVVGTVGYLRG	0	0	2 / 1.23	2 / 0.81
VRMFDYGVPRRAVYGG	0	0	2 / 1.23	2 / 0.81

Table 3.4. Summary of peptide sequences and frequencies in the 3rd to 5th round of *in vivo* phage display against MCF-7 tumors *. * Only peptides having total colonies no less than 2 are included in this table. Rd = round of biopanning; cln = total phage colonies.

3.3.2 Live *in vivo* imaging of tumor-bearing mice

For *in vivo* imaging, the 5 peptides were conjugated to streptavidin with a Cy5 fluorescent tag and were injected into mice through tail vein. *In vivo* imaging was carried out 24 h later. For comparison, a random peptide, KGYGVGLRFPWQGA, was used as a control peptide. The amount of peptides accumulated at the MCF-7 tumors is judged by the fluorescence intensity, and the stronger fluorescence indicates more peptide accumulation. As shown in Figure 3.2, all of the 5 selected peptides have exhibited significantly higher tumor accumulation in comparison to the control peptide. Among them, peptide 1 showed the strongest fluorescence intensity, suggesting that it has the best tumor-homing capability. In addition, peptide 2 presented slightly

lower fluorescence intensity compared to peptide 1, which is consistent with the fact that peptide 1 has slightly higher occurrence frequency than peptide 2 (Table 3.4). Thus, peptide 1 is chosen for the following targeted drug delivery tests.

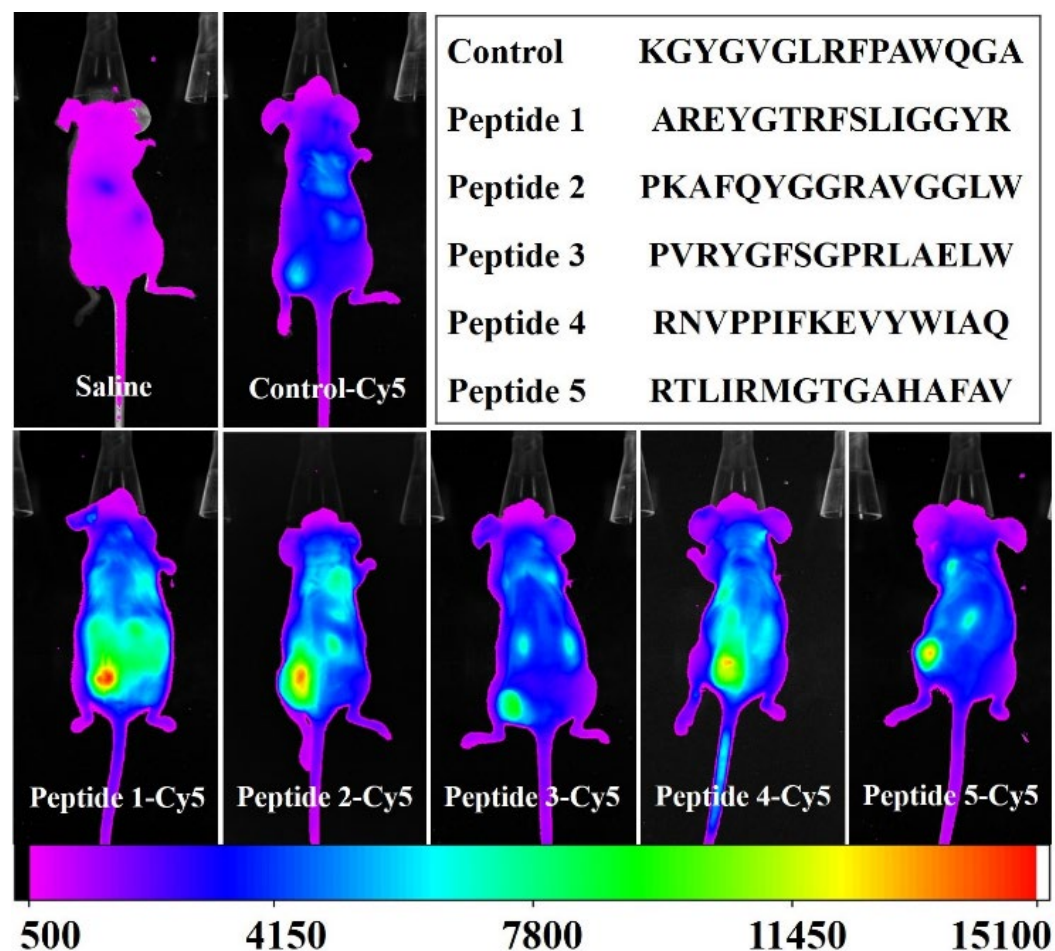


Figure 3.2. *In vivo* imaging for the detection of selective accumulation of tumor-homing peptides at the MCF-7 tumors. Peptides were first labelled with biotin at the C-terminal, and then conjugated to Cy-5 tagged streptavidin. Images were taken 24 h after the intravenous injection of 5 nmol of peptides (100 μ l in saline). All of the images were taken under the same parameters, thus the intensity difference represents the actual difference of peptide accumulation at the tumor sites.

3.4.3 Characteristics of peptide modified AuNRs

I then conducted *in vivo* experiments to test the excellence of the selected peptides in tumor targeting. First, I employed the *in vivo* imaging system to verify peptide accumulation at tumor sites. Second, I conjugated the peptides to gold nanorods (AuNRs, Figure 3.3), a well-known photothermal reagent,¹²⁶ to find out the effectiveness of the selected peptides in enhancing the targeted delivery of drugs to cancerous tissues.

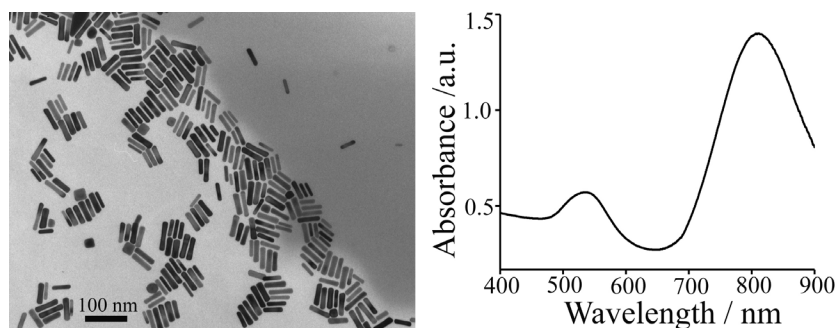


Figure 3.3. TEM image (left) and UV-Vis spectrum (Right) of the as-synthesized AuNRs used for the photothermal treatment.

The peptide-assisted *in vivo* drug delivery was tested by quantification of nanoparticles' tissue distribution as well as the effectiveness of photothermal treatment on MCF-7 tumor-bearing mice. To conduct the test, peptide 1 was first conjugated with AuNRs at the C-terminal through a well-developed method, in which the as-synthesized cetyl trimethylammonium bromide (CTAB) coated AuNRs were first replaced by HS-PEG-COOH, followed by peptide conjugation through the EDC/NHS chemistry (see experimental section).¹²⁷⁻¹²⁸ The resultant nanoparticles are termed Peptide-AuNRs. The hydrodynamic radius of the CTAB coated AuNRs, PEG coated AuNRs and peptide conjugated AuNRs is 40.8 ± 2.1 nm, 44.3 ± 2.5 nm and 47.0 ± 2.4 nm, respectively (Figure 3.4), suggesting the successful conjugation of peptides onto the AuNRs.

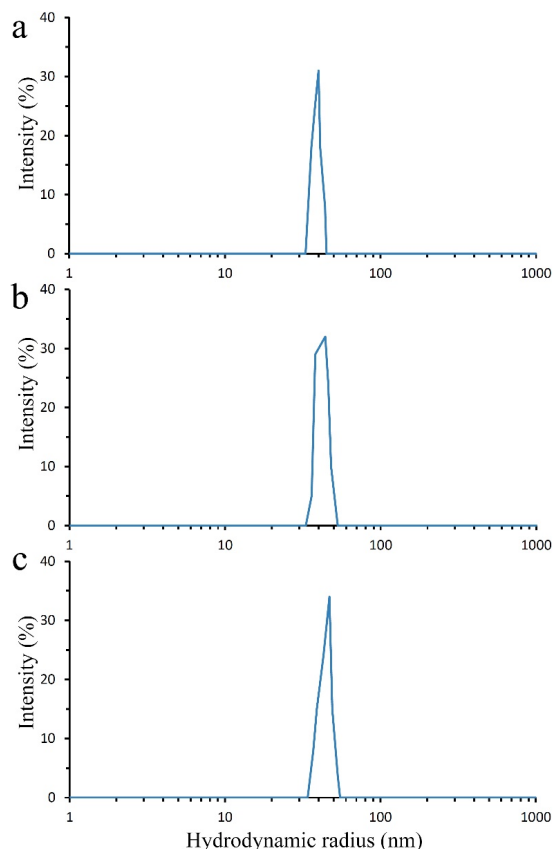


Figure 3.4. Dynamic Light Scattering (DLS) measurement of AuNRs with different surface ligands. The effective hydrodynamic radii are (a) 40.8 ± 2.1 nm for the as-synthesized CTAB-AuNRs, (b) 44.3 ± 2.5 nm for the PEG functionalized AuNRs, and (c) 47.0 ± 2.4 nm for the peptide functionalized AuNRs.

3.4.4 *In vivo* biodistribution of tumor-homing AuNRs

For quantitative studies, 1 mg of Peptide-AuNRs (200 μ l, 5 mg/ml) per mouse was used for intravenous injection. I first monitored for 48 h the *in vivo* blood circulation of AuNRs. I discovered that the half-life ($t_{1/2}$) of the Target-AuNRs in the blood is about 16 h (Figure 3.5), and the value for the control peptide conjugated AuNRs (Control-AuNRs) is about 18 h; both are comparable to the previously reported $t_{1/2}$ of PEG coated AuNRs.¹²⁹ For *in vivo* tissue distribution study, the nanoparticles were allowed to circulate for five different periods of time (1 day, 2 days, 3 days, 4 days and 5 days).

At the end of each time point, mice were sacrificed and the organs were then freeze dried, weighed, and digested. Finally, the concentration of gold in each organ was quantified by the Inductively Coupled Plasma Atomic Emission Spectroscopy (ICP-AES). The Control-AuNRs were used as a control. In the presence of the tumor-homing peptide, the tumor uptake of AuNRs after 1 day circulation is 63% higher than that of the case with control peptide and it remained to be 61%-83% higher during the whole period of five-day monitoring (Figure 3.6). This result confirms that peptide 1 selected from the *in vivo* phage display can result in significantly enhanced drug delivery to the MCF-7 tumors. The distribution of peptide-AuNRs in other healthy organs is either less than or comparable to that of the Control-AuNRs. It is worth noting that the gold content in liver in the target group is 56% lower than that in the control group on day 1, and remained to be 22-44% lower in the following 4 days, suggesting that modification of AuNRs with the tumor targeting peptides can effectively reduce the non-specific AuNRs uptake by livers.

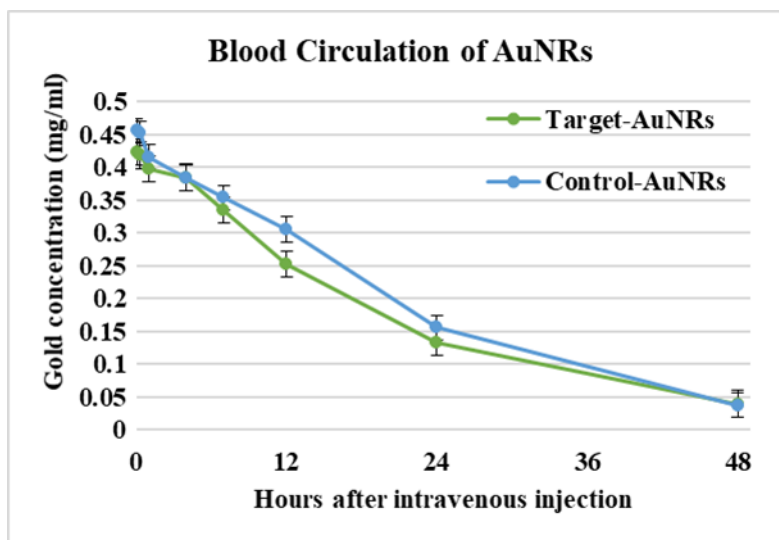


Figure 3.5. Blood circulation of AuNRs. 1.0 mg of tumor targeting peptide conjugated AuNRs (green) or control peptide conjugated AuNRs (blue) were injected intravenously. To track the gold concentration in peripheral blood (represented as the mass of gold per ml of blood), 20 μ l of

blood was collected from suborbital space of the mouse each time at 3 min, 20 min, 1 h , 4 h, 7 h, 12 h, 24 h and 48 h after injection, and immediately added into 200 μ l of freshly prepared aqua regia. The concentration of AuNRs was quantified by ICP-AES.

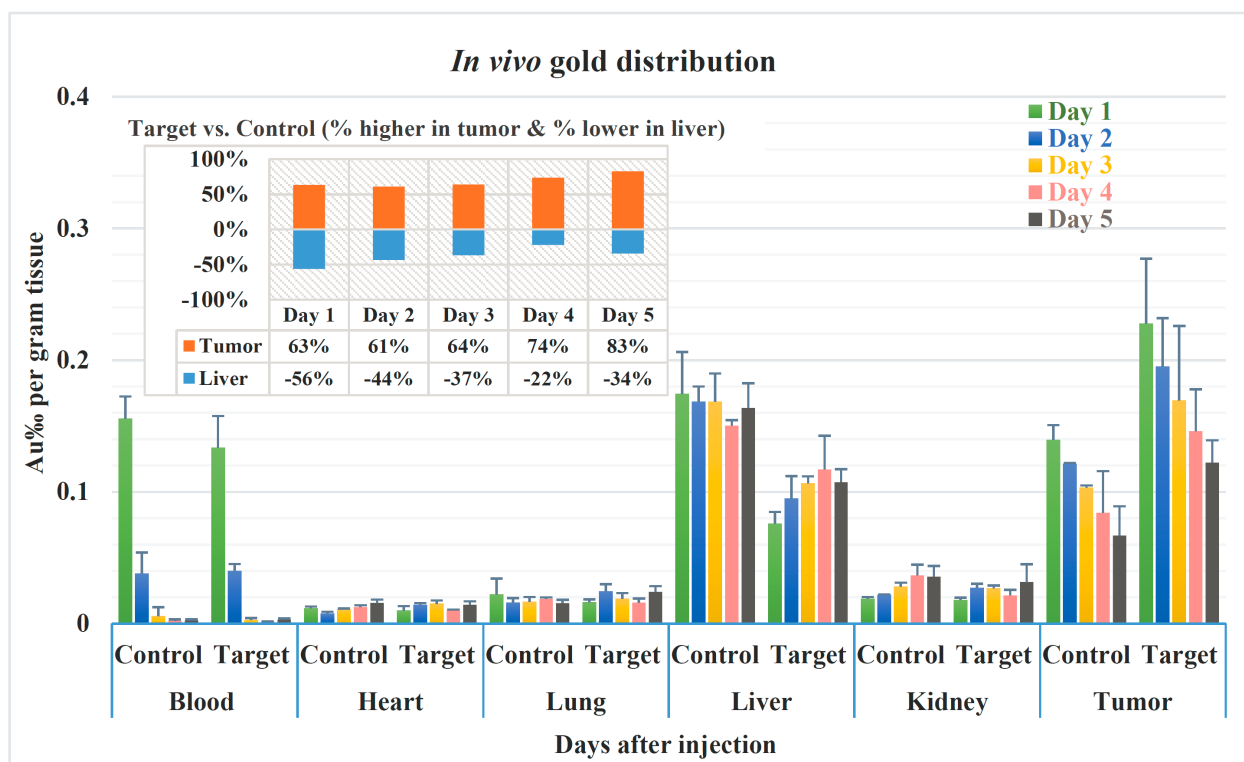


Figure 3.6. Organ distribution of AuNRs. Mice were sacrificed 1 day, 2 days, 3 days, 4 days and 5 days after the intravenous injection of 1 mg of AuNRs. Target group was the group injected with peptide 1 conjugated AuNRs whereas control group was the one injected with control peptide conjugated AuNRs. Gold concentration was calculated as mass permillage of Au in 1 gram of the corresponding tissue. The inset chart shows the percentage increase (in tumor, represented as positive values) or decrease (in liver, represented as negative values) of gold content in target group when compared to the control group on different days. The data indicate

that conjugation of our selected peptide 1 onto AuNRs can effectively increase their uptake by tumors but decrease their uptake by livers.

3.4.5 Tumor targeting photothermal treatment

The photothermal treatment was conducted 24 h after injection because the concentration of peptide-AuNRs in tumors is maximized at this time point according to the ICP-AES based biodistribution study. During the treatment, MCF-7 tumors were irradiated directly by a 808 nm laser at a power density of 2.25 W/cm² for 5 min. Figure 3.7 shows photographs of tumors and the corresponding average tumor volumes in each group 20 days after the photothermal therapy. One can see that the size and volume of the tumors in the targeting group (AuNRs functionalized with peptide 1) is significantly smaller than those in the other groups. In fact, two of the tumors in this group were destructed so severely that it was hard to collect any tumor tissue even after 20 days following the treatment. The development of tumors treated by non-targeting AuNRs, modified with PEG and control peptide, has also been retarded, although not as significant as that in the targeting group. This is because even without the assistance of targeting peptide, AuNRs can still be delivered to tumors through the passive targeting mechanism.

Hematoxylin and Eosin (HE) staining study further illustrates the death of tumor cells as a result of photothermal treatment (Figure 3.7c). Tumors used for this study were collected from mice 3 h after the laser treatment. For control tumors without AuNRs (Saline group), both apoptosis and necrosis, the two typical cell death mechanisms, are barely found in the tumor cells, suggesting that the laser power density used for the photothermal treatment was safe to normal tissues. For tumors in the target group (Target-AuNRs), however, the classic necrosis characters, including karyolysis, nuclear swelling and extensive pale eosinophilic cytoplasm are all observed, indicating contiguous cell necrosis upon acute injury caused by photothermal

treatment. In addition, the apoptosis characters such as nuclear pyknosis, hypereosinophilic cytoplasm and apoptotic bodies were also seen, which are indications of programmable cell death following the laser treatment. In contrast, such damages on the other two AuNRs groups (PEG-AuNRs and Control-AuNRs) were not as significant. Overall, our photothermal investigation is in accordance with the study of organ distribution of AuNRs by ICP-AES, namely, the *in vivo* selected targeting peptides, when conjugated onto AuNRs, can indeed result in enhanced delivery and accumulation of AuNRs at the tumor sites, which further leads to the remarkably improved efficiency in the photothermal cancer therapy.

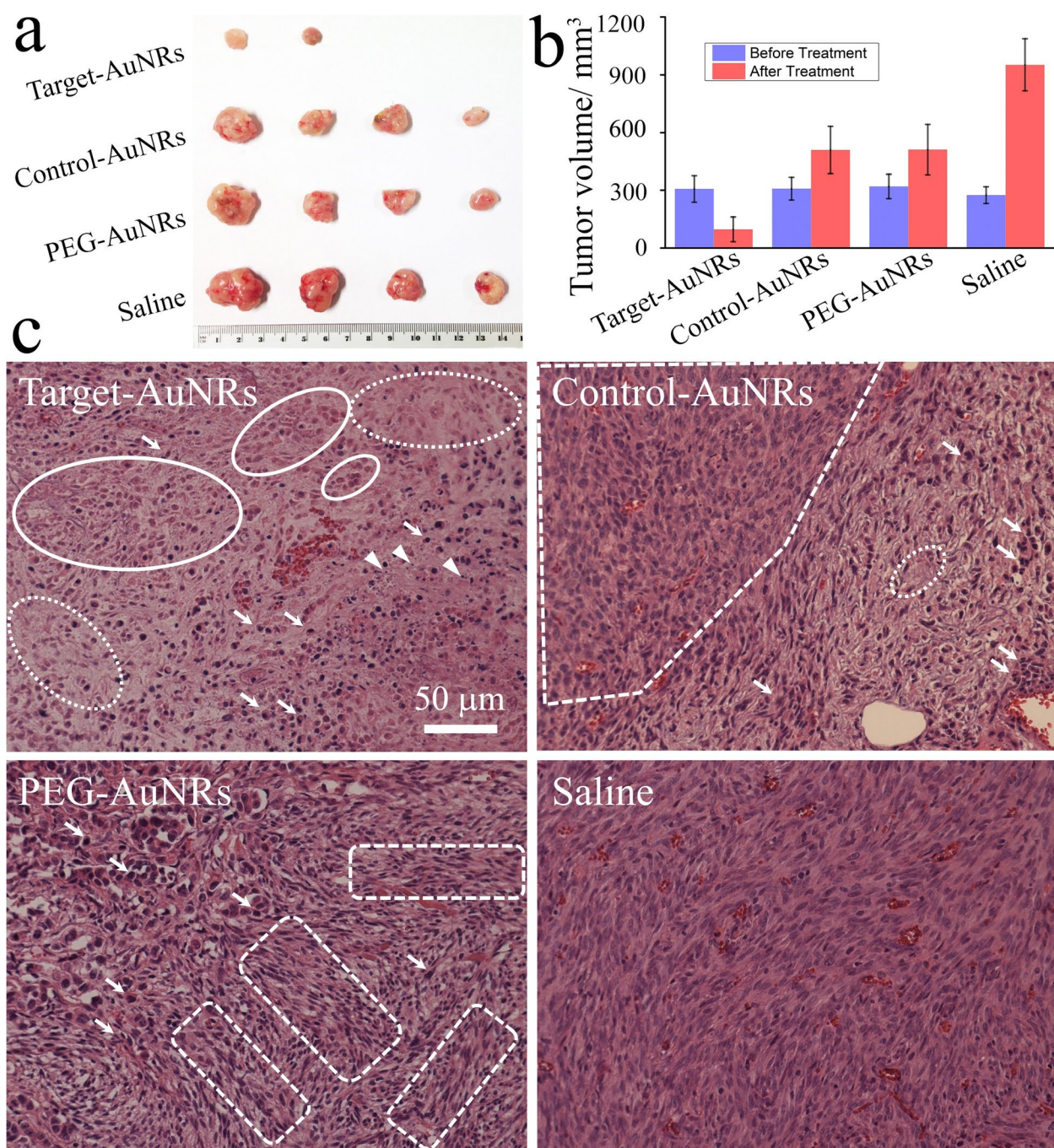


Figure 3.7. Photothermal treatment of MCF-7 tumors. (a) Photographs of tumors taken out from the mice 20 days after the photothermal therapy (For the target-AuNRs group, only two animals had visible tumors); (b) Average tumor volume before and 20 days after the treatment; (c) Images of HE stained sections of tumors obtained 3 h after 808 nm laser treatment. Target-

AuNRs: AuNRs modified with peptide 1; PEG-AuNRs: PEG modified AuNRs; Control-AuNRs: AuNRs modified with a control peptide; Saline: saline only and without AuNRs. Comparing to the normal nucleus of cancer cells in the control tumor, contiguous cell necrosis is determined by the extensive pale eosinophilic cytoplasm (typically highlighted by dashed ovals) as well as karyolysis and nuclear swelling (typically highlighted by solid ovals). The cells apoptosis with the presence of nuclear pyknosis, hyper-eosinophilic cytoplasm (typically highlighted by arrows) and apoptotic bodies (typically highlighted by arrow heads) are marked. The normal tumor tissue area in each AuNRs treated group is also circled by angled dash frames.

3.4 Conclusion and Discussion

Phage display can be carried out both *in vitro* and *in vivo*. Phage library is allowed to interact cancer cells in the culture media in the *in vitro* phage display whereas it is intravenously injected into animals and circulated in blood stream to enable the discovery of phages homing to tumors in the *in vivo* phage display. In principle, *in vivo* selection against tumors should be more target-specific and more effective for clinic applications, as the peptides were selected under conditions similar as the physiological environment. So far, none of the groups has studied the discovery of tumor-targeting peptides using *in vivo* phage display and then tested the use of such peptides in *in vivo* homing and destruction of tumors, all using the same animal models and in the same lab.¹³⁰⁻¹³² Most of the reported studies were based on peptides reported previously by others, rather than selected through exactly the same tumor model in the same work, thus these peptides cannot be considered as patient-specific. Hence, these works did not meet the requirement of precision medicine. In particular, for MCF-7 breast cancer, such study was reported exclusively based on peptides selected through *in vitro* phage display.¹³³⁻¹³⁶ In addition, although I only demonstrated the concept of phage display-based breast cancer precision

medicine by using photothermal treatment, the same procedures can be readily applied to other cancer therapeutics, such as chemo-, gene and photodynamic therapies.

In summary, I have demonstrated a new strategy of breast cancer precision medicine by using the MCF-7 breast cancer mice model. In this strategy, a patient specific tumor-targeting peptide was first identified through *in vivo* phage display. Our *in vivo* imaging study showed that these peptides can actively target MCF-7 tumors. By conjugating the as-selected peptides with the model drug, AuNRs, enhanced accumulation of the nanomedicine to the tumors was observed by the ICP-AES measurement, which further leads to improved cancer killing efficiency.

Chapter 4: 3D multiple cell spheroids in silica coated fungi network scaffolds

4.1 Introduction

According to the cancer fact sheet of World Health Organization in 2018, cancer was the second global leading cause of death and caused about 9.6 million deaths. A developed tumor model is desired for anti-cancer research. *In vitro* 3-dimensionally growing cancer cell spheroids can mimic the complex *in vivo* tumor microenvironment and retain an *in vivo* cancer cell phenotype with a similar solid structure like tumor tissues.⁵⁰⁻⁵³ Studies of multicellular cancer spheroids confirmed that the biological profile of 3D cultured cancer cells is closer to *in vivo* tumors comparing to 2D cultured cells, including cell proliferation and resistance to anti-cancer therapy.⁵⁴⁻⁵⁷ Thus, 3D cultured cell spheroids are the ideal model for studying the physiology of cancer and anti-cancer drug screening as a non-invasive alternate to animal tumor models. For generating 3D cultured cell spheroids, non-adherent surface cell culture dish⁵⁸⁻⁶⁰ such as bacterial culture dish, microwell non-adherent cell culture plate or microfluidic platform⁶¹⁻⁶³ is the most popular device to employ. To culture the cells in space limited gel matrix of collagen fibers^{57, 64-66}, the hanging drop technique⁶⁷⁻⁶⁸ or coculture the cancer cells⁶⁹ with endothelial cells is another common way to have the cells grown into multicellular spheroids. However, using either way to culture cell spheroids requires special devices consuming or advanced experimental skill. In addition, all those scaffold-free isolated cell spheroids or cell-seeded in hydrogel or microparticles are hard to identify, operate or transfer without a microscope. So that the 3D cultures cell spheroids have been rarely used for paraffin embedding histology and phage-antibody selection.¹³⁷

In this research, I first used the natural network structure of *Penicillium* fungi to build silica-based biocompatible branched scaffolds effortlessly. MCF-7 cancer cells will develop attached cell spheroids growing on the scaffold within 3 days, showing higher cell viability than those grow freely on non-adherent surface. The fibers of a scaffold are naturally connected as a single colony of fungi. Thus, the scaffolds could be easily transferred by clipping the edge of it without losing any fiber and the cells attached on it. Consequently, I first applied phage-antibody selection against *in vitro* tumors and paraffin embedding histology of cell spheroids. A total of four promising *in vitro* tumor binding peptides were identified by employing Ph.D.-12 phage peptide display library biopanning against MCF-7 cell spheroids on silica-coated fungi network scaffolds.

4.2 Material and method

4.2.1 Cell line and 3D cell spheroids generation

Human breast cancer cells MCF-7 (ATCC Org.) were cultured in Eagle's Minimum Essential Medium (EMEM, ATCC Org.) with 10% fetal bovine serum (Gibco Inc). To generate 3D cell spheroids, 2.5×10^3 to 2×10^4 cells in 2-5 μ l medium were seeded into a piece of dry scaffold and then cultured in 96 well plate. Transfer the cell loaded scaffold into a new well with fresh medium to discard the unattached cells at the second day after cell-loading. The same number of cells were seeded into ultra-low attachment 96 well plates without scaffolds as a control. The cell viability was evaluated by AlarmaBlue assay (BioRed Inc.). The morphology of cell spheroids was imaged on an Eclipse Ti microscope system (Nikon Instruments Inc.) for both light images and phase contract images.

4.2.2 Preparation of silica coated *Penicillium* fungi network scaffolds

The *Penicillium* colony were seeded into lysogeny broth (LB) broth and gently shaken at 100-120 RPM for 2-3 days at room temperature to form network spheres 5mm in diameter. The fungi spheres were fixed with 4% PFA for 12 hours and autoclaved in water to completely kill the fungi. The sterile fungi spheres were gradient dehydrate by 20%, 35%, 50 %, 65% and finally 80% (v/v) ethanol/water solution. To coat silica layer on the surface of the fungi mycelium, the fungi spheres were soaked in 75-85% (v/v) ethanol/water solution with 200 μ l TEOs and 300 μ l 38%-40% ammonia hydrate and gently shaken overnight. After 3 steps of 80% ethanol washing, the same step of silica-coating will be repeated for two more time to assure enough silica deposit for long-term cell culture. Then, the silica coated spheres were washed, gradient re-rehydrated and soaked with water, frozen rapidly in liquid nitrogen and finally dried in a freeze-drying system (). To avoid possible bacteria contamination, the scaffolds will be exposed under ultraviolet (UV) light for 45 min before cell seeding.

4.2.3 Light microscopy and phase contract microscopy

The cell spheroids were directly observed under the microscope (Nikon Instruments Inc.). An area of 1mm \times 1mm was imaged under the phase ring, the detailed area of 225 μ m \times 225 μ m inside the phage contract image was pictured by normal light microscope. For better observation of the cell spheroids growing on the scaffold, the whole sample will be removed from the 96 well plate and place in a well of 24 well plate before it was imaged by light microscope.

4.2.4 Cell viability assay of cell spheroid growing with or without scaffolds.

The AlamarBlue assay was applied for comparing and semi-quantificating the cell viability between the cell spheroids growing on the scaffolds to those growing without the scaffold. The assay was repeated for 4 times, at day 1, day 3, day 5 and day 7 respectively for 5

repeating wells of cells. In another word, the cell proliferation profile of a group of wells was monitored every two day for a week. Briefly, at each time point, 200 μ l of pre-mixed assay medium (20 μ l of AlamarBlue reagent added in 180 μ l of serum-free EMEM medium) were placed in each well of a new 96 well plate. The cell spheroids on one scaffold in one well was transferred into a well of pre-mixed assay medium and cultured at 37 °C for 3.5 to 4 hours and then transferred back to the 96 well plate filled with fresh medium and kept culturing in the cell incubator. For AlamarBlue assay on free cell spheroids, 180 μ l out of 200 μ l of the old medium was removed and replaced by 180 μ l of fresh serum-free medium and then 180 μ l of the medium was removed again. Thus, 99% of the old medium and serum was removed from the well, 20 μ l of serum-free medium remained in the well. 180 μ l of pre-mixed assay medium (20 μ l of AlamarBlue reagent added in 160 μ l of serum-free EMEM medium) was added into each well of free cell spheroids. The plate was incubated at 37 °C for the exact same time as the cell spheroids on the scaffold were. 150 μ l of the assay medium out of the total volume for both groups was transferred into a new 96 well plate and measured the absorption at 570 nm and 600 nm. The remain assay medium in the cell culture well was removed in the similar way above.

4.2.5 Scanning electron microscopy (SEM) and Energy-dispersive X-ray spectroscopy (EDS)

The cell spheroids were fixed with 4% PFA PBS buffer for 20 min, following by gradient dehydration using from 20% (v/v) to 100% ethanol/ water solution with concentration increment of 10%. Then the samples will be dried by critical point drying (CPD), attached on the specimen holder under the microscope to make sure the major area of cell spheroids growing is upward and sputtering coated with gold. The images and X-ray EDS were performed by NEON high resolution scanning electronic microscopy (Zeiss, Thornwood, NY). The component of gold was excluded from the weight calculation.

4.2.6 *In vitro* 3D multi-cell spheroids targeting peptide selection by phage library

biopanning

1×10^{12} transducing units (TU) of Ph.D.-12 phage display peptide library (E8110S BioLabs.Inc) were added into a 24 well plate with an empty scaffold and incubated for 1 h at 37°C to remove the scaffold and environment binding phages. The unbound phages were transferred into a new well with the cell spheroid loaded scaffold to interact with the cells for 1 h at 37°C. The scaffold was washed 10 times to remove the unbound phage. The spheroid-binding phages were then eluted from the scaffold. Additionally, cell penetrating phages were eluted by lysing the cell spheroids. The cell lysis releases the cell-penetrating phages. Both types of binding phages were amplified separately and used as the input phage for the next round of biopanning. After the third round of biopanning, the binding phage colonies were randomly picked and sequenced to identify the potential tumor-homing peptide.

4.3 Results

4.3.1 Structure of silica-coated Fungi scaffold.

The Penicillium mycelium sphere can grow over 3 cm long in diameter within 4-5 days in LB broth. To control the fungi to grow slowly is a key factor to have the fungi sphere grown with impact enough network of fibers. So that, instead of shaking the fungi at 220 RPM and 37°C, the fungi were cultured at room temperature and less than 150 RPM shaking speed. According to our experience, the fungus sphere with the size of 0.7-0.8 cm in diameter has the best fiber density and intensity of construction to provide network surface for cell attachment and suitable space for cell growth. Due to dehydration process for silica coating, the average diameter of silica-coated fungus spheres is 6.3 ± 0.3 mm that is 15% smaller than 7.4 ± 0.7 mm, which is the average diameter of the fungus spheres before silica coating (Figure 4.1A and 4.1B). The SEM

image showed the scaffold is composed by numbers of fibers with the average diameter of $1.5 \pm 0.4 \mu\text{m}$ (Figure 4.1C and 4.1D). The detailed SEM image of an open-end fiber indicated that the fibers of scaffold are hollow (Figure 4.1E). X-ray EDS result (Figure 4.2) confirmed the silica layer on the fiber surface with the silicon (Si) weight ratio of 10.6 %, the weight of gold caused by sputtering coating has been excluded. The peak of carbon (C) is excluded from the spectrum due to its dominating high counts. After incubating the empty scaffold in cell culture medium for 7 days, the silicon weight ratio decreased to 7.6%, which was still able to support the scaffold structure and the cell growth.

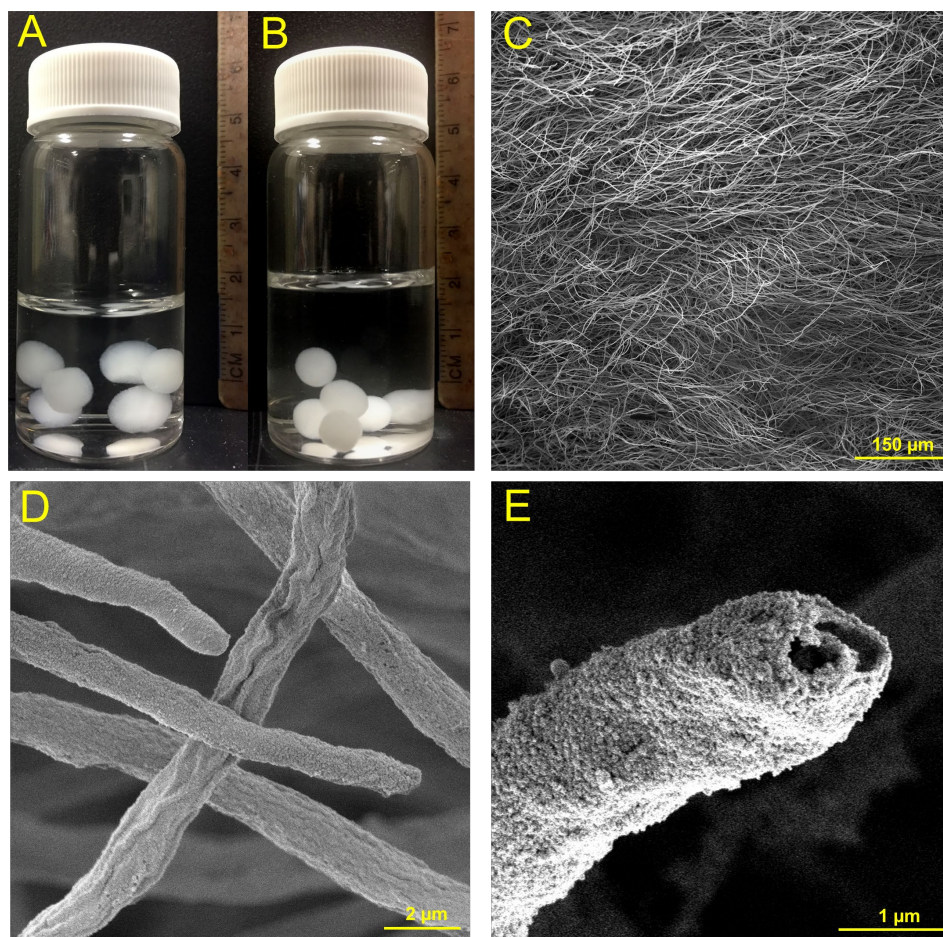


Figure 4.1. Fungus template branched silica scaffolds. (A) Fixed fungus spheres with average diameter of $7.4 \pm 0.7 \text{ mm}$ soak in sterile water. (B) Silica-coated fungus spheres with average

diameter of $6.3 \pm 0.3 \mu\text{m}$ soak in sterile water. (C and D) SEM images of the surface of the fungus template branched silica-coated scaffold. The average diameter of the silica coated fiber is $1.5 \pm 0.4 \mu\text{m}$. (E) detailed SEM image of an open-end fiber of silica-coated scaffold.

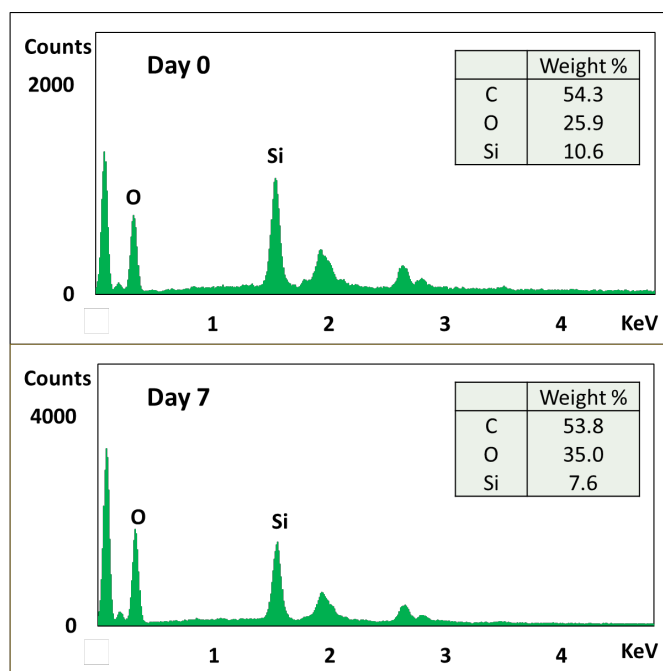


Figure 4.2. EDS spectrum of empty silica-coated scaffold at day 0 before incubation and at day 7 after incubation with EMEM. The peak of C is not included. The data table shows the weight distribution of C, O and Si.

4.3.2 Size shrinkage in pre-SEM process

The SEM images showed that the cells have formed spheroids with the diameter range of 35-135 μm at day 3 after cell-seeding (Figure 4.3). However, the shrinkage of mammal cells during the dehydration and drying process for SEM is unignorable without using osmium tetroxide, which is extremely toxic and high-risk to use.¹³⁸ The shrinkage range of the mean diameter of mammal cells and tissues is from 25% to 45% according to the related literature. In this study, I measured and compared the average size of both single cells and cell spheroids between LM and SEM images. The cell spheroids are significantly smaller in SEM image than

them in LM image with the shrinkage range from 34% to 48% (the average is $43 \pm 6\%$) according to Figure 4.4A and B showing SEM image and LM image of the identical area of cell spheroids (the same sample of cell spheroids at day 7 after 1×10^4 cells loaded in Figure 4.3). The single cell has the average diameter of $15 \pm 3 \mu\text{m}$ in phase contract microscope image (Figure 4.4D), which is 38% larger than the average diameter of $9 \pm 2 \mu\text{m}$ in SEM image (Figure 4.4C). Overall, the size shrinkage of single cell and cell spheroid in our pre-SEM process in our procedure mostly located in the range of 35%- 45%. Therefore, the calculated diameter range of the cell spheroids at day 3 is actually from 60 μm to 240 μm . The size of cell spheroid on the scaffold acquired from SEM image in the following discussion, including the diameter and volume, were recalculated.

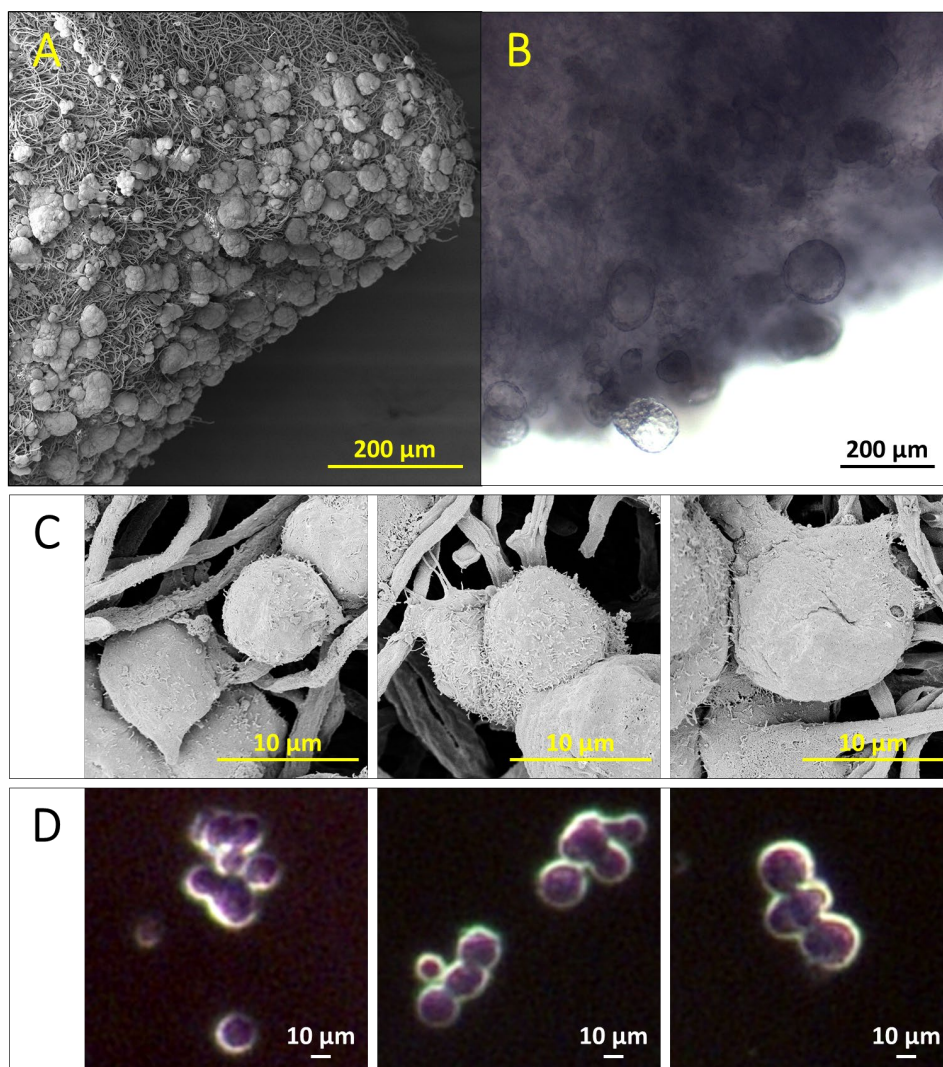


Figure 4.3. (A and B) SEM and LM images of the same sample of cell spheroids growing on the scaffold. The LM image was pictured right before the pre-SEM process. (C and D) SEM and phase contract microscope images show single cells respectively.

4.3.3 Statistics of 3D cultured MCF-7 cell spheroids.

The cell spheroids growing circumstance in non-adherent well plate was monitored for 7 days post-cell-seeding (Figure 4.5). The cell spheroids growing circumstance on the scaffold at day 3 and day7 post-cell-seeding was showed in SEM images (Figure 4.4). Some cell spheroids started to form at 24 hours post-cell-seeding, most of them were smaller than 100 μm in diameter.

Either the size or the amount of cell spheroids increased as the time went or as the number of cell-seeding increased.

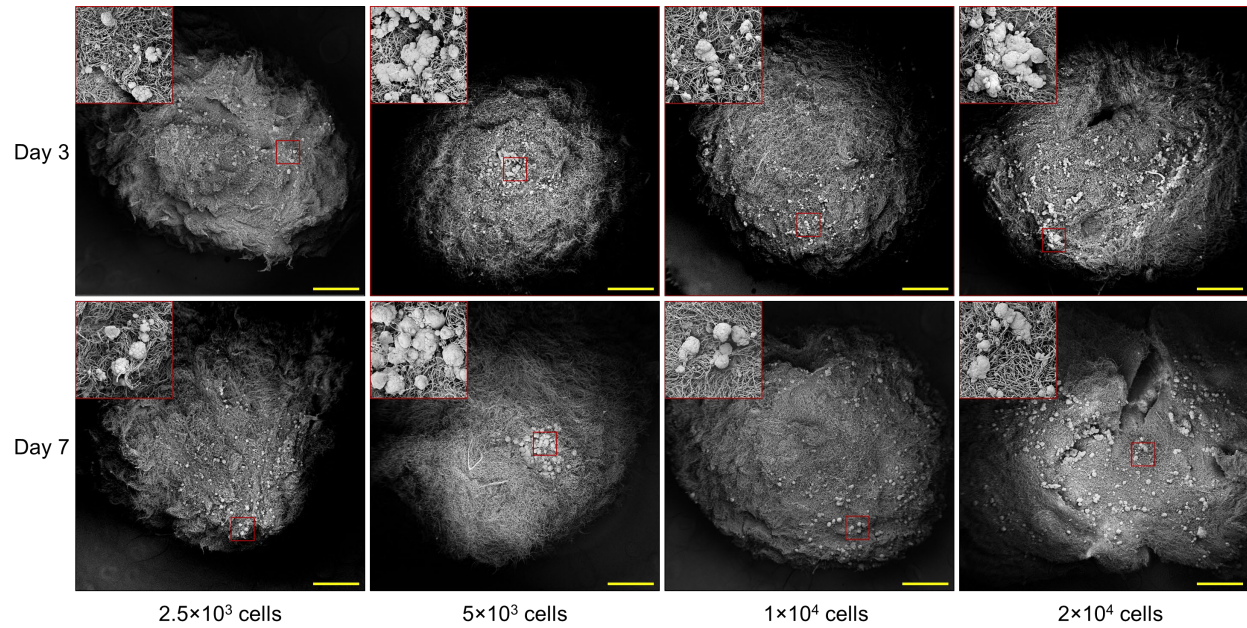


Figure 4.4. SEM images of MCF-7 cell spheroids growing on silica-coated fungi network scaffolds at day 3 and day 7 after loading cells of 2.5×10^3 , 5×10^3 , 1×10^4 and 2×10^4 on the scaffold respectively. The side containing most of the cell spheroids were displayed by adjusting the specimen stage. All the scale bars indicate $500 \mu\text{m}$. For each image, the inset image in red frame showed the detailed information of the area highlighted with red square. The red square area is $250 \mu\text{m} \times 250 \mu\text{m}$.

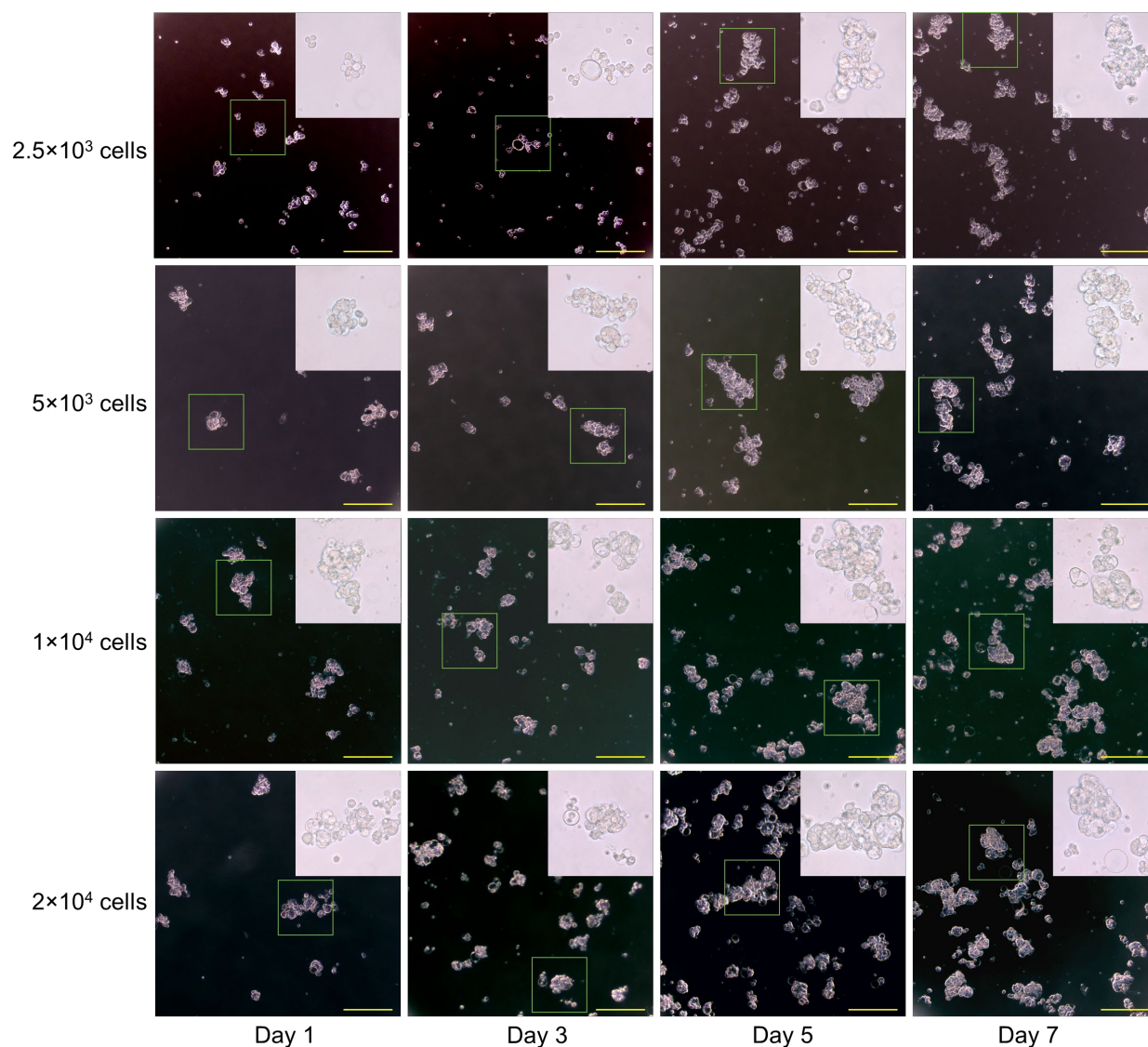


Figure 4.5. Phase contrast images of cell spheroids growing in Corning ultra-low attachment surface 96 well plate for 7 days. The bars indicate 200 μm . The inset image in each individual image is the zoom in view of area highlighted with green square. The green square area is 225 $\mu\text{m} \times 225 \mu\text{m}$.

To evaluate the efficiency of cell spheroids forming with the scaffolds, I compared the size distribution for 2×10^4 cells being cultured for 7 days, between them growing with the scaffold and them growing without the scaffolds. The SEM images of cell spheroids growing on the

scaffold (Figure 4.6) showed two types of growing manners. One was that the cells trended to form cell spheroids in larger scale, up to 500 μm in diameter. However, the amount of cell spheroids is low (Figure 4.6A to D). This manner was found in the scaffolds those were loaded with high concentrated cell solution (2×10^4 cells in 2-3 μl of medium). The other manner is that the cells trended to form hundreds of relatively equal sized spheroids (Figure 4.6E to H). For this manner, 2×10^4 cells were loaded within 5 μl of medium. According to the two manners, I supposed that the cells prefer to stay at the certain spot and interact with the surrounding cells once they had attached on the scaffold, rather than to migrate. The size distribution statistic between cell spheroids growing with and without scaffold showed the comparable result (Figure 4.7).

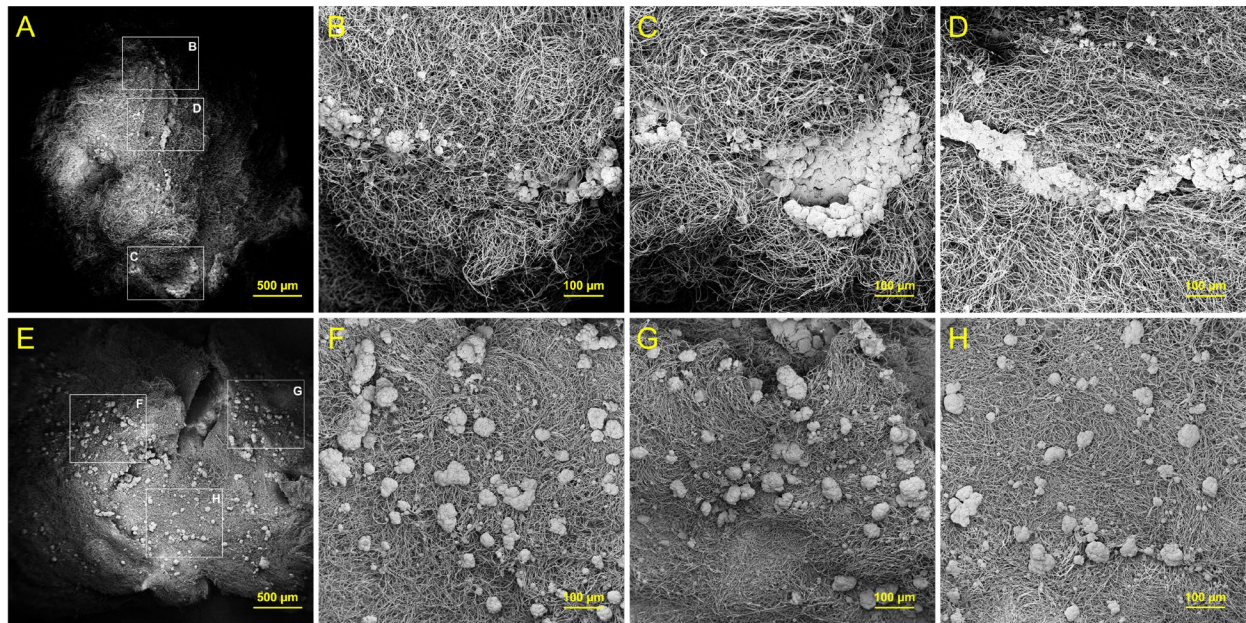


Figure 4.6. SEM images of cell spheroids growing on silica-coated scaffold for 7 days after cell-seeding with 2×10^4 cells. (A) shows cells aggregating and growing into a few large cell spheroids; (B, C and D) show the zoom in views of the labeled areas highlighted with white squares in A, respectively; (E) shows cells evenly distributing on whole scaffold and forming hundreds of small uniform cell spheroids. (F, G and H) show the zoom in views of the labeled

areas highlighted with white squares in E, respectively. Some of the zoom in images were captured at different stage tilt angle, so that did not show identical images in the corresponding highlight area.

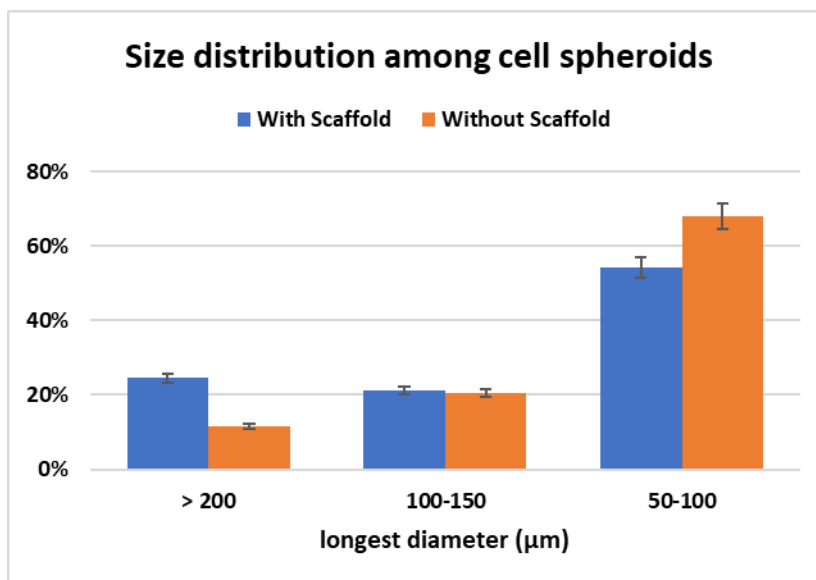


Figure 4.7. Statistic of size distribution for the cell spheroids with or without scaffold being cultured for 7 days. Only the cell spheroids having the largest diameter longer than 50 μm are included.

4.3.4 Cell viability assay of 3D cultured MCF-7 cell spheroids

To evaluate the cell proliferation growing on the scaffold, AlamarBlue assay was applied as a semi-quantification for the cell viability of the spheroids with or without the scaffolds (Figure 4.8). The cell viability of the spheroids growing on the scaffolds are significantly higher than those growing without scaffolds in most control groups, especially for the groups have larger amount of cell seeding. Based on our best knowledge, the possible reason is that the scaffolds provide more space 3-dimensionally rather than the bottom of the well. Another advantage of using the scaffold is that beyond the cell density limitation of the 96- well plate, over 5×10^4 cells could be seeded on a single piece of scaffold and formed numerous of cell

spheroids (Figure 4.9) for some specific type of purpose, like *in vitro* tumor derived tumor xenograft.

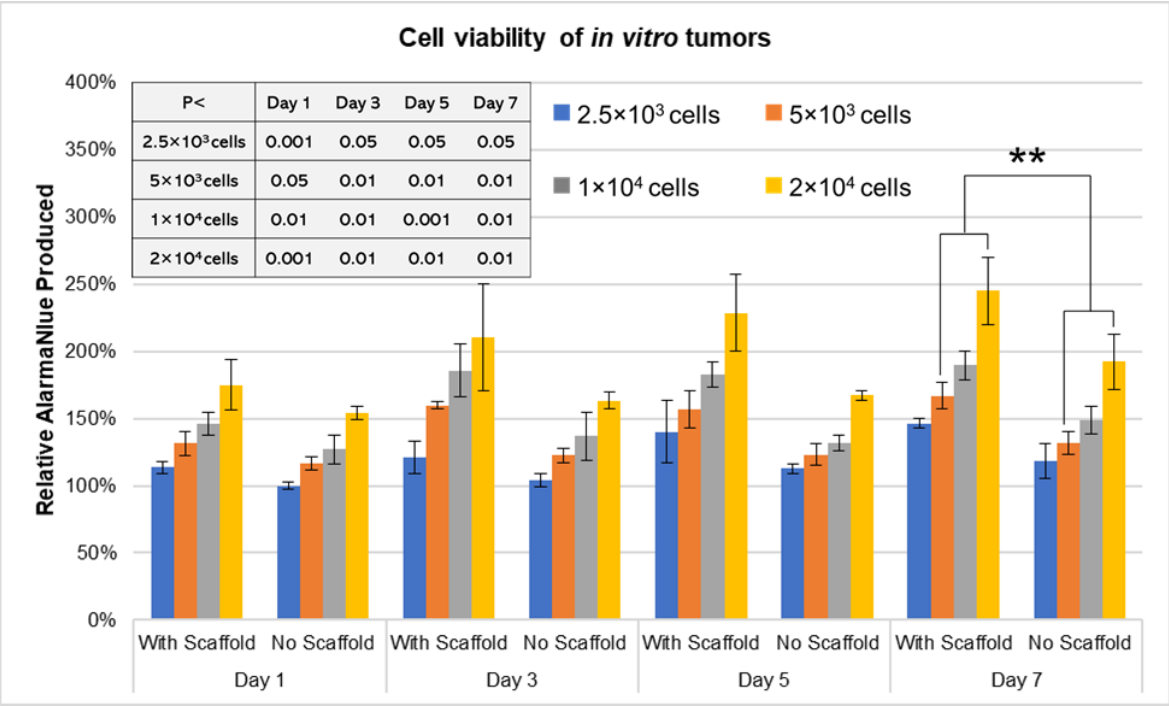


Figure 4.8. Comparison of AlarmaBlue assay between *in vitro* cell spheroids with or without the presence of scaffolds. The relative AlarmaBlue level is normalized by the one for 2.5×10^3 cells without scaffold at day 1. All the comparison between two corresponding groups has P value less than 0.05. ** indicates $P < 0.01$. The inset table shows the t-test comparison of the cell viability, for the same amount of cells growing for the same days.

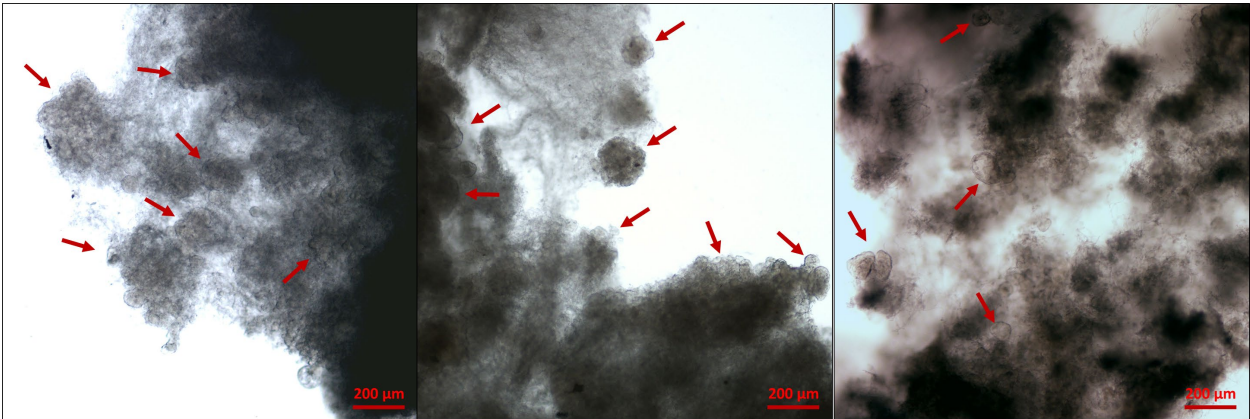


Figure 4.9. Microscopic images of 5×10^4 cells growing on scaffold for 7 days. Some cell spheroids are indicated by arrows.

4.3.5 Phage-antibody selection

Phage-antibody selection, also known as phage biopanning is a promising way to screen target-specific peptides out of billions of random peptides efficiently. This technique has been applied to find ligand for targeting therapy and specially to develop human antibody phage display-derived (APD) mAb since the first full human APD mAb were made for therapeutic use in 2007. However, this technique has never been applied *in vitro* tumor targeting ligand selection for the following possible reason. The free cell spheroids could be easily lost during the wash step every round. After 10 repeats of the washing steps, the best targeting phage candidates might have been lost in the first round of biopanning. The character of the silica coated fungi network scaffold makes phage biopanning against *in vitro* tumor much easier to accomplish than using the free cell spheroids. So, in this study, I first employed phage biopanning against *in vitro* MCF-7 tumors and identified a 12-residue peptide sequence with excellent binding affinity to the tumors. After 4 rounds of phage biopanning, 4 targeting peptide sequences SYPSNALSLHKY, TLGLRPVPVATT, SEPQNIWQYLRN and SYWYEASSYTGTV with the highest frequency were selected as the *in vitro* tumor targeting peptide (Table 4.1). The peptide with the highest tumor affinity should be verified by phage titer and IHC of cell imaging.

	Peptide Sequence	Count (201 colonies total)	Frequency
1	SYPSNALSLHKY	11	5.5%
2	TLGLRPVPVATT	7	3.5%
3	SEPQNIWQYLRN	6	3.0%
4	SYWYEASSYTGTV	6	3.0%
5	TLNVPPAKRSL	5	2.5%

6	WGVTKPIRTSTL	4	2.0%
7	MKAHHSQLYPRH	4	2.0%
8	TISAFTSFMPNT	3	1.5%
9	WGLTAQVPESRH	3	1.5%
10	YPSAHHSLMRPA	3	1.5%
11	GSAARTISPSLL	3	1.5%
12	HSTLLNHTTGVL	3	1.5%
13	IPWSPTRIIHAQ	3	1.5%
14	NLWATQPPSHHV	3	1.5%
15	NYLPHQSSSPSR	2	1.0%
16	SSHSSASVSPKT	2	1.0%
17	SSMPINSPATRQ	2	1.0%
18	SYASRHLPLLSS	2	1.0%
19	ISPSHLFHQAVK	2	1.0%
20	TYNYDMPLRGRA	2	1.0%
21	FQARWEPPRLQ	2	1.0%
22	APPITSVLFPYL	2	1.0%
23	AAHRVGGFNYHM	2	1.0%

Table 4.1. Summary of peptide sequences and frequencies in both 3rd and 4th rounds of Ph.D.-12 phage display against *in vitro* MCF-7 tumors. Only peptides having total colonies no less than 2 are included in this table.

4.4 Conclusion and Discussion

In this study, I have first applied the natural structure of fungi *Penicillium* to effortlessly make a cell-safe scaffold for culturing 3D *in vitro* tumors. The method has a low cost and requires no advanced skills. The cells formed a comparable number of spheroids with a similar size on the scaffold as them growing in commercial non-adherent culture dish. The cell viability assay indicated enhanced cell proliferation on the scaffold, most likely because the scaffold could provide more space for cell growth. Another advantage of our new scaffold is that the unique structure allowed itself to be easily transferred in different solutions. Therefore, the *in*

vitro tumors could be used for complex protocol such as paraffin embedding based histology and phage biopanning. *In vitro* tumors were first employed for phage-antibody selection in this study and four tumor-binding peptide candidates were identified. Tumor-homing analysis should be evaluated *in vitro* and *in vivo* in the future.

References

1. Rakonjac, J.; Bennett, N. J.; Spagnuolo, J.; Gagic, D.; Russel, M., Filamentous bacteriophage: biology, phage display and nanotechnology applications. *Current issues in molecular biology* **2011**, *13* (2), 51-76.
2. Yusuf, S.; Anand, S., Hormone replacement therapy: a time for pause. *CMAJ : Canadian Medical Association journal = journal de l'Association medicale canadienne* **2002**, *167* (4), 357-9.
3. DeSantis, C.; Ma, J.; Bryan, L.; Jemal, A., Breast cancer statistics, 2013. *CA: a cancer journal for clinicians* **2014**, *64* (1), 52-62.
4. DeSantis, C. E.; Fedewa, S. A.; Sauer, A. G.; Kramer, J. L.; Smith, R. A.; Jemal, A., Breast Cancer Statistics, 2015: Convergence of Incidence Rates Between Black and White Women. *Ca-Cancer J Clin* **2016**, *66* (1), 31-42.
5. Lee, J. H.; Nan, A., Combination drug delivery approaches in metastatic breast cancer. *Journal of drug delivery* **2012**, *2012*, 915375.
6. Din, F. U.; Aman, W.; Ullah, I.; Qureshi, O. S.; Mustapha, O.; Shafique, S.; Zeb, A., Effective use of nanocarriers as drug delivery systems for the treatment of selected tumors. *Int J Nanomed* **2017**, *12*, 7291-7309.
7. Kossai, M.; Duchemann, B.; Boutros, C.; Caramella, C.; Hollebecque, A.; Angevin, E.; Gazzah, A.; Bahleda, R.; Ileana, E.; Massard, C.; Vielh, P.; Soria, J. C.; Besse, B., Antitumor activity in advanced cancer patients with thymic malignancies enrolled in early clinical drug development programs (Phase I trials) at Gustave Roussy. *Lung Cancer* **2015**, *89* (3), 306-10.
8. Wheler, J.; Hong, D.; Swisher, S. G.; Falchook, G.; Tsimberidou, A. M.; Helgason, T.; Naing, A.; Stephen, B.; Janku, F.; Stephens, P. J.; Yelensky, R.; Kurzrock, R., Thymoma Patients Treated in a Phase I Clinic at MD Anderson Cancer Center: Responses to mTOR Inhibitors and Molecular Analyses. *Oncotarget* **2013**, *4* (6), 890-898.

9. Yang, Y.; Ding, L.; Wang, P., Dramatic response to anti-PD-1 therapy in a patient of squamous cell carcinoma of thymus with multiple lung metastases. *Journal of thoracic disease* **2016**, *8* (7), E535-7.
10. Yu, P.; Yu, H.; Guo, C.; Cui, Z.; Chen, X.; Yin, Q.; Zhang, P.; Yang, X.; Cui, H.; Li, Y., Reversal of doxorubicin resistance in breast cancer by mitochondria-targeted pH-responsive micelles. *Acta biomaterialia* **2015**, *14*, 115-24.
11. Lee, E. S.; Kim, J. H.; Sim, T.; Youn, Y. S.; Lee, B. J.; Oh, Y. T.; Oh, K. T., A feasibility study of a pH sensitive nanomedicine using doxorubicin loaded poly(aspartic acid-graft-imidazole)-block-poly(ethylene glycol) micelles. *J Mater Chem B* **2014**, *2* (9), 1152-1159.
12. Talelli, M.; Iman, M.; Varkouhi, A. K.; Rijcken, C. J.; Schiffelers, R. M.; Etrych, T.; Ulbrich, K.; van Nostrum, C. F.; Lammers, T.; Storm, G.; Hennink, W. E., Core-crosslinked polymeric micelles with controlled release of covalently entrapped doxorubicin. *Biomaterials* **2010**, *31* (30), 7797-804.
13. Zhang, Y.; Huang, Y.; Li, S., Polymeric micelles: nanocarriers for cancer-targeted drug delivery. *AAPS PharmSciTech* **2014**, *15* (4), 862-71.
14. Mohajer, G.; Lee, E. S.; Bae, Y. H., Enhanced intercellular retention activity of novel pH-sensitive polymeric micelles in wild and multidrug resistant MCF-7 cells. *Pharmaceutical research* **2007**, *24* (9), 1618-27.
15. Yuan, Y.; Cai, T.; Xia, X.; Zhang, R.; Chiba, P.; Cai, Y., Nanoparticle delivery of anticancer drugs overcomes multidrug resistance in breast cancer. *Drug delivery* **2016**, *23* (9), 3350-3357.
16. Bangham, A. D., Liposomes: the Babraham connection. *Chemistry and physics of lipids* **1993**, *64* (1-3), 275-85.
17. Kontermann, R. E., Immunoliposomes for cancer therapy. *Current opinion in molecular therapeutics* **2006**, *8* (1), 39-45.

18. Marty, M.; Cognetti, F.; Maraninchi, D.; Snyder, R.; Mauriac, L.; Tubiana-Hulin, M.; Chan, S.; Grimes, D.; Anton, A.; Lluch, A.; Kennedy, J.; O'Byrne, K.; Conte, P.; Green, M.; Ward, C.; Mayne, K.; Extra, J. M., Randomized phase II trial of the efficacy and safety of trastuzumab combined with docetaxel in patients with human epidermal growth factor receptor 2-positive metastatic breast cancer administered as first-line treatment: The M77001 study group. *J Clin Oncol* **2005**, *23* (19), 4265-4274.
19. Robert, N.; Leyland-Jones, B.; Asmar, L.; Belt, R.; Ilegbodu, D.; Loesch, D.; Raju, R.; Valentine, E.; Sayre, R.; Cobleigh, M.; Albain, K.; McCullough, C.; Fuchs, L.; Slamon, D., Randomized phase III study of trastuzumab, paclitaxel, and carboplatin compared with trastuzumab and paclitaxel in women with HER-2-overexpressing metastatic breast cancer. *J Clin Oncol* **2006**, *24* (18), 2786-92.
20. Lee, C. M.; Iorno, N.; Sierro, F.; Christ, D., Selection of human antibody fragments by phage display. *Nat Protoc* **2007**, *2* (11), 3001-8.
21. Peer, D.; Karp, J. M.; Hong, S.; Farokhzad, O. C.; Margalit, R.; Langer, R., Nanocarriers as an emerging platform for cancer therapy. *Nat Nanotechnol* **2007**, *2* (12), 751-760.
22. Smith, G. P.; Petrenko, V. A., Phage display. *Chem Rev* **1997**, *97* (2), 391-410.
23. Kehoe, J. W.; Kay, B. K., Filamentous phage display in the new millennium. *Chem Rev* **2005**, *105* (11), 4056-4072.
24. Krag, D. N.; Shukla, G. S.; Shen, G. P.; Pero, S.; Ashikaga, T.; Fuller, S.; Weaver, D. L.; Burdette-Radoux, S.; Thomas, C., Selection of tumor-binding ligands in cancer patients with phage display libraries. *Cancer Res* **2006**, *66* (15), 7724-33.
25. Sarikaya, M.; Tamerler, C.; Schwartz, D. T.; Baneyx, F. O., Materials assembly and formation using engineered polypeptides. *Annu Rev Mater Res* **2004**, *34*, 373-408.
26. Huang, W.; Petrosino, J.; Palzkill, T., Display of functional beta-lactamase inhibitory protein on the surface of M13 bacteriophage. *Antimicrobial agents and chemotherapy* **1998**, *42* (11), 2893-7.

27. Lee, S. K.; Yun, D. S.; Belcher, A. M., Cobalt ion mediated self-assembly of genetically engineered bacteriophage for biomimetic Co-Pt hybrid material. *Biomacromolecules* **2006**, *7* (1), 14-7.
28. Sunderland, K. S.; Yang, M.; Mao, C., Phage-Enabled Nanomedicine: From Probes to Therapeutics in Precision Medicine. *Angewandte Chemie* **2017**, *56* (8), 1964-1992.
29. Hammers, C. M.; Stanley, J. R., Antibody phage display: technique and applications. *J Invest Dermatol* **2014**, *134* (2), 1-5.
30. Takaba, H.; Takayanagi, H., The Mechanisms of T Cell Selection in the Thymus. *Trends Immunol* **2017**, *38* (11), 805-816.
31. Yang, M.; Sunderland, K.; Mao, C., Virus-Derived Peptides for Clinical Applications. *Chem Rev* **2017**, *117* (15), 10377-10402.
32. Li, Y. J.; Whyburn, G. P.; Huang, Y., Specific Peptide Regulated Synthesis of Ultrasmall Platinum Nanocrystals. *J Am Chem Soc* **2009**, *131* (44), 15998-15999.
33. Cao, B. R.; Yang, M. Y.; Mao, C. B., Phage as a Genetically Modifiable Supramacromolecule in Chemistry, Materials and Medicine. *Accounts of chemical research* **2016**, *49* (6), 1111-1120.
34. Naik, R. R.; Jones, S. E.; Murray, C. J.; McAuliffe, J. C.; Vaia, R. A.; Stone, M. O., Peptide templates for nanoparticle synthesis derived from polymerase chain reaction-driven phage display. *Adv Funct Mater* **2004**, *14* (1), 25-30.
35. Wilhelm, S.; Hirsch, T.; Patterson, W. M.; Scheucher, E.; Mayr, T.; Wolfbeis, O. S., Multicolor upconversion nanoparticles for protein conjugation. *Theranostics* **2013**, *3* (4), 239-48.
36. Li, C.; Liu, J.; Alonso, S.; Li, F.; Zhang, Y., Upconversion nanoparticles for sensitive and in-depth detection of Cu²⁺ ions. *Nanoscale* **2012**, *4* (19), 6065-71.
37. Weissleder, R., A clearer vision for in vivo imaging. *Nat Biotechnol* **2001**, *19* (4), 316-7.

38. Chen, W.; Chen, M.; Zang, Q.; Wang, L.; Tang, F.; Han, Y.; Yang, C.; Deng, L.; Liu, Y. N., NIR light controlled release of caged hydrogen sulfide based on upconversion nanoparticles. *Chem Commun (Camb)* **2015**, 51 (44), 9193-6.
39. Abdul Jalil, R.; Zhang, Y., Biocompatibility of silica coated NaYF₄ upconversion fluorescent nanocrystals. *Biomaterials* **2008**, 29 (30), 4122-8.
40. Xiong, L.; Yang, T.; Yang, Y.; Xu, C.; Li, F., Long-term in vivo biodistribution imaging and toxicity of polyacrylic acid-coated upconversion nanophosphors. *Biomaterials* **2010**, 31 (27), 7078-85.
41. Sun, Y.; Feng, W.; Yang, P.; Huang, C.; Li, F., The biosafety of lanthanide upconversion nanomaterials. *Chemical Society reviews* **2015**, 44 (6), 1509-25.
42. Lin, M.; Zhao, Y.; Wang, S.; Liu, M.; Duan, Z.; Chen, Y.; Li, F.; Xu, F.; Lu, T., Recent advances in synthesis and surface modification of lanthanide-doped upconversion nanoparticles for biomedical applications. *Biotechnology advances* **2012**, 30 (6), 1551-61.
43. Tian, G.; Zhang, X.; Gu, Z. J.; Zhao, Y. L., Recent Advances in Upconversion Nanoparticles-Based Multifunctional Nanocomposites for Combined Cancer Therapy. *Advanced materials* **2015**, 27 (47), 7692-7712.
44. Riley, R. S.; Day, E. S., Gold nanoparticle-mediated photothermal therapy: applications and opportunities for multimodal cancer treatment. *Wiley interdisciplinary reviews. Nanomedicine and nanobiotechnology* **2017**, 9 (4).
45. Loo, C.; Lowery, A.; Halas, N.; West, J.; Drezek, R., Immunotargeted nanoshells for integrated cancer imaging and therapy. *Nano Lett* **2005**, 5 (4), 709-11.
46. Qiu, P. H.; Yang, M. Y.; Qu, X. W.; Huai, Y. Y.; Zhu, Y.; Mao, C. B., Tuning photothermal properties of gold nanodendrites for in vivo cancer therapy within a wide near infrared range by simply controlling their degree of branching. *Biomaterials* **2016**, 104, 138-144.

47. Xia, Y.; Li, W.; Cobley, C. M.; Chen, J.; Xia, X.; Zhang, Q.; Yang, M.; Cho, E. C.; Brown, P. K., Gold nanocages: from synthesis to theranostic applications. *Accounts of chemical research* **2011**, *44* (10), 914-24.
48. Huang, X.; El-Sayed, M. A., Gold nanoparticles: Optical properties and implementations in cancer diagnosis and photothermal therapy. *Journal of Advanced Research* **2010**, *1* (1), 13-28.
49. Chithrani, B. D.; Ghazani, A. A.; Chan, W. C. W., Determining the size and shape dependence of gold nanoparticle uptake into mammalian cells. *Nano Lett* **2006**, *6* (4), 662-668.
50. Kim, J. B., Three-dimensional tissue culture models in cancer biology. *Seminars in cancer biology* **2005**, *15* (5), 365-77.
51. Kumar, H. R.; Zhong, X. L.; Hoelz, D. J.; Rescorla, F. J.; Hickey, R. J.; Malkas, L. H.; Sandoval, J. A., Three-dimensional neuroblastoma cell culture: proteomic analysis between monolayer and multicellular tumor spheroids. *Pediatr Surg Int* **2008**, *24* (11), 1229-1234.
52. Holliday, D. L.; Brouillette, K. T.; Markert, A.; Gordon, L. A.; Jones, J. L., Novel multicellular organotypic models of normal and malignant breast: tools for dissecting the role of the microenvironment in breast cancer progression. *Breast cancer research : BCR* **2009**, *11* (1), R3.
53. Smalley, K. S.; Lioni, M.; Noma, K.; Haass, N. K.; Herlyn, M., In vitro three-dimensional tumor microenvironment models for anticancer drug discovery. *Expert opinion on drug discovery* **2008**, *3* (1), 1-10.
54. Antoni, D.; Burckel, H.; Josset, E.; Noel, G., Three-dimensional cell culture: a breakthrough in vivo. *International journal of molecular sciences* **2015**, *16* (3), 5517-27.
55. Edmondson, R.; Broglie, J. J.; Adcock, A. F.; Yang, L. J., Three-Dimensional Cell Culture Systems and Their Applications in Drug Discovery and Cell-Based Biosensors. *Assay Drug Dev Techn* **2014**, *12* (4), 207-218.

56. Lv, D.; Hu, Z.; Lu, L.; Lu, H.; Xu, X., Three-dimensional cell culture: A powerful tool in tumor research and drug discovery. *Oncology letters* **2017**, *14* (6), 6999-7010.
57. Chen, L.; Xiao, Z.; Meng, Y.; Zhao, Y.; Han, J.; Su, G.; Chen, B.; Dai, J., The enhancement of cancer stem cell properties of MCF-7 cells in 3D collagen scaffolds for modeling of cancer and anti-cancer drugs. *Biomaterials* **2012**, *33* (5), 1437-44.
58. Zanoni, M.; Piccinini, F.; Arienti, C.; Zamagni, A.; Santi, S.; Polico, R.; Bevilacqua, A.; Tesei, A., 3D tumor spheroid models for in vitro therapeutic screening: a systematic approach to enhance the biological relevance of data obtained. *Scientific reports* **2016**, *6*.
59. Weiswald, L. B.; Bellet, D.; Dangles-Marie, V., Spherical cancer models in tumor biology. *Neoplasia* **2015**, *17* (1), 1-15.
60. Napolitano, A. P.; Dean, D. M.; Man, A. J.; Youssef, J.; Ho, D. N.; Rago, A. P.; Lech, M. P.; Morgan, J. R., Scaffold-free three-dimensional cell culture utilizing micromolded nonadhesive hydrogels. *BioTechniques* **2007**, *43* (4), 494, 496-500.
61. Albanese, A.; Lam, A. K.; Sykes, E. A.; Rocheleau, J. V.; Chan, W. C. W., Tumour-on-a-chip provides an optical window into nanoparticle tissue transport. *Nat Commun* **2013**, *4*.
62. Esch, E. W.; Bahinski, A.; Huh, D., Organs-on-chips at the frontiers of drug discovery. *Nat Rev Drug Discov* **2015**, *14* (4), 248-260.
63. Sabhachandani, P.; Motwani, V.; Cohen, N.; Sarkar, S.; Torchilin, V.; Konry, T., Generation and functional assessment of 3D multicellular spheroids in droplet based microfluidics platform. *Lab on a chip* **2016**, *16* (3), 497-505.
64. Dhiman, H. K.; Ray, A. R.; Panda, A. K., Characterization and evaluation of chitosan matrix for in vitro growth of MCF-7 breast cancer cell lines. *Biomaterials* **2004**, *25* (21), 5147-54.
65. de la Puente, P.; Ludena, D., Cell culture in autologous fibrin scaffolds for applications in tissue engineering. *Experimental cell research* **2014**, *322* (1), 1-11.

66. Ekaputra, A. K.; Prestwich, G. D.; Cool, S. M.; Hutmacher, D. W., The three-dimensional vascularization of growth factor-releasing hybrid scaffold of poly (epsilon-caprolactone)/collagen fibers and hyaluronic acid hydrogel. *Biomaterials* **2011**, 32 (32), 8108-8117.
67. Tung, Y. C.; Hsiao, A. Y.; Allen, S. G.; Torisawa, Y. S.; Ho, M.; Takayama, S., High-throughput 3D spheroid culture and drug testing using a 384 hanging drop array. *Analyst* **2011**, 136 (3), 473-478.
68. Falkenberg, N.; Hofig, I.; Rosemann, M.; Szumielewski, J.; Richter, S.; Schorpp, K.; Hadian, K.; Aubele, M.; Atkinson, M. J.; Anastasov, N., Three-dimensional microtissues essentially contribute to preclinical validations of therapeutic targets in breast cancer. *Cancer medicine* **2016**, 5 (4), 703-10.
69. Baze, A.; Parmentier, C.; Hendriks, D. F. G.; Hurrell, T.; Heyd, B.; Bachellier, P.; Schuster, C.; Ingelman-Sundberg, M.; Richert, L., Three-Dimensional Spheroid Primary Human Hepatocytes in Monoculture and Coculture with Nonparenchymal Cells. *Tissue engineering. Part C, Methods* **2018**, 24 (9), 534-545.
70. Katt, M. E.; Placone, A. L.; Wong, A. D.; Xu, Z. S.; Searson, P. C., In Vitro Tumor Models: Advantages, Disadvantages, Variables, and Selecting the Right Platform. *Frontiers in bioengineering and biotechnology* **2016**, 4, 12.
71. Kingston, D. G. I., Tubulin-Interactive Natural Products as Anticancer Agents. *J Nat Prod* **2009**, 72 (3), 507-515.
72. Butler, M. S., Natural products to drugs: natural product-derived compounds in clinical trials. *Nat Prod Rep* **2008**, 25 (3), 475-516.
73. Gueritte, F., *Anticancer agents from natural products*. 2 ed.; CRC press: 2011.
74. Svoboda, G. H.; Johnson, I. S.; Gorman, M.; Neuss, N., Current status of research on the alkaloids of *Vinca rosea* Linn. (*Catharanthus roseus* G. Don). *Journal of pharmaceutical sciences* **1962**, 51, 707-20.

75. Noble, R. L.; Beer, C. T.; Cutts, J. H., Role of chance observations in chemotherapy: Vinca rosea. *Annals of the New York Academy of Sciences* **1958**, 76 (3), 882-94.
76. Wani, M. C.; Taylor, H. L.; Wall, M. E.; Coggon, P.; McPhail, A. T., Plant antitumor agents. VI. The isolation and structure of taxol, a novel antileukemic and antitumor agent from *Taxus brevifolia*. *J Am Chem Soc* **1971**, 93 (9), 2325-7.
77. Schiff, P. B.; Fant, J.; Horwitz, S. B., Promotion of microtubule assembly in vitro by taxol. *Nature* **1979**, 277 (5698), 665-7.
78. McGuire, W. P.; Rowinsky, E. K.; Rosenshein, N. B.; Grumbine, F. C.; Ettinger, D. S.; Armstrong, D. K.; Donehower, R. C., Taxol - a Unique Antineoplastic Agent with Significant Activity in Advanced Ovarian Epithelial Neoplasms. *Ann Intern Med* **1989**, 111 (4), 273-279.
79. Holmes, F. A.; Walters, R. S.; Theriault, R. L.; Forman, A. D.; Newton, L. K.; Raber, M. N.; Buzdar, A. U.; Frye, D. K.; Hortobagyi, G. N., Phase II trial of taxol, an active drug in the treatment of metastatic breast cancer. *Journal of the National Cancer Institute* **1991**, 83 (24), 1797-805.
80. Bates, D.; Eastman, A., Microtubule destabilising agents: far more than just antimetabolic anticancer drugs. *Brit J Clin Pharmacol* **2017**, 83 (2), 255-268.
81. Jordan, M. A.; Wilson, L., Microtubules as a target for anticancer drugs. *Nature Reviews Cancer* **2004**, 4 (4), 253-265.
82. Calvaresi, E. C.; Hergenrother, P. J., Glucose conjugation for the specific targeting and treatment of cancer. *Chemical science* **2013**, 4 (6), 2319-2333.
83. R, M.; K, S.; H, H., Effects of the properties of short peptides conjugated with cell-penetrating peptides on their internalization into cells. *Sci Rep*. **2015**, 5 (12884).
84. IA, K.; K, K., High density of octaarginine stimulates macropinocytosis leading to efficient intracellular trafficking for gene expression. *J Biol Chem*. **2006**, 281 (6), 3544-51.

85. S, V.; SD, L., Recent developments in peptide-based nucleic acid delivery. . *Int J Mol Sci.* **2008**, *9* (7), 1276-320.
86. Abbineni, G.; Modali, S.; Safiejko-Mrocza, B.; Petrenko, V. A.; Mao, C., Evolutionary selection of new breast cancer cell-targeting peptides and phages with the cell-targeting peptides fully displayed on the major coat and their effects on actin dynamics during cell internalization. *Molecular pharmaceutics* **2010**, *7* (5), 1629-42.
87. Cao, B.; Mao, C., Identification of microtubule-binding domains on microtubule-associated proteins by major coat phage display technique. *Biomacromolecules* **2009**, *10* (3), 555-64.
88. Kolarova, M.; Garcia-Sierra, F.; Bartos, A.; Ricny, J.; Ripova, D., Structure and pathology of tau protein in Alzheimer disease. *International journal of Alzheimer's disease* **2012**, *2012*, 731526.
89. Liu, C.; Wang, H.; Li, X.; Chen, D., Monodisperse, size-tunable and highly efficient beta-NaYF₄:Yb,Er(Tm) up-conversion luminescent nanospheres: controllable synthesis and their surface modifications. *J Mater Chem* **2009**, *19* (21), 3546-3553.
90. Li, Z.; Zhang, Y., An efficient and user-friendly method for the synthesis of hexagonal-phase NaYF₄:Yb, Er/Tm nanocrystals with controllable shape and upconversion fluorescence. *Nanotechnology* **2008**, *19* (34), 345606.
91. ML, S.; F, G., Microtubule assembly in the absence of added nucleotides. *Proc Natl Acad Sci U S A.* **1973**, *70* (3), 765-8.
92. Burkhart, C. A.; Kavallaris, M.; Horwitz, S. B., The role of beta-tubulin isotypes in resistance to antimetabolic drugs. *Bba-Rev Cancer* **2001**, *1471* (2), O1-O9.
93. Kavallaris, M.; Kuo, D. Y.; Burkhart, C. A.; Regl, D. L.; Norris, M. D.; Haber, M.; Horwitz, S. B., Taxol-resistant epithelial ovarian tumors are associated with altered expression of specific beta-tubulin isotypes. *The Journal of clinical investigation* **1997**, *100* (5), 1282-93.

94. Ferlini, C.; Cicchillitti, L.; Raspaglio, G.; Bartollino, S.; Cimitan, S.; Bertucci, C.; Mozzetti, S.; Gallo, D.; Persico, M.; Fattorusso, C.; Campiani, G.; Scambia, G., Paclitaxel directly binds to Bcl-2 and functionally mimics activity of Nur77. *Cancer Res* **2009**, *69* (17), 6906-14.
95. Mackenzie, L. E.; Goode, J. A.; Vakurov, A.; Nampi, P. P.; Saha, S.; Jose, G.; Millner, P. A., The theoretical molecular weight of NaYF₄:RE upconversion nanoparticles. *Scientific reports* **2018**, *8* (1), 1106.
96. Blajeski, A. L.; Phan, V. A.; Kottke, T. J.; Kaufmann, S. H., G(1) and G(2) cell-cycle arrest following microtubule depolymerization in human breast cancer cells. *J Clin Invest* **2002**, *110* (1), 91-9.
97. Lv, X.; He, C.; Huang, C.; Hua, G.; Wang, Z.; Remmenga, S. W.; Rodabough, K. J.; Karpf, A. R.; Dong, J.; Davis, J. S.; Wang, C., G-1 Inhibits Breast Cancer Cell Growth via Targeting Colchicine-Binding Site of Tubulin to Interfere with Microtubule Assembly. *Molecular cancer therapeutics* **2017**, *16* (6), 1080-1091.
98. Saoudi, Y.; Fotadar, R.; Abrieu, A.; Doree, M.; Wehland, J.; Margolis, R. L.; Job, D., Stepwise reconstitution of interphase microtubule dynamics in permeabilized cells and comparison to dynamic mechanisms in intact cells. *The Journal of cell biology* **1998**, *142* (6), 1519-32.
99. Rai, A.; Surolia, A.; Panda, D., An antitubulin agent BCFMT inhibits proliferation of cancer cells and induces cell death by inhibiting microtubule dynamics. *PloS one* **2012**, *7* (8), e44311.
100. Duangmano, S.; Sae-lim, P.; Suksamrarn, A.; Domann, F. E.; Patmasiriwat, P., Cucurbitacin B inhibits human breast cancer cell proliferation through disruption of microtubule polymerization and nucleophosmin/B23 translocation. *Bmc Complem Altern M* **2012**, *12*.

101. Abeylath, S. C.; Ganta, S.; Iyer, A. K.; Amiji, M., Combinatorial-designed multifunctional polymeric nanosystems for tumor-targeted therapeutic delivery. *Accounts of chemical research* **2011**, *44* (10), 1009-17.
102. Caldorera-Moore, M. E.; Liechty, W. B.; Peppas, N. A., Responsive theranostic systems: integration of diagnostic imaging agents and responsive controlled release drug delivery carriers. *Accounts of chemical research* **2011**, *44* (10), 1061-70.
103. Shi, J.; Xiao, Z.; Kamaly, N.; Farokhzad, O. C., Self-assembled targeted nanoparticles: evolution of technologies and bench to bedside translation. *Accounts of chemical research* **2011**, *44* (10), 1123-34.
104. Koo, H.; Huh, M. S.; Sun, I. C.; Yuk, S. H.; Choi, K.; Kim, K.; Kwon, I. C., In vivo targeted delivery of nanoparticles for theranosis. *Accounts of chemical research* **2011**, *44* (10), 1018-28.
105. Scott, A. M.; Wolchok, J. D.; Old, L. J., Antibody therapy of cancer. *Nature reviews. Cancer* **2012**, *12* (4), 278-87.
106. Loo, D. T.; Mather, J. P., Antibody-based identification of cell surface antigens: targets for cancer therapy. *Curr Opin Pharmacol* **2008**, *8* (5), 627-631.
107. Trikha, M.; Corringham, R.; Klein, B.; Rossi, J. F., Targeted anti-interleukin-6 monoclonal antibody therapy for cancer: a review of the rationale and clinical evidence. *Clinical cancer research : an official journal of the American Association for Cancer Research* **2003**, *9* (13), 4653-65.
108. Schrama, D.; Reisfeld, R. A.; Becker, J. C., Antibody targeted drugs as cancer therapeutics. *Nat Rev Drug Discov* **2006**, *5* (2), 147-159.
109. Milenic, D. E.; Brady, E. D.; Brechbiel, M. W., Antibody-targeted radiation cancer therapy. *Nat Rev Drug Discov* **2004**, *3* (6), 488-99.

110. Srinivasarao, M.; Galliford, C. V.; Low, P. S., Principles in the design of ligand-targeted cancer therapeutics and imaging agents. *Nat Rev Drug Discov* **2015**, *14* (3), 203-19.
111. Hilgenbrink, A. R.; Low, P. S., Folate receptor-mediated drug targeting: from therapeutics to diagnostics. *Journal of pharmaceutical sciences* **2005**, *94* (10), 2135-46.
112. Paulos, C. M.; Turk, M. J.; Breur, G. J.; Low, P. S., Folate receptor-mediated targeting of therapeutic and imaging agents to activated macrophages in rheumatoid arthritis. *Advanced drug delivery reviews* **2004**, *56* (8), 1205-17.
113. Landmark, K. J.; DiMaggio, S.; Ward, J.; Kelly, C. V.; Vogt, S.; Hong, S.; Kotlyar, A.; Myc, A.; Thomas, T. P.; Penner-Hahn, J. E.; Baker, J. R.; Holl, M. M. B.; Orr, B. G., Synthesis, characterization, and in vitro testing of superparamagnetic iron oxide nanoparticles targeted using folic acid-conjugated dendrimers. *Acs Nano* **2008**, *2* (4), 773-783.
114. Fan, N. C.; Cheng, F. Y.; Ho, J. A. A.; Yeh, C. S., Photocontrolled Targeted Drug Delivery: Photocaged Biologically Active Folic Acid as a Light-Responsive Tumor-Targeting Molecule. *Angew Chem Int Edit* **2012**, *51* (35), 8806-8810.
115. Zuber, G.; Zammuto-Italiano, L.; Dauty, E.; Behr, J. P., Targeted gene delivery to cancer cells: directed assembly of nanometric DNA particles coated with folic acid. *Angewandte Chemie* **2003**, *42* (23), 2666-9.
116. Cho, H. J.; Yoon, H. Y.; Koo, H.; Ko, S. H.; Shim, J. S.; Lee, J. H.; Kim, K.; Kwon, I. C.; Kim, D. D., Self-assembled nanoparticles based on hyaluronic acid-ceramide (HA-CE) and Pluronic(R) for tumor-targeted delivery of docetaxel. *Biomaterials* **2011**, *32* (29), 7181-90.
117. Lee, Y.; Lee, H.; Kim, Y. B.; Kim, J.; Hyeon, T.; Park, H.; Messersmith, P. B.; Park, T. G., Bioinspired Surface Immobilization of Hyaluronic Acid on Monodisperse Magnetite Nanocrystals for Targeted Cancer Imaging. *Advanced materials* **2008**, *20* (21), 4154-4157.
118. Jiang, T.; Zhang, Z.; Zhang, Y.; Lv, H.; Zhou, J.; Li, C.; Hou, L.; Zhang, Q., Dual-functional liposomes based on pH-responsive cell-penetrating peptide and hyaluronic acid for tumor-targeted anticancer drug delivery. *Biomaterials* **2012**, *33* (36), 9246-58.

119. Li, J.; He, Y.; Sun, W.; Luo, Y.; Cai, H.; Pan, Y.; Shen, M.; Xia, J.; Shi, X., Hyaluronic acid-modified hydrothermally synthesized iron oxide nanoparticles for targeted tumor MR imaging. *Biomaterials* **2014**, *35* (11), 3666-77.
120. Chen, C.; Ke, J.; Zhou, X. E.; Yi, W.; Brunzelle, J. S.; Li, J.; Yong, E. L.; Xu, H. E.; Melcher, K., Structural basis for molecular recognition of folic acid by folate receptors. *Nature* **2013**, *500* (7463), 486-9.
121. Mankoff, D. A.; Link, J. M.; Linden, H. M.; Sundararajan, L.; Krohn, K. A., Tumor receptor imaging. *Journal of nuclear medicine : official publication, Society of Nuclear Medicine* **2008**, *49 Suppl 2*, 149S-63S.
122. Zhao, X.; Li, H.; Lee, R. J., Targeted drug delivery via folate receptors. *Expert opinion on drug delivery* **2008**, *5* (3), 309-19.
123. Ahrens, T.; Assmann, V.; Fieber, C.; Termeer, C. C.; Herrlich, P.; Hofmann, M.; Simon, J. C., CD44 is the principal mediator of hyaluronic-acid-induced melanoma cell proliferation. *J Invest Dermatol* **2001**, *116* (1), 93-101.
124. Collins, F. S.; Varmus, H., A new initiative on precision medicine. *The New England journal of medicine* **2015**, *372* (9), 793-5.
125. Schork, N. J., Personalized medicine: Time for one-person trials. *Nature* **2015**, *520* (7549), 609-11.
126. Huang, X. H.; El-Sayed, I. H.; Qian, W.; El-Sayed, M. A., Cancer cell imaging and photothermal therapy in the near-infrared region by using gold nanorods. *J Am Chem Soc* **2006**, *128* (6), 2115-2120.
127. Cho, S. K.; Emoto, K.; Su, L. J.; Yang, X.; Flaig, T. W.; Park, W., Functionalized gold nanorods for thermal ablation treatment of bladder cancer. *Journal of biomedical nanotechnology* **2014**, *10* (7), 1267-76.

128. Cheng, Y.; Meyers, J. D.; Agnes, R. S.; Doane, T. L.; Kenney, M. E.; Broome, A. M.; Burda, C.; Basilion, J. P., Addressing brain tumors with targeted gold nanoparticles: a new gold standard for hydrophobic drug delivery? *Small* **2011**, 7 (16), 2301-6.
129. von Maltzahn, G.; Park, J. H.; Agrawal, A.; Bandaru, N. K.; Das, S. K.; Sailor, M. J.; Bhatia, S. N., Computationally Guided Photothermal Tumor Therapy Using Long-Circulating Gold Nanorod Antennas. *Cancer Res* **2009**, 69 (9), 3892-3900.
130. Arap, W.; Pasqualini, R.; Ruoslahti, E., Cancer treatment by targeted drug delivery to tumor vasculature in a mouse model. *Science* **1998**, 279 (5349), 377-80.
131. Du, B.; Han, H.; Wang, Z.; Kuang, L.; Wang, L.; Yu, L.; Wu, M.; Zhou, Z.; Qian, M., targeted drug delivery to hepatocarcinoma in vivo by phage-displayed specific binding peptide. *Molecular cancer research : MCR* **2010**, 8 (2), 135-44.
132. Newton, J. R.; Kelly, K. A.; Mahmood, U.; Weissleder, R.; Deutscher, S. L., In vivo selection of phage for the optical imaging of PC-3 human prostate carcinoma in mice. *Neoplasia* **2006**, 8 (9), 772-80.
133. Wang, T.; Hartner, W. C.; Gillespie, J. W.; Praveen, K. P.; Yang, S.; Mei, L. A.; Petrenko, V. A.; Torchilin, V. P., Enhanced tumor delivery and antitumor activity in vivo of liposomal doxorubicin modified with MCF-7-specific phage fusion protein. *Nanomedicine : nanotechnology, biology, and medicine* **2014**, 10 (2), 421-30.
134. Wang, T.; D'Souza, G. G.; Bedi, D.; Fagbohun, O. A.; Potturi, L. P.; Papahadjopoulos-Sternberg, B.; Petrenko, V. A.; Torchilin, V. P., Enhanced binding and killing of target tumor cells by drug-loaded liposomes modified with tumor-specific phage fusion coat protein. *Nanomedicine (Lond)* **2010**, 5 (4), 563-74.
135. Wang, T.; Petrenko, V. A.; Torchilin, V. P., Paclitaxel-loaded polymeric micelles modified with MCF-7 cell-specific phage protein: enhanced binding to target cancer cells and increased cytotoxicity. *Molecular pharmaceutics* **2010**, 7 (4), 1007-14.

136. Wang, T.; Yang, S. H.; Petrenko, V. A.; Torchilin, V. P., Cytoplasmic Delivery of Liposomes into MCF-7 Breast Cancer Cells Mediated by Cell-Specific Phage Fusion Coat Protein. *Molecular pharmaceutics* **2010**, 7 (4), 1149-1158.
137. Lupp, A.; Danz, M.; Muller, D., Morphology and cytochrome P450 isoforms expression in precision-cut rat liver slices. *Toxicology* **2001**, 161 (1-2), 53-66.
138. Gusnard, D.; Kirschner, R. H., Cell and organelle shrinkage during preparation for scanning electron microscopy: effects of fixation, dehydration and critical point drying. *J Microsc* **1977**, 110 (1), 51-7.

Appendix A: List of Abbreviations

2D	two-dimensional
3D	three-dimensional
AFM	atomic force microscope
ALP	alkaline phosphatase
APD	antibody phage display
AuNRs	gold nanorods
CPD	critical point drying
CTAB	cetyl trimethylammonium bromide
CTP	cell-targeting peptide
Ctrl	control
DAPI	4',6-diamidino-2-phenylindole
DLS	dynamic light scattering
DMEM	dulbecco's modified eagle medium
<i>E. coli</i>	<i>Escherichia coli</i>
EDC	<i>N</i> -(3-dimethylaminopropyl)- <i>N'</i> -ethylcarbodiimide hydrochloride
EDS	energy-dispersive X-ray spectroscopy
EGTA	ethylene glycol-bis(2-aminoethylether)- <i>N,N,N',N'</i> -tetraacetic acid
ELISA	enzyme-linked immunosorbent assay
EMEM	eagle's minimal essential medium
ER	estrogen
Ff	filamentary bacteria phage
HE	haematoxylin and eosin

HRT	hormone replacement therapy
IC50	half maximal inhibitory concentration
ICP-AES	inductively coupled plasma atomic emission spectroscopy
IGEPAL CO-520	polyoxyethylene (5) nonylphenylether,
LB	lysogeny broth
mAb	monoclonal antibody
mPEG-Silane	methosy polyethyleneglycol-silane
MES	2-(N-morpholino) ethanesulfonic acid
MT	microtubule
MW	molecular weight
NHS	<i>N</i> -Hydroxysuccinimide
NIR	near-infrared
OD	optical density
ODE	1-octadecene
pNPP	p-nitrophenyl phosphate
PBS	phosphate buffered saline
PEG	polyethyleneglycol
PFA	paraformaldehyde

PIPES	1,4-piperazinediethanesulfonic acid
Rd	round
SEM	scanning electron microscope
Silane-PEG-COOH	silane-polyethyleneglycol-acetic acid
TEM	transmission electron microscope
TEOS	tetraethoxysilane
TIP	tubulin-interactive peptide
TU	transducing units
UCNP	up-converting nano-particle
U. S.	United States
UV	ultraviolet
V	volume
WT	wild type

**SPRINGER NATURE LICENSE
TERMS AND CONDITIONS**

Nov 15, 2018

This Agreement between Xuewei Qu ("You") and Springer Nature ("Springer Nature") consists of your license details and the terms and conditions provided by Springer Nature and Copyright Clearance Center.

License Number	4470271183599
License date	Nov 15, 2018
Licensed Content Publisher	Springer Nature
Licensed Content Publication	Nature Nanotechnology
Licensed Content Title	Nanocarriers as an emerging platform for cancer therapy
Licensed Content Author	Dan Peer, Jeffrey M. Karp, Seungpyo Hong, Omid C. Farokhzad, Kimona Margalit et al.
Licensed Content Date	Dec 1, 2007
Licensed Content Volume	2
Licensed Content Issue	12
Type of Use	Thesis/Dissertation
Requestor type	academic/university or research institute
Format	electronic
Portion	figures/tables/illustrations
Number of figures/tables/illustrations	1
High-res required	no
Will you be translating?	no
Circulation/distribution	<501
Author of this Springer Nature content	no
Title	Graduate assistant
Institution name	University of Oklahoma
Expected presentation date	Dec 2018
Order reference number	21
Portions	Figure 3
Requestor Location	Xuewei Qu 317 Wadsack Dr. Apt. G NORMAN, OK 73072 United States Attn: Xuewei Qu
Billing Type	Invoice
Billing Address	Xuewei Qu 317 Wadsack Dr. Apt. G NORMAN, OK 73072 United States Attn: Xuewei Qu
Total	0.00 USD
Terms and Conditions	

<https://s100.copyright.com/AppDispatchServlet>

1/3

Appendix B: List of Copyrights and Permissions

**JOHN WILEY AND SONS LICENSE
TERMS AND CONDITIONS**

Nov 15, 2018

This Agreement between Xuewei Qu ("You") and John Wiley and Sons ("John Wiley and Sons") consists of your license details and the terms and conditions provided by John Wiley and Sons and Copyright Clearance Center.

License Number	4470310560708
License date	Nov 15, 2018
Licensed Content Publisher	John Wiley and Sons
Licensed Content Publication	Advanced Materials
Licensed Content Title	Recent Advances in Upconversion Nanoparticles-Based Multifunctional Nanocomposites for Combined Cancer Therapy
Licensed Content Author	Gan Tian, Xiao Zhang, Zhanjun Gu, et al
Licensed Content Date	Oct 27, 2015
Licensed Content Volume	27
Licensed Content Issue	47
Licensed Content Pages	21
Type of use	Dissertation/Thesis
Requestor type	University/Academic
Format	Electronic
Portion	Figure/table
Number of figures/tables	1
Original Wiley figure/table number(s)	Scheme 3
Will you be translating?	No
Title of your thesis / dissertation	Graduate assistant
Expected completion date	Dec 2018
Expected size (number of pages)	1
Requestor Location	Xuewei Qu 317 Wadsack Dr. Apt. G NORMAN, OK 73072 United States Attn: Xuewei Qu
Publisher Tax ID	EU826007151
Total	0.00 USD

[Terms and Conditions](#)**TERMS AND CONDITIONS**

This copyrighted material is owned by or exclusively licensed to John Wiley & Sons, Inc. or one of its group companies (each a "Wiley Company") or handled on behalf of a society with which a Wiley Company has exclusive publishing rights in relation to a particular work (collectively "WILEY"). By clicking "accept" in connection with completing this licensing transaction, you agree that the following terms and conditions apply to this transaction (along with the billing and payment terms and conditions established by the Copyright Clearance Center Inc., ("CCC's Billing and Payment terms and conditions"), at the time that

**JOHN WILEY AND SONS LICENSE
TERMS AND CONDITIONS**

Nov 15, 2018

This Agreement between Xuwei Qu ("You") and John Wiley and Sons ("John Wiley and Sons") consists of your license details and the terms and conditions provided by John Wiley and Sons and Copyright Clearance Center.

License Number	4470310821413
License date	Nov 15, 2018
Licensed Content Publisher	John Wiley and Sons
Licensed Content Publication	Wiley Interdisciplinary Reviews - Nanomedicine and Nanobiotechnology
Licensed Content Title	Gold nanoparticle-mediated photothermal therapy: applications and opportunities for multimodal cancer treatment
Licensed Content Author	Rachel S. Riley, Emily S. Day
Licensed Content Date	Feb 3, 2017
Licensed Content Volume	9
Licensed Content Issue	4
Licensed Content Pages	16
Type of use	Dissertation/Thesis
Requestor type	University/Academic
Format	Electronic
Portion	Figure/table
Number of figures/tables	1
Original Wiley figure/table number(s)	Figure 1
Will you be translating?	No
Title of your thesis / dissertation	Graduate assistant
Expected completion date	Dec 2018
Expected size (number of pages)	1
Requestor Location	Xuwei Qu 317 Wadsack Dr. Apt. G NORMAN, OK 73072 United States Attn: Xuwei Qu
Publisher Tax ID	EU826007151
Total	0.00 USD
Terms and Conditions	



RightsLink®

Home

Account
Info

Help



ACS Publications
Most Trusted. Most Cited. Most Read.

Title: Determining the Size and Shape
Dependence of Gold
Nanoparticle Uptake into
Mammalian Cells

Author: B. Devika Chithrani, Arezou A.
Ghazani, Warren C. W. Chan

Publication: Nano Letters

Publisher: American Chemical Society

Date: Apr 1, 2006

Copyright © 2006, American Chemical Society

Logged in as:

Xuewei Qu

Account #:
3001366532

LOGOUT

PERMISSION/LICENSE IS GRANTED FOR YOUR ORDER AT NO CHARGE

This type of permission/license, instead of the standard Terms & Conditions, is sent to you because no fee is being charged for your order. Please note the following:

- Permission is granted for your request in both print and electronic formats, and translations.
- If figures and/or tables were requested, they may be adapted or used in part.
- Please print this page for your records and send a copy of it to your publisher/graduate school.
- Appropriate credit for the requested material should be given as follows: "Reprinted (adapted) with permission from (COMPLETE REFERENCE CITATION). Copyright (YEAR) American Chemical Society." Insert appropriate information in place of the capitalized words.
- One-time permission is granted only for the use specified in your request. No additional uses are granted (such as derivative works or other editions). For any other uses, please submit a new request.

If credit is given to another source for the material you requested, permission must be obtained from that source.

BACK

CLOSE WINDOW

Copyright © 2018 Copyright Clearance Center, Inc. All Rights Reserved. [Privacy statement](#). [Terms and Conditions](#).
Comments? We would like to hear from you. E-mail us at customercare@copyright.com

